Coalfire related CO_2 emissions and remote sensing

Aan steenkoolbranden gerelateerde CO_2 uitstoot en aardobservatie

(met een samenvatting in het Nederlands)

PROEFSCHRIFT

ter verkrijging van
de graad van doctor aan de Universiteit Utrecht
op gezag van de rector magnificus,
prof. dr. J.C. Stoof
ingevolge het besluit van het college voor promoties,
in het openbaar te verdedigen
op woensdag 11 Juni 2008 des ochtends te 10.30 uur

door

Prasun Kumar Gangopadhyay
geboren op 20 Maart, 1970 te Burdwan, India

Promotor: Prof. Dr. Freek D. van der Meer

Co-promotor: Dr. Paul M. van Dijk
Int. Institute for Geo-information Science and Earth Observation
Department of Earth Systems Analysis

This doctoral dissertation was produced with the financial support of:

Netherlands Fellowship Programme and ITC
The Netherlands

Leden promotiecommissie	Prof. Dr. S.M. de Jong
	Prof. Dr. S.B. Kroonenberg
	Prof. Dr. M. Hale
	Prof. Dr. J.L. van Genderen
	Prof. Dr. Tian Shuichen

International Institute for Geo-information Science and Earth Observation, Enschede, The Netherlands

ITC dissertation number 153
ITC, P.O. Box 6, 7500 AA Enschede, The Netherlands

University of Utrecht

ISBN 978-90-6164-267-1

-Cover designed by Prasun K Gangopadhyay
Printed by ITC Printing Department

Copyright © 2008 by Prasun K Gangopadhyay

असतो मा सद्गमय |
तमसो मा ज्योतिर्गमय ||

Lead us from untruth to truth,
Lead us from darkness to light of knowledge.

Upanishad, ~2000 BCE

to my family

Contents

List of figures v

List of tables vii

List of symbols ix

List of acronyms xi

1 Introduction 1
1.1 The problem 1
1.2 The concept 2
1.3 Research objectives 3
1.4 Structure of the thesis 4

2 Remote sensing of coalfire and related emissions 5
2.1 Coalfire: the problem and occurrence 5
2.1.1 Properties and burning process of coal 8
2.1.2 Spontaneous combustion of coal 9
2.2 Coalfire detection and monitoring 10
2.2.1 Remote sensing and coalfires 10
2.2.2 Geophysical methods 14

2.3 Worldwide occurrence of coalfires and use of remote sensing 15
2.3.1 Coalfires in Asia and Pacific Region 15
2.3.2 Coalfires in the Americas 19
2.3.3 Coalfires in Europe 20
2.3.4 Coalfires in Africa 20
2.4 Greenhouse gas emissions from coalfires 21
2.5 Conclusions 21

3 Coalmining, coalfire and environment 23
3.1 Introduction 23
3.2 Indian scenario: a case study 25
3.2.1 Study area 25
3.2.2 Environmental impact of coalmining and coalfire 25
3.2.3 Physical impact 26
3.2.4 Socio-economic impact 29
3.3 Chinese scenario: a brief discussion 29
3.3.1 Main environmental problems of Chinese coalmines 31
3.3.2 Mining accidents 33
3.4 Conclusions 33

4 Satellite derived emissivity and coalfire detection 35
4.1 Introduction 35
4.2 Coalfire detection in northern China 37
4.2.1 Study area 37
4.2.2 Methodology 40
4.2.3 Results and discussions 45
4.2.4 The relation between crack and satellite derived temperature 48
4.3 Coalfire detection in eastern India 52
4.3.1 Study Area 52
4.3.2. Methodology 53
4.3.3 Results and Discussions 56
4.4 Conclusions 59

5 Monitoring coalfire using remote sensing 61
5.1 Introduction 61
5.2 Study area 62
5.3 Previous research 62
5.4 Methodology 63
5.5 Results and discussion 67
5.6 Conclusions 71

6 Atmospheric modelling of CO_2 absorption bands for remote sensing applications **73**
6.1 Introduction 73
6.2 Radiative transfer in atmosphere 76
6.2.1 The formal solution 76
6.3 Research approach 79
6.4 CO_2 absorption bands and their suitability analysis 81
6.5 FASCOD simulated models and sensor suitability analysis 84
6.6 Error contributing factors 86
6.7 Conclusions 86

7 Detecting anomalous CO_2 flux using spaceborne spectroscopy **91**
7.1 Introduction 91
7.2 Study area 93
7.3 Research approach 93
7.4 Parameters calculation using FASCOD 95
7.5 Estimating CO_2 concentration using the CIBR method 95
7.6 Estimating CO_2 concentration using inversion method 103
7.7 Error contribution factors 106
7.8 Conclusions 108

8 Synthesis **109**
8.1 Introduction 109
8.2 The concept 110
8.3 Satellite derived emissivity and coalfire detection 112
8.4 Sensitivity analysis of hyperspectral remote sensing sensors 113
8.5 Quantifying CO_2 emissions from coalfires 114
8.6 Concluding remarks 115
8.7 Potential of future research 117

Appendix **119**
A.1 Instrument information 119
A.2 IDL code used in Chapter 5 121

Bibliography **127**
Summary **141**
Samenvatting **145**
Acknowledgements **149**
Biography **151**
Publications **153**

List of figures

Fig. 2.1 The worldwide occurrence of coalfires 7
Fig. 2.2 Historical CO_2 emissions form fossil fuel consumption 7
Fig. 2.3 The phenomenon and data acquisition 12
Fig. 2.4 Smokes coming out from underground coalfire 16
Fig. 2.5 Burnt outcrop of coal seam in Wuda, north China 17
Fig. 3.1 Coalmine refuse land 27
Fig. 3.2 Diversion of small streams due to overburden dumps 27
Fig. 3.3 The Void-Subsidence-Coalfire Nexus 28
Fig. 3.4 A small-scale mine in northern China 29
Fig. 3.5 Air pollution from a coal processing plant, north China 31
Fig. 4.1 Location of the Wuda coalmine area and test sites 37
Fig. 4.2 Generalized cross-section of Wuda syncline 38
Fig. 4.3 Temperature anomaly extraction from ASTER data 45
Fig. 4.4 Temperature comparison of different methods 47
Fig. 4.5 Satellite derived surface temperature and ground truth 48
Fig. 4.6 Satellite derived kinetic temperature and ground data 49
Fig. 4.7 Location of Raniganj coal coalmine area, India 52
Fig. 4.8 Geological settings of Raniganj coal coalmining 53
Fig. 4.9 A mixed pixel of TM6 55
Fig. 4.10 Density sliced surface temperature anomaly map 57
Fig. 4.11 Smoke is coming out from a crack from a coalfire 58

Fig. 4.12	Surface temperature anomaly map and coalfires	59
Fig. 5.1	Location of the study area and test site	62
Fig. 5.2	Different layers of the proposed model	65
Fig. 5.3	Initiation point with coal seams and cracks	66
Fig. 5.4	An overview of the proposed model	67
Fig. 5.5	Effect of different parameters	69
Fig. 5.6	The comparison of processed image and predicted location of coalfires in *average* case	70
Fig. 5.7	comparison of processed image (red) and predicted location of coalfires in *extreme* case	70
Fig. 5.8	Relation between average speed and weighing factor	71
Fig. 6.1	FASCOD simulated mixing ratios of atmospheric gases	79
Fig. 6.2	CO_2 line intensities in HITRAN data base	80
Fig. 6.3	Absorption of CO_2 and H_2O+ in 1.859-2.283 μm region	82
Fig. 6.4	Absorption of CO_2 and H_2O+ in 1.995-2.014 μm region	82
Fig. 6.5	Distribution of significant CO_2 absorption bands.	83
Fig. 6.6	Relation between CO_2 concentration and transmission	83
Fig. 6.7	Noise simulation using central wavelength and FWHM	88
Fig. 6.8	Additive noise simulation in 330 and 570 ppmv	89
Fig. 6.9	Multiplicative noise simulation in 330 and 570 ppmv	90
Fig. 7.1	Location of measurement and reference channels	96
Fig. 7.2	CIBR derived CO_2 (B185 and B186)	97
Fig. 7.3	Relation between surface temperature and CIBR CO_2	98
Fig. 7.4	Relation between temperature range and CIBR CO_2	99
Fig. 7.5	Spatial relation of CIBR derived CO_2 (B185 and B186)	100
Fig. 7.6	Effect of change in radiance at satellite	101
Fig. 7.7	Effect of surface reflectance on CO_2 retrieval	102
Fig. 7.8	Main components of the proposed model	103
Fig. 7.9	Surface temperature and model derived CO_2	105
Fig. 7.10	Spatial relation between surface temperature and model derived CO_2, and CIBR and model derived CO_2	106
Fig. 8.1	The conceptual framework	111

List of tables

Table 3.1 China's Primary Energy Consumption (1980–2000) 30
Table 3.2 Raw Coal Output by Ownership (in million tons) 30
Table 4.1 Comparison of temperatures of different bands (NEM and RCM method) 46
Table 4.2 Comparison of satellite derived and crack temperatures 51
Table 5.1 Weighing factors of different parameters of simulations 68
Table 6.1 Relation between reference and noise added spectra 85
Table 6.2 Relation between reference and noise added spectra with different CO_2 concentration 85
Table 7.1 Correlation between surface temperature and CO_2 concentration (B185) 99
Table 7.2 Correlation between surface temperature and CO_2 concentration (B186) 100
Table A.1 Characteristics of the Hyperion System 119
Table A.2 On-orbit Performance of the Hyperion Instrument 120
Table A.3 Characteristics of Hyperion bands of interest 120

List of symbols

Symbol	Interpretation	Unit
L	Radiance	watt m^2 sr^{-1}
τ	Transmissivity	-
ε	Emissivity	-
$s\downarrow$, L_{Sun}	Solar irradiance	watt m^2
α, β, k	Coefficients	-
θ_S	Solar zenith angle	Degree
ρ	Reflectance	-
T	Temperature	K
L_m	Measurement channel	-
L_r	Reference channel	-
T_R	Radiance temperature	K
T_K	Kinetic temperature	K
s	General point among the path	-
s_0	Boundary	-
d	Earth-Sun distance	Astronomical unit
l	Wavelength	nm, µm
Ω	Solid angle, resistivy	sr, Ohms
ϕ, q	Angle	Degree

List of acronyms

ASTER	Advanced Spaceborne Thermal Emission and Reflection Radiometer
AVHRR	Advanced Very High Resolution Radiometer
BIRD	Bi-spectral Infra-Red Detection
BRSC	Beijing Remote Sensing Corporation
CIBR	Continuum Interpolated Band Ratio
DLR	Deutsche Zentrum für Luft- und Raumfahr
EMS	Electro-magnetic spectrum
EO-1	Earth Observation 1
ETM+	Enhanced Thematic Mapper
FASCOD	Fast atmospheric signature code
FWHM	Full width at half maximum
GHG	Green house gas
GMS	Geostationary Meteorological Satellite
GOES	Geostationary Operational Environmental Satellites
GOMS	Geostationary Operational Meteorological Satellite
HITRAN	High resolution transmission
HWHM	Half width at half maximum
INSAT	Indian National Satellite
Modtran	Moderate resolution transmission
NOAA	National Oceanic and Atmospheric Administration

OMIS	Optical Module Imaging System
PBL	Planetary boundary level
PLSR	Partial least square regression
ppmv	Parts per million volume
SWIR	Shortwave infrared
TABI	Thermal airborne broadband imager
TIMS	Thermal Infrared Multispectral Scanner
TOA	Top of the atmosphere
VNIR	Visible near infrared
NEM	Normalized emissivity method
RCM	Reference channel method

Chapter 1

Introduction

1.1 The problem

Coalfires are common problem in most coal producing countries. In most cases a coalfire is initiated naturally, i.e. by spontaneous combustion or induced by humans (e.g. accidents, improper mining method and unauthorized mining). Other than the loss of a non-renewable energy source, coalfires promote several environmental problems including GHG (green house gas) emissions, subsidence and the increment of surface temperature.

Since the 60s remote sensing has been used as an efficient tool to detect and monitor coalfires. Over time, remote sensing technology has been improved such that more reliable information form the Earth's surface and atmosphere can be received. Remote sensing of coalfires was mostly based on fixed emissivity whilst extracting kinetic surface temperature in order to conduct a quantitative study. An estimation of surface emissivity can return more reliable surface temperature results, leading to a better understanding of coalfires. The first part of this research has explored the possibilities of satellite derived emissivity for surface temperature extraction for a better understanding of coalfires.

Due to human activity and geo-natural events, CO_2 has increased in the atmosphere since the pre-industrialization era and increased the radiative forcing to 1.46 w m^{-2}. CO_2 is the prime GHG that is emitted from coalfires along with other gases such as CO, CH_4, SO_x and NO_x. According to some studies, the CO_2 emission from Chinese coalfires is somewhere between 0.3 – 3% of total emission from the world's fossil fuel. In the NIR to SWIR part of EMS CO_2 has few narrow absorption bands with frequent interference of other atmospheric species such as H_2O. A remote sensing sensor, that acquires information from TOA (top of atmosphere) or middle of atmosphere, will be affected in particular wavelength in a changing concentration of CO_2. In this range, the spectral signature acquired by a sensor is a combined product of surface reflected/emitted energy and CO_2 absorbed/radiated energy. A high spectral resolution sensor can *see* this change of CO_2 concentration more closely. The core part of this research focuses on this problem; in order to develop a remote sensing based model to estimate CO_2 emissions from coalfires.

1.2 The concept

The main source of energy that drives the Earth's climatic system is radiation from the sun. About 50% of this radiation is in the visible short-wave part and rest is in the near-infrared part of the electromagnetic spectrum. Throughout the year, the Earth's surface receives an average of 342 watts of solar radiation, 31% of which is immediately reflected back into space by clouds, the atmosphere and the Earth's surface. The remaining energy is absorbed by the Earth and its atmosphere, and as such increases the Earth's surface temperature, which is later radiated back into space with a longer wavelength and partly as sensible heat and water vapour (as latent heat during cloud drop formation).

The Earth's atmosphere contains several trace gases which absorb and then radiate in the infrared part of the spectrum. These GHGs in the atmosphere absorb infrared radiation, emitted by the earth's surface, the atmosphere and clouds and then re-emit infrared radiation in all directions. This phenomenon forces the Earth's surface temperature to increase to a much higher average temperature of 287 K.

Increased human activity (fossil fuel burning, cement production and

deforestation) and geo-natural hazards (volcanism, leakage from hydrocarbon reservoir and coalfire) have increased the CO_2 concentrations in the atmosphere.

Among the all other geo-natural hazards, spontaneous combustion of coal is unique in nature and common in most coal producing countries. Coalfires can occur in coal seams and stockpiles of coal in ambient temperature under certain conditions, such as: coal type and effective area (fine particles), exposure to air and moisture content.

Except consuming a non-renewable energy resource, coalfires contribute to a significant amount of GHGs in the immediate and regional atmosphere. These GHGs (especially CO_2 and methane) in the atmosphere is the main reason for the *global warming* phenomena. Other than gaseous emissions, coalfires increase the aerosol loading in the local environment. Coaldust and ashes are usually deposited in the nearby agricultural fields, in housing areas and in the water resources by wind and also increase toxic elements in the food chain.

In order to avert a major environmental disaster in the near future, it is very important to monitor and control CO_2 emission in the atmosphere. A reliable space borne estimation of CO_2 emission can identify these anomalous sources to ensure proper planning and measures.

1.3 Research objectives

The principal question of this research is how remote sensing can be used for atmospheric CO_2 retrieval emitted from geo-natural events such as coalfires.

The following research objectives are defined:

- to use satellite derived emissivity in order to retrieve reliable surface temperature readings for a better understanding of coalfires.
- to evaluate present hyperspectral sensors sensitivity in a changing CO_2 concentration by means of simulation.
- to evaluate band ratioing method for column atmospheric CO_2 retrieval and develop an new remote sensing based model to quantify CO_2 emission from coalfires.

1.4 Structure of the thesis

This thesis consists of eight chapters. All six core chapters have been or are to be published as peer-reviewed articles in journals (chapters 3, 4, 6 and 7) or in books (chapters 2 and 5).

Chapter 2 defines the problem of coalfire, the process and related gaseous emissions. It also provides a detailed study of worldwide occurrence of coalfires and application of remote sensing in coalfire study.

Chapter 3 introduces the main environmental problems related to coal mining and coalfires. A coal mining region in eastern India was taken as the study area.

Chapter 4 discusses the applicability of remote sensing to detect and monitor coalfires in two study areas, one is in north China and other is in eastern India. In this chapter, the use of satellite derived emissivity is discussed in order to extract more reliable surface temperature readings.

Chapter 5 proposes a model based on multitemporal images and simulation with the inputs from the local geological setting and ground knowledge to predict the vector of a coalfire.

Chapter 6 discusses the radiative transfer in the atmosphere and use of a radiative transfer code to identify most suitable CO_2 bands for atmospheric CO_2 retrieval using hyperspectral remote sensing sensors. A sensitivity study of different hyperspectral sensors is also presented with different noise scenarios.

Chapter 7 verifies the suitability of band ratioing method for atmospheric column retrieval of CO_2 in a coalfire affected area in north China. A model is proposed based on radiative transfer in the atmosphere for CO_2 retrieval from coalfires. This model first establishes a relationship between radiance at the satellite and the CO_2 plume related radiance, and finally the inverse of the CO_2 radiance in CO_2 concentration (ppmv).

Chapter 2

Remote sensing of coalfire and related emissions*

2.1 Coalfire: the problem and occurrence

Minerals constitute the backbone of the economic growth of any nation, and coal is one of the most easily accessible minerals that is used as a primary energy resource in most parts of the world. Total recoverable reserves of coal around the world are estimated at 1,083 billion tonnes, which is enough to last ~210 years at current consumption levels. Although coal deposits are widely distributed, 60% of the world's recoverable reserves are located in three countries: the United States (25%), the former Soviet Union (23%), and China (12%). Australia, India, Germany, and South Africa account for an additional 29% (Goddard Space Flight Center, 2006). However, one of the most primitive uses of coal by humans (~75,000 years ago) was found in France (Théry *et al*., 1996), and one of the earliest coalfires was revealed by Goldammer and Seibert (1989), using the thermoluminescence of baked rocks close to a coal seam in East Kalimantan, which was dated back to ca. 13 ka.

*This chapter is based on the following article: Gangopadhyay, P.K. (2007) Application of remote sensing in coal - fire studies and coal - fire – related emissions. In: Geology of coal fires : case studies from around the world, Editor. G.B. Strachter. Boulder : Geological Society of America (GSA), pp. 239-248.

Subsurface and surface coalfires are a serious problem in many coal-producing countries. Combustion can occur within the coal seams (underground or surface), in piles of stored coal, or in spoil dumps at the surface. The fires in coal seams can be initiated spontaneously under certain conditions, where air, heat (from sun), and water vapour are the main constituents. Lightning and forest/bush fire can also initiate a coalfire. In some cases, human negligence, a mine accident, or a human-induced heat source could be the reason for a coalfire (Sinha, 1986). Coalfires are common in many coal-producing countries, such as China, India, Indonesia, the United States, Australia, South Africa, and Russia (Fig. 2.1) (Ellyett and Fleming, 1974; Saraf *et al*., 1995; van Genderen *et al*., 1996; Walker, 1999; Tetuko *et al*., 2003; Stracher and Taylor, 2004).

Significant environmental and economic problems are associated directly and indirectly with coalfires. Some of the impacts of coalfires are listed below.

- A coalfire pollutes the immediate environment by emitting toxic gases, such as CO, CO_2, NO_x, SO_x, and CH_4. Among these noxious gases, CO_2 and CH_4 contribute to global warming.
- Land subsidence is a common event in areas that are affected by subsurface coalfires, which lead to a change in the local drainage pattern.
- Heat radiation from a coalfire increases the local temperature.
- A coalfire increases the cost of production by making existing mining operations difficult.
- A coalfire consumes the most used and potentially valuable energy resource.
-

Several researchers suggested that the concentration of CO_2 in the atmosphere has increased unambiguously since the Industrial Revolution (Etheridge, *et al.*, 1996; Keeling and Whorf, 1999). Derived from historical data, based on energy source, the total CO_2 emission in the global atmosphere has increased at an alarming rate (Andres *et al.*, 1999). Fig. 2.2 shows a reconstruction of past emissions of CO_2 from fossil fuel combustion since ca. 1750. Other researchers have confirmed that the current CO_2 concentration has increased to 375 ppmv, which increased the radiative forcing to 1.46 w m^{-2} (Ramaswamy, *et al.*, 2001).

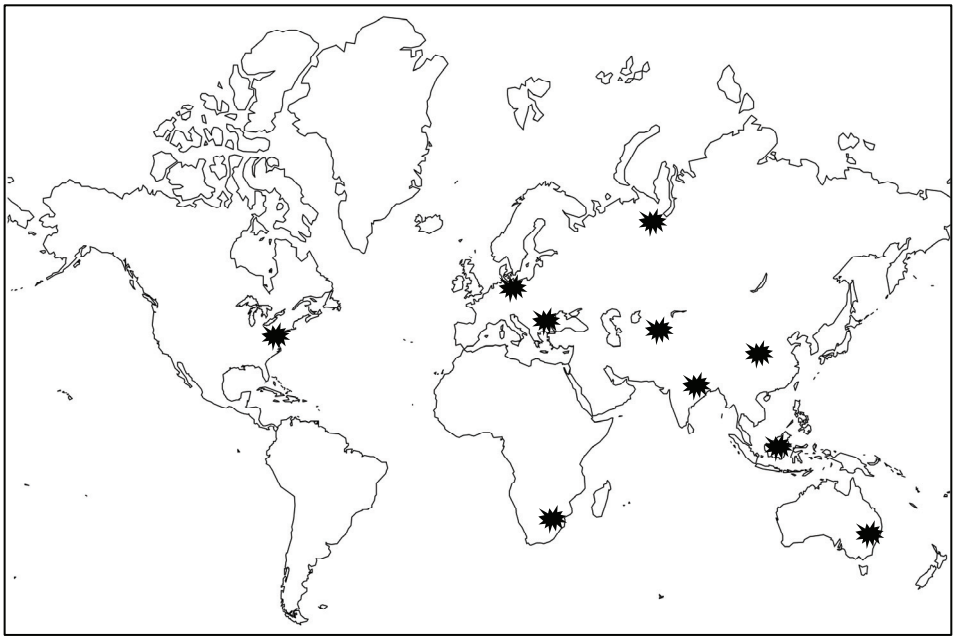

Fig. 2.1: The worldwide occurrence of coalfires.

In addition to CO_2, CH_4 and NO_2 are significant GHGs that are emitted from coalfires. Both of these GHGs have increased at a significant rate. Atmospheric methane (CH_4) concentration has increased by about 150% (1,060 ppbv) since 1750, whereas the NO_2 concentration has increased by 16% (46 ppbv) (Ramaswamy, *et al.*, 2001).

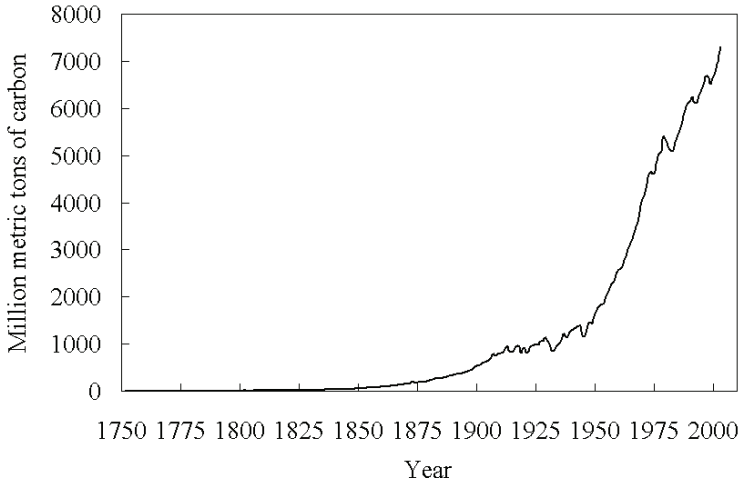

Fig. 2.2: Historical CO_2 emissions form fossil fuel consumption (data source: EIA 1, 2006).

The focus here is on the global distribution of coalfires with emphasis on remote sensing used for the detection, monitoring, and quantification of coalfire related emissions.

2.1.1 Properties and burning process of coal

Coal, the most used fossil fuel, is a readily combustible rock that contains more than 50%, by weight, of carbonaceous material, and is formed by the compaction and indurations of variously altered plant remains. Initially, these remains were deposited in a swampy basin in the form of peat. Unpredictable amounts of other chemicals (e.g., sulphur, chlorine, sodium) and other minerals can be found in coal. The physical properties of coal, such as colour, specific gravity, and hardness, vary considerably. This variance depends on the composition and the nature of preservation of the original plant material that formed the coal; the amount of impurities in the coal, derived from soil and silt that were deposited with the parent material; and the amount of time, heat, and pressure that has affected the coal since it was formed. Time, heat, and pressure also determine the degree of maturation of the sequence, which, according to the increasing amount of carbon, is classified as lignite, sub-bituminous coal, bituminous coal, or anthracite. Rank is another index of coal quality. This is a measure of the brightness (reflectivity) of the coal as measured microscopically, and is a function of the vitrinite content one of the microlithotypes in coal (Williams, D.J., 2005: personal communication).

Combustion of coal is a chemical process that can be defined in a simplified form as:

$$\text{Coal} + O_2 \rightarrow CO_2 + \text{Energy} \qquad (2.1)$$

Practically, it is more complicated and may consist of different stages, which also depend on the presence of other substances (eg, water [vapour], pyrite). For dry coal, the overall reaction was described by Schmal (1987), referencing Kok (1981) as:

$$C_{100}H_{74}O_{11}+113\ O_2 \rightarrow 100\ CO_2+37\ H_2O+4.2\times10^8\ \text{J/kmol}\ O_2 \qquad (2.2)$$

The first part of the reaction, which consists of the chemical absorption of oxygen by the coal surface, can be presented in the following equation:

$C_{100}H_{74}O_{11}+17.5\ O_2 \rightarrow C_{100}H_{74}O_{46}+2.5\times10^8$ J/kmol O_2 (2.3)

Several factors can accelerate or decrease the speed of the reactions (e.g., oxygen content of air, exposed surface area of the coal, temperature, composition of coal).

2.1.2 Spontaneous combustion of coal

The potential for coal to spontaneously combust depends on its aptitude of oxidization at ambient temperature in certain conditions (Fig. 2.3). This occurs through the *absorption* of oxygen at the surface of the coal, and is an exothermic reaction. The temperature of the coal may start to increase. If the temperature reaches what often is called the 'threshold' temperature somewhere between 353 and 393 K, a steady reaction results in the production of gaseous products, such as CO_2. The temperature of the coal almost certainly will continue to increase until, somewhere between 503 and 553 K, the reaction becomes rapid and strongly exothermic (i.e., the coal reaches *ignition* or *flash* point and starts to burn).

Not all types of coal are equally susceptible to spontaneous combustion. High-ranking coals (high carbon content) are more fire prone than lower ranking coals; however, the exact reasons are unclear. Another important factor is the size of the particles; the larger the effective area of the coal (fine particles), the more rapidly the reaction can proceed.

External factors also play a role in the oxidation reaction. Oxidation requires an adequate supply of air; cracks, fissures, and the porosity of rock and soil over the coal seams may encourage underground coalfires by allowing oxygen to reach the coal. A very rapid airflow may remove the heat so rapidly that the coal never reaches the combustion temperature. Conduction through the coal itself and the surrounding rocks can also remove the heat. Nevertheless, in general, the thermal conductivity of coal is quite poor. The removal of heat is the only likely way to stop the process (of burning) in the initial stages of the oxidation reaction. Once the threshold temperature is reached and the second stage of the reaction begins, heat usually is generated at too great a rate and the temperature of the coal will continue to increase until combustion starts.

The presence of water (vapour) also has some important effects. Coal

with very high or very low moisture content tends to exhibit a low oxidation rate. However, a minimum amount of water is considered necessary for the reaction to continue (Banerjee, 1985; Schmal, 1987).

Depending on the influencing factors, a coalfire can initiate in an outcrop of coal seams at the surface. Rosema *et al.* (1999) defined an open fire as a coalfire that burns in direct contact with the atmosphere, usually with visible flames. Other than in exposed seams of coal, fire can occur in stockpiles or spoil dumps. In the case of a subsurface coalfire, the required oxygen enters through cracks/fissures at the surface or mine shafts. However, the coalfire can cause subsidence as it voids the support (coal seam) beneath the overburden rock and makes sufficient passage for *breathing* such that combustion may continue.

2.2 Coalfire detection and monitoring

It is obvious that a surface coalfire can be detected easily; however, a subsurface coalfire can burn over time without any surface activity. Before the introduction of remote sensing for the study of coalfires, borehole measurement was one of the popular methods that were used to identify coalfires. Although this method can be used to measure the temperature of a coal seam that is suspected to be affected by fire very accurately, it is not feasible for use over a large area.

Despite the fact that remote sensing already was being used for earth observation, in the early 1960s it was used first for a coalfire study with an airborne thermal scanner. With time the technology and quality of thermal remote sensing has improved and so has its use. Some established geophysical methods also are used for coalfire study.

2.2.1 Remote sensing and coalfires

Aerial photography based on remote sensing was introduced by the end of the nineteenth century, and was used mostly for reconnaissance purposes. Satellite-based remote sensing began in 1960, but it was not accessible to civilians until 1972. With time, remote sensing has evolved dramatically. Remote sensing involves the following components:

- Energy source - illuminates or provides electromagnetic energy to the target of interest.
- Radiation - energy travels from its source to the target.

- Interaction with the target - depends on the properties of the target and the radiation.
- Interaction with the atmosphere - reflected and radiated energy from the target is transmitted through, and interacts with the atmosphere.
- Recording of energy at the sensor - a sensor collects and records the transmitted electromagnetic radiation.
- Reception and processing - the data recorded by the sensor are received at a ground station where they are processed into an image and distributed.
- Interpretation and analysis - the processed image is interpreted, visually and/or digitally, in order to extract information about the target which was illuminated.
- Application - the final element of the remote sensing process is achieved when it reveals new information or assists in solving a particular problem.

The 3 to 14 μm region of the electromagnetic spectrum (EMS) is referred to as the thermal infrared region (Lillesand and Kiefer, 2000). Thermal remote sensing uses atmospheric windows in the 3 to 5 μm and 8 to 14 μm regions only, because these parts of the EMS are not affected as much by atmospheric interaction.

Thermal-infrared sensing exploits the fact that everything above absolute zero (0 K or -273 C) emits radiation in the thermal infrared range of the EMS. The thermal infrared radiation of an object is controlled mainly by its emissivity, geometry, and temperature. Thermal infrared sensors record differences in the received infrared radiation from various objects. Because these differences often are considerable, an infrared image can exhibit a wide range of contrasts. The sensors that are carried by aircraft or spacecraft, which are sensitive to this (infrared) region, provide a possible means of making synoptic measurements of land surface temperatures. The relationship between the radiated energy that is recorded by the sensor and the temperature of the surface can be drawn by Planck's distribution function.

All over the world, many commercial and research scanners (air- and satellite borne) are acquiring data in the thermal infrared region (3-5 μm and 8-14 μm). Numerous thermal airborne scanners (e.g., Daedalus [8.5-15.5 μm, USA], TIMS [8.2-12.2 μm, USA], Aries [France], Digital Thermal

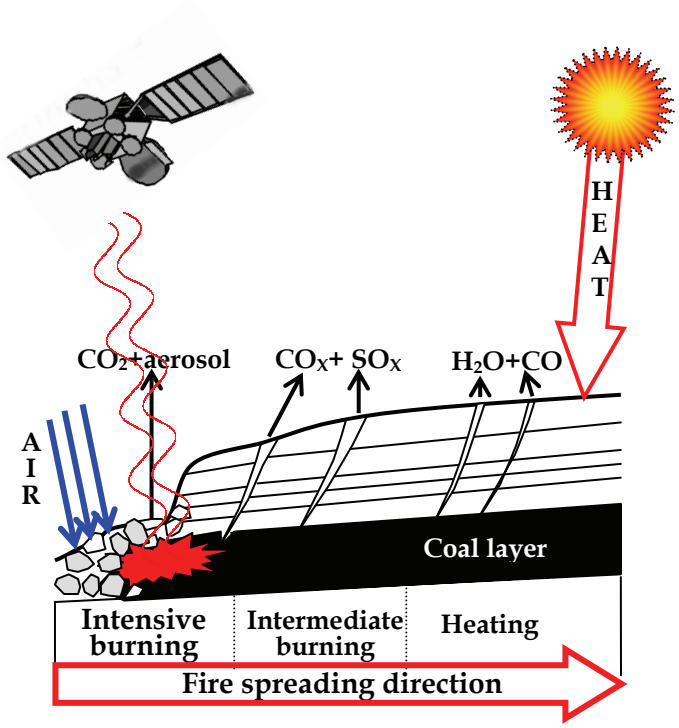

Fig. 2.3: The phenomenon and data acquisition.

Linescanner [8-14 µm, UK], TABI-320 [8-12 µm, Canada], OMIS1 [8.08-12.4 µm, China]) and several other thermal scanners are operating in different countries with many applications, such as coal, forest or bush fire detection and monitoring, surveillance, and reconnaissance. Airborne operations are not as cost effective as a satellite-based operation when monitoring a broad area. Satellite-based Earth observation thermal scanners operate from two types of platforms: polar orbiting and geostationary. Among polar-orbiting satellites, Landsat7 ETM+ band 6 thermal data has 60-m spatial resolution, which is the highest of the commercially available satellites. Presently, Landsat7 is nearly non-functional because of scanner failure. However, another useful spaceborne thermal scanner is ASTER, which is on board the TERRA satellite. With five channels in the thermal infrared region (8.125–11.65 µm), it provides an opportunity to estimate emissivity values from the satellite data directly, which is very crucial for the quantitative thermal study of the Earth's surface. For a large area, the AVHRR instrument (on the NOAA series of polar-orbiting satellites) is recording the Earth's surface thermally with a spatial resolution of 1.1

km. Among the small satellite series, BIRD (DLR, Germany) has two scanners to detect hot spots on the Earth's surface: one in the mid-infrared range (3.4-4.2 μm) and another in the TIR (thermal infrared) range (8.5-9.3 μm). Although the spatial resolution is coarse (290 m) but with a high quantization level (14 bits), BIRD data are quite useful for detecting temperature anomalies over the Earth's surface. MODIS (NASA) is currently acquiring data in the thermal infrared region (spatial resolution 1 km), which are being used in many applications in meteorology and earth observation. Many geostationary satellites, such as GOES (NASA), Envisat, Eumetsat and Meteosat (ESA), INSAT (India), GOMS (Russia), GMS (Japan), and Feng-Yun (China), are gathering data about cloud-top temperature for weather prediction. Some of these satellites also are being used for forest fire monitoring because of their very high temporal resolution (Maathuis, B., 2005: personal communication).

When present as flaming combustion on the surface, coalfires emit significant thermal energy that is easy to detect by any thermal remote sensing scanner. However, the surface heating is comparatively subdued with a subsurface coalfire, and may be masked by daytime solar heating. In that case it is necessary to use nighttime remote sensing data to reveal and measure the extent of heating. There are three steps in the use of remote sensing in order to detect a coalfire:

1. Acquisition of a thermal image (preferably night) of the area under investigation using remote sensing and processed digitally to create a surface temperature map in order to reveal the temperature anomalies,
2. Acquisition of information about the local geological setting, temperatures of coalfire vents, and different land cover types through field survey,
3. Use of the geological and other field knowledge to eliminate anomalies, other than coalfires, to produce a final temperature map that is calibrated with temperatures that were collected in the field.

The atmosphere between the object (coalfire) and the receiver (remote sensor) plays a significant role in the accuracy of the surface temperature estimation, especially in quantitative studies. The temperature of the surface over a coalfire depends on several factors, such as inherent

properties (emissivity, fire temperature) and the conditions of the surrounding areas (soil type, topography, local atmosphere, crack or fissures on the surface, depth of fire).

Soil moisture and wind also affect the surface temperature. The thermal properties of rock also are significant factors in thermal remote sensing. For example, some high thermal inertia rocks can appear as coalfires in nighttime images because they trap the heat longer compared with other rocks. However, predawn data acquisition and a good knowledge of the local geological setting can exclude these false anomalies.

Although satellite remote sensing is established as a matured technology in the field of coalfire detection and monitoring, few constraints (e.g., direct comparison between satellite-derived temperature and field measurements) have been overcome to an extent. In general, coalfires are a very local phenomenon, and, in many cases, they are not large enough to saturate a whole pixel to appear as an anomaly in comparison with the background. The aggregated temperature of a pixel depends on the location, spread, surface type, and temperature of the fire/crack and its surroundings. For example, an ASTER pixel is large enough (90 m) to accommodate a few cracks with active fire, local rocks, and (sometimes) sparse vegetation. These different types of landcover may have different temperature ranges to influence each other and finally appear as an anomaly or background with a certain pixel integrated temperature value. Also, the viewing angle, foot print, field of view of sensor, distance from the object, and operating range (wavelengths) can determine the final pixel integrated temperature.

2.2.2 Geophysical methods

In addition to borehole measurements and remote sensing, some established geophysical methods are being used for coalfire detection and monitoring. However, these methods are point-based measurements and errors are to be expected during their interpolation.

The radioactive method is based on the fact that sedimentary rocks contain radioactive elements, such as uranium ($^{235}U_{92}$, $^{238}U_{92}$) and thorium ($^{232}Th_{90}$). These radioactive elements emit α particles during decay. During this process, they are transformed into radon $^{222}Rn_{86}$, $^{220}Rn_{86}$, $^{219}Rn_{86}$), which has a half-life of 3.96 seconds to 3.825 days. The concentration of α particles depends on the temperature (i.e., if the

temperature is higher, then the transportation of α particles is also higher). Pressure, porosity, and water content also influence the transportation.

Another method that is used is the resistivity method. The resistance of rock is calculated by using a few electric poles, measuring the resistance in ohms (Ω) per metre, and comparing these with the standard value. Under normal conditions, the resistance of sedimentary rock is 600 to 800 Ω m^{-1}, but in burnt rock it increases to 1200 to 3000 Ω m^{-1}, because of high porosity, cracks, and low water content.

2.3 Worldwide occurrence of coalfires and use of remote sensing

Coalfires, which are a common problem in most coal-producing countries, have a very long history (Fig. 2.1). The oldest coalfire is nearly two million years old (Early Quaternary), and is found near Urumqi in northwest China (Zhang *et al*., 2004). There also are some reports about a historic coal seam fire in Indonesia, which probably was started by a lightning strike. In countries where coal mining is a major industry, coalfires are inevitable; some were responsible for mine disasters and were short-lived, others burned for considerable periods of time. Major fires, largely uncontrolled, are burning in China, India, and the Unites States. The following sections describe the worldwide occurrence of coalfires and remote sensing–aided coalfire detection and monitoring-related research.

2.3.1 Coalfires in Asia and Pacific Region

2.3.1.1 Coalfires in India

The Raniganj coal belt, West Bengal, the oldest and largest coal field in India, belongs to the Gondwana Supergroup 1. With an area of about 1260 km^2, the Raniganj coal belt is located about 200 km west of Calcutta, West Bengal. Underground fires have been known there for the past 100 years or more (Fig. 2.4). Some surface fires also are evident in some opencast mines. Based on Landsat5 thermal data and local knowledge, the coalfire areas were identified in the Raniganj coal belt (Gangopadhyay *et al*., 2005a).

The neighbouring sickle-shaped Jharia coal field, which is the only coking coal source in India, lies in the Dhanbad district in the Jharkhand state of India. With an area of 700 sq km, it is located ~250 km northwest of Calcutta. Coalfires are common phenomena in Jharia, that generally increase the temperature of the surrounding areas, and render the whole region dangerous for inhabitants and unfit for cultivation (Prakash *et al.*, 1997).

Fig. 2.4: Smokes coming out from underground coalfire in RCB, India.

Aided by remote sensing, many researchers, such as Bhattacharya e*t al.* (1991), Cracknell and Mansor (1992), Reddy *et al*. (1993), Saraf *et al*. (1995), and Prakash *et al*. (1997), have studied the Jharia coalfires. In 1991, Bhattacharya *et al*. used airborne predawn thermal infrared and daytime multispectral images to distinguish the coalfires from the background. Another attempt to detect the coalfire was made by Mukherjee *et al*. (1991), using predawn airborne thermal data. They also attempted to estimate the depth of the fire using a linear heat flow equation. Cracknell and Mansor (1992) first used Landsat-5 TM and NOAA-9 AVHRR data, and found that nighttime NOAA data were quite useful to isolate the warm areas from the background. Reddy *et al*. (1993) used the short-wave infrared (SWIR) region of the EMS, which is covered by Landsat TM bands 4, 5, and 7. Using Landsat TM bands 6 and 7, Saraf *et al*. (1995) established a relation between high-temperature events and surface fires. Later, Prakash *et al*. (1997) used the Landsat TM TIR and SWIR bands to identify surface and subsurface fires separately. Based on a dual-band approach using TM data, Prakash and Gupta (1999) attempted to calculate the area of surface fires.

2.3.1.2 Coalfires in China

Coalfires in China originate at the outcrop of coal in the surface and underground, and have natural and manmade origins (Fig. 2.5). It is estimated that up to 200 million tons of high-quality coal are lost every year, mostly in the northern half of China (Rosema *et al.*, 1999). In 1991, Huang *et al*. studied the extent of coalfires using Daedalus data, and presented an alarming picture of Chinese coalfires. Since 1986, several researchers have worked on coalfires in Xinjinag and Ningxia Hui regions. In 1995, Yang identified several coalfires in these areas using predawn airborne thermal scanner data. Later, Wan and Zhang (1996) carried out a detailed study in the same area. They used daytime Landsat TM band 6 data to estimate the relative amount of solar illumination during the overpass time, which was used to correct the effects of terrain. To detect smaller coalfires from Landsat 5 thermal band data (spatial resolution 120 m), Zhang *et al.* (1997) used a sub-pixel temperature estimation method. Cassels (1998) attempted to model an underground coalfire in the Kelazha area of northern China with input from a three-dimensional geological model. By analyzing the SWIR spectra of rocks, Zhang (1996) identified the burnt rocks, which also are an indication of coalfire. In 1997, Wang (2002) identified areas that were affected by coalfires with ASTER and Landsat TM data in Xinxiang province.

Fig. 2.5: Burnt outcrop (white part) of coal seam in Wuda, China.

In the Wuda mining region, in Inner Mongolia, an extensive study was done on coalfire, using satellite-derived emissivity, which returns a more reliable surface temperature (Gangopadhyay, 2003; Gangopadhyay *et al*., 2005a). Because emissivity values vary with landcover, satellite-derived emissivity values can increase the accuracy of quantitative study of coalfires.

2.3.1.3 Coalfires in Australia

Although Burning Mountain in Australia has been known for a long time, the first recorded observation was in 1828 after its discovery by a local farmer (Anon, 1972). In 1829, and again in 1831, these fires were mapped with a detailed description by the surveyor general, T.L. Mitchell (Mitchell, 1839). In 1918, Abbott recorded detailed information about this phenomenon concerning the movement of the main vent area (Abbott, 1918). In addition, Bunny (1967) and Rattigan (1967a, b) made detailed and careful contributions on the study of the Burning Mountain coalfire. A notable study was produced by Fleming (1972), which suggested that the fires could have been burning since the Pleistocene. Later, Ellyett and Fleming (1974) did an extensive study using a Daedalus thermal airborne scanner that operates in the 8-µm to 14-µm region. Today, that fire is more than 152 metres underground, and is still burning the coal slowly. Fires also occur spontaneously in opencast coal mines in many locations, such as Hunter Valley (New South Wales) and the lignite mines in Victoria and South Australia (Williams, D.J., 2005: personal communication).

2.3.1.4 Coalfires in Indonesia

Slash and burn (forest clearing by fire) is a popular and easy method by which to claim cultivation land from forests in Kalimantan (Borneo) of Indonesia; these fires sometimes burn out of control and ignite the coal seams that are exposed nearby. These fires can be very difficult to extinguish because they often ignite in the peat layer. In the same area, Tetuko *et al*. (2003) studied the burnt coal seams in order to estimate the thickness of the fire scar using synthetic aperture radar. In East Kalimantan, baked rocks were found close to a coal seam, which could be evidence of an ancient coalfire. The existence of coalfires in southern Sumatra is also familiar to the community that researches coalfires, and it has been assumed that these ancient coalfires were ignited by lightning. A combination of forest fire, frequent lightning, and warm climate create a favourable situation for spontaneous combustion in coal.

A recent study by Whitehouse and Mulyana (2004) estimated that between 760 and 3000 coalfires are currently burning in east Kalimantan.

2.3.1.5 Coalfires in Russia and the former Soviet Union States

Like other coal-producing countries, Russia also has a problem with coalfires. In addition to spontaneous combustion, some coalfires are initiated by explosion of trapped methane and human errors (Interfax, 2004; Reuters, 2005). In 1998, 74 coalfires were reported in Russia (Walker, 1999). Kyrgyzstan, a former USSR state, also has been stricken by coalfires, which is evident in the Issyk-Kul region (Reuters, 1998). Nevertheless, no open literature is available that reports on the application of remote sensing to the detection and monitoring of coalfires in Russia and the former Soviet Union states.

2.3.2 Coalfires in the Americas

2.3.2.1 Coalfires in the United States

Coal mining started in Pennsylvania mainly to make coke for iron smelting. The first coalfire was reported in 1772; in 1869, it turned into a major disaster and claimed the lives of many miners (Glover, 1998; Stracher and Taylor, 2004). Finally, it extinguished itself about a year after an attempt to pour water into the mine failed. The Pennsylvanian fire adversely affected the local flora and fauna, and was a major acid rain producer in the United States (Glover, 1998). Many underground coalfires continue to remain poorly documented because they are unprofitable, intangible, and unpredictable. The Centralia mine fire in Pennsylvania has been burning since 1962 and is one of the worst mine fires in the United States (Geissinger, 1990; Memmi, 2000).

In 1962, the U.S. Bureau of Mines reported a total of 223 coalfires all over the United States (Slavecki, 1964). The United States was the first country to apply remote sensing to coalfire detection. Using the 'Reconofax' thermal scanner on an airborne platform, Slavecki (1964), Fisher and Knuth (1968), and Greene *et al*. (1969) studied fires on waste coal and subsurface coalfires in the state of Pennsylvania, () where issue of coalfires remains a serious problem. Greene *et al*. also studied the depth of fire, and they classified fires into three types according to their depth: shallow fires (≤10 m deep), intermediate fires (10–30 m deep), and deep fires (>30 m deep).

2.3.2.2 Coalfires in Canada and South America

Bustin and Mathews (1982, 1985) reported about a burning coal seam in southeastern British Columbia, Canada. They found that the upper 3m of the coal seam is being consumed and the fire is advancing along the strike of the coal seam. They also found that some vents in the burnt out zones are being used as air intakes.

Some coalfires in Venezuela and Argentina, which were initiated mostly by human errors, have been reported by news agencies (Reuters, 2004). Other than these news agency reports, no open scientific documents exist that confirm coalfire study using remote sensing in these countries.

2.3.3 Coalfires in Europe

The occurrence of coalfires in mines and stockpiles in many coal-producing countries, such as Germany, Poland, Bulgaria (Walker, 1999) and Romania (Rădan and Rădan, 1998), have been reported by different researchers. In addition, some coal seam fires were reported by Walker (1999) near the Poland–Czech Republic border. One of the biggest coalfire–related accidents in Serbian (then Yugoslavia) mining history happened in 1989 and claimed 92 lives. This coalfire was initiated by a trapped methane explosion that took a long time to extinguish (AAS, 1989). Coalfire is a known phenomenon in Ukrainian coal mines. One of the biggest coalfire–related accidents claimed 33 lives in recent years (Interfax, 2002). A very recent coalfire has been reported in the Svea Nord mine on the Arctic island of Spitsbergen, off Norway, which was initiated by human negligence. The fire had a width of 1 km and took several weeks to extinguish (APN, 2005). An unconfirmed Internet-based source reports about the use of a thermal (airborne) scanner in Germany for monitoring (stockpile) coalfires, but there is no reviewed report available.

2.3.4 Coalfires in Africa

The occurrence of fires in South African underground coal mines was observed for a long time. In addition to South Africa, there are some web-based reports about stockpile or spoil dump fires in Zimbabwe, Botswana, Mozambique, and Zambia. An underground coalfire in one of the Anglo coalmines had been burning for the last few years, but was extinguished recently (Kooij, M., 2005: personal communication).

2.4 Greenhouse gas emissions from coalfires

Over The Past Two Centuries, The Anthropogenic Emissions Of greenhouse gases (GHGs) have increased, which have led to an alarming situation. This steady increase in GHGs in the atmosphere acts as a blanket that retains solar radiation in the atmosphere and has led to global warming. Among all of the GHGs, CO_2 plays a significant role in this phenomenon. Since the pre-industrial era, the concentration of CO_2 has increased from 280 ppmv to 375 ppmv (IPCC, 2001). In this linear increase in the concentration of CO_2, coalfires contribute a significant amount. The GHGs, emitted from all sources, have increased the global mean surface air temperature between approximately 0.3°C and 0.6°C since the late nineteenth century, and have caused serious consequences for low-lying coastal areas (EIA 2, 2006).

The impact of coalfires on climate change and their contribution to global warming are getting increasing amounts of expert attention. Recent coalfire studies on China, one of the major producers of coal, estimate that the country contributes 0.3% (Voigt *et al*., 2004) to the total world annual output of CO_2 that is caused by fossil fuels. Some previous studies suggested this amounts to 3% of the world's total (Rosema, 1995), neither of which is a negligible amount. However, the aforementioned estimates are based on indirect methods, such as the total coal burnt in a certain area. The CSIRO's department of Energy Technology in Australia found an empirical relationship between airborne infrared thermography and GHGs emission from Australian coal mines (Williams, D.J., 2005: personal communication). Some hyperspectral remote sensing–based methods are being developed that exploit the absorption features of CO_2, in a particular part of the EMS, to quantify the CO_2 emission from coalfires (van der Meer *et al*., 2004; Gangopadhyay *et al*., 2005b).

2.5 Conclusions

Coalfires are a widespread problem in most coal-producing countries. Remote sensing can play a significant role in the detection and monitoring coalfires, which may prevent huge economic losses and environmental disasters. In developing countries, such as China and India, coal is the most available and economic energy source. To ensure the proper use of this prime and nonrenewable energy resource, better planning and management is required, with a special emphasis on environmental rehabilitation for a sustainable development. Although

methods for coalfire detection and monitoring that are based on remote sensing are well established, some constraints, such as pixel integrated temperature (with respect to spatial resolution) and acquisition time need to be considered much more cautiously. Most of the research on coalfires has been concerned with detection and monitoring; the GHGs that are emitted from coalfires need to be considered more seriously because they have a significant, adverse impact on global climate. To reduce the steadily increasing GHGs in the atmosphere, emissions that are related to coalfires should be studied more effectively. The countries that are affected most by coalfires (e.g., the United States, China, and India) are concerned about their impact on the environment. However, in most cases, the efforts to restrain these fires are limited if they do not have an immediate economic impact.

Chapter 3

Coalmining, coalfire and environment*

3.1 Introduction

Minerals constitute the backbone of the economic growth of any nation, and coal is one of the easily accessible minerals that are used as a primary energy resource in most parts of the world. Total recoverable reserves of coal around the world are estimated at 1,083 billion tonnes, which is enough to last about 210 years at current consumption levels. Although coal deposits are distributed widely, 60% of the world's recoverable reserves are located in three countries: the United States (25%), the former Soviet Union (23%), and China (12%). Australia, India, Germany, and South Africa account for an additional 29% (Goddard Space Flight Center, 2006). One of the most primitive uses of coal by humans (~75,000 years ago) was found in France (Théry *et al*., 1996).

Mining promotes the economic growth in many ways. In developing countries, mining often does not require huge economic investment to extract minerals from smaller sized mines, but if they are large in size,

*This chapter is based on the following article: Gangopadhyay, P.K., van der Meer, F., Dijk, P.M. and Saha, K. (2007) Coalmining, coalfire and environment in India and China. International Journal of Environmental Studies (in review).

with a greater contribution to economy they have a larger footprint on the local and regional environment. A clustering of smaller mines in an area may also lead to significant environmental consequences. Mining being a concentrated activity tends to draw attention to its physical imprint on land. Moreover, there is a resource dimension to mineral extraction. Minerals are to be treated as a 'fund resource' in environmental sustainability and any future developmental plans are affected by the care with which they are extracted.

Mining has impacts on both physical and human environments at different scales. It is an extractive industry that creates pits and scars, and leaves the land degraded in the process of wining natural resources from the land. As well as people in the mining areas are influenced severely in respect of social and cultural aspects. Mining areas, especially in developing countries, where environment comes after resource, return enormous landuse/landcover change, loss of vegetation cover, soil degradation, change of drainage pattern and relief, subsidence, and loss of flora and fauna. Coal mining in deep underground involves a higher safety risk than coal mined in opencast pits. However, modern coalmines have rigorous safety procedures, health and safety standards and worker education and training, which have led to significant improvements in safety levels in both underground and opencast mining. However, there are still problems within the industry.

In India, coal is the prime source of energy. With a huge input in energy sector, coalmines promote several direct and indirect environmental problems. Most of these problems are directly related with mining operations and related consequences, including mining accidents. Nevertheless, Indian coalmining operations have become much more eco-friendly after nationalization, but there are still several other issues that need to be dealt with more delicately.

Coal is also the main energy resource in China (about 67%). Several environmental problems are frequent in Chinese coalmines, additionally safety in coal mining in China is a critical issue, as the number of fatalities is unacceptably high. By closing unauthorized mines and modernizing operations, Chinese authorities are trying to improve the situation and are promoting the best practice (World Coal Institute, 2007).

The present article describes the main coal mining related environmental issues, first in a coal mining region in eastern India (Raniganj coalbelt), then gives a brief discussion on Chinese coalmining environment.

3.2 Indian scenario: a case study

3.2.1 Study area

The Raniganj coalbelt (RCB) is located in eastern India, and covers a total area of nearly 1,260 km^2 (Fig. 4.7). The area is bounded by 23°28′ and 23°53′ north latitudes, and 86°48′ and 87°26′ east longitudes. Eastern Coalfield Limited (ECL), a state owned subsidiary manages and administrates this mining area. Open-cast and pit both method are being used to extract coal, although an open-cast method is much popular as it is less risky and yields higher profits.

The total economic coal reserve of the RCB is estimated at 24 billion tonnes of non-coking (high moisture, high volatile, high ash), coal and 1.02 billion tonnes of coking (low moisture, medium to high volatile, low ash) coal (Sarkar and Sarkar, 1995). The region now contributes about 20% of total Indian coal output, and is considered to be the second largest in the country. The total coal bearing area of the RCB falling within the eastern Indian state of West Bengal is about 927 km^2. The average thickness of the coal in most of the formations is over 1.2 m, occurring at low depths varying from the surface to 300m (GSI, 2004). At present, there are 109 collieries operating in the region of which 92 are underground and 17 are open cast, producing about 18 million tonnes of coal annually and employing about 174 thousand people (ECL, 2004).

3.2.2 Environmental impact of coalmining and coalfire

Before coal was discovered by colonial administrators in Raniganj in the late 18th century, this area was a forested district known as *Jungle Mahal* or forest state (Paterson, 1910), inhabited by indigenous or tribal people. By the middle of the nineteenth century, at the peak of British rule, mining had begun in full earnest. By that time the environment of the region had undergone so much change that the region was already ‘practically treeless’ (Hunter, 1868, reprinted 1973).

The development of coal mining in colonial period was initially slow. Few factors in the last half of the nineteenth century provided major stimuli for growth. They are: the abolition of East India Company’s

trading monopoly in 1813 which virtually stopped the import of British coal under European supervision; and the introduction of railways to facilitate coal transport to the local market (Rothurmund and Wadhwa, 1978). With the increase of mining operations, fires have always been a major source of accidents and risk in Indian collieries. Early reports of explosions that killed many people are recorded in the Directorate General of Mines Safety records (GOI, 1979). Another report published by the National Council for Safety in Mines (1981) also notes 'fires' among the various causes of early mine disasters in India. The main causes of subsurface coalfires in recent years, are quite different from the spontaneous heating and combustion, and involve long-term human involvement (e.g. unauthorized mining) and related consequences (Lahiri-Dutt, 1999).

After India's independence, the collieries were nationalized in several phases between 1971 and 1973 (Ghosh, 1990), and were brought under the umbrella organization Coal India Limited (CIL). Since then, the population of the region has increased manifold, colliery towns have mushroomed all over and existing towns have given rise to an almost continuous urban sprawl. In RCB, even underground mining has changed the surface landuse through transport linkages, warehouses, subsided areas and dumping grounds for tailings and removed overburden. The vast cultivated tracts have become interspersed with abundant quarry depressions, large heaps of ash and soils, overburdens, minehead gears and the usual characteristic components of the working collieries. Coal mining in this area has resulted in extensive environment degradation and has changed the rural landscape into an extensive urban built up area. On the eve of nationalization of coal industries in 1971, there were only 3 mining towns; in the last census (2001) more than 41 towns have emerged as having their economies based entirely on mining activity (Lahiri-Dutt, 2001). The next few paragraphs discuss the mining related environmental problems in RCB.

3.2.3 Physical impact

Physical impacts of coalmining in RCB can be divided into the following categories:

3.2.3.1 Land subsidence and land degradation

Due to unplanned and irresponsible mining during British rule, many of the abandoned mining pits are not properly stowed with sand and water. With time the surface layers over the void coal seams will not be able to hold the pressure and will collapse. In RCB many places are declared *unsafe* by Director General of Mines Safety. The total volume of the known voids, about 26.82 million m^3, is stretching over nearly 50 km^2 of land. The estimated damages from subsidence in terms of surface land affected are nearly 41 km^2 (Saha, 2004). Other than subsidence, dereliction of land is quite evident in RCB due to abandoned and active surface and underground mines (Fig. 3.1). Of a total area of 55.5 km^2 derelict land, about 20 km^2 is occupied by the abandoned quarries and associated spoil dumps while about 10.5 km^2 is scarred by open cast mining (CMPDIL, 1992).

Fig. 3.1: Coalmine refuse land, RCB.

3.2.3.2 Changes in drainage pattern and local water table

Several minor drainage channels have been diverted from their original courses in order to facilitate the extraction of coal by the open cast method. In some cases, the overburden dumps of the open cast collieries extend almost up to the channels of the drainage lines (Fig.

Fig. 3.2: Diversion of small streams due to overburden dumps of open cast mining.

3.2). Large point bars were noted within the channels of almost all the minor streams due to the accumulation of spoil material drained out into them. Extensive use of subsurface water in mining industry is one of the main destabilizing factors for the local water table. It is proved from time series data that the average depth of the groundwater level has lowered compared to last decade (CMPDIL, 1992).

3.2.3.3 Changes in landuse/landcover

As discussed earlier, once covered with dense deciduous forest, RCB converted into a mixed mining-industrial zone with several mushroomed small mining towns. Mine refuse land, overburden and spoil dump, scars related to opencast mining are frequently visible in this region. Several deforested areas have turned into agriculture and pasture land.

3.2.3.4 Coalfires

The main cause of the coalfires in most coal bearing tracts is spontaneous combustion of coal and unauthorized human activities. Abandoned mines and mine refuse dumps are consequently extremely prone to fires, which can spread to the adjoining working mines.

The extraction of coal from under the ground without completely filling the empty spaces or goafs has caused widespread subsidence through which subsurface coal seams get the air supply and spontaneous combustion starts. Such fires and their consequent underground voids lead to the occurrence of large-scale subsidence or isolated ground collapse, and the wastage of valuable resources of coal in mining regions. Thus, there is a close nexus among phenomena of fire-void-subsidence (Fig. 3.3). The breathing of oxygen into the coal seam may be triggered in many ways but in the RCB, it mostly occurs through one or another factor as described in this nexus.

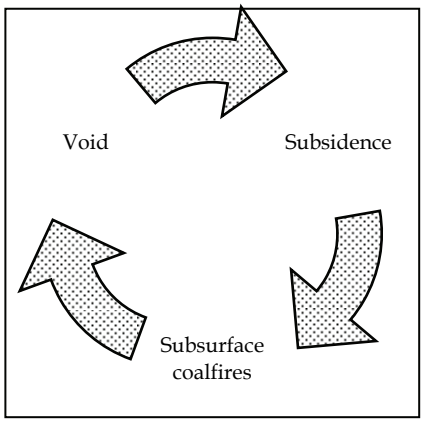

Fig. 3.3: The Void-Subsidence-Coalfire Nexus.

3.2.4 Socio-economic impact

The greatest impact on the social fabric of the region was caused by mass migrations of labour in the past (RoyChaudhuri, 1996), and urbanization in the present (Lahiri-Dutt, 2001). As colliery owners, often through recruiting organizations on contract basis imported upcountry labour, the local tribal workers withdrew from the collieries. However, the post-nationalization mining growth has been characteristic of a stupendous expansion of the urban sector of the economy with all associated features such as decay of agriculture and narrowing of survival bases at the local level.

3.3 Chinese scenario: a brief discussion

China accounts for 12% of the world's total recoverable reserves of coal. In 2002, the total coal production in China was 1.4 billion tonnes, and it is currently ranked as the highest in the world, accounting for about 29 percent of total world production. However, China's coal industry has not attained the same level of development as many of the main coal producing countries in the world. China is the second largest energy consumer in the world and most of its energy is produced from coal (about 67%) in 2002 (Table 3.1). This dominance of coal is not expected to fall significantly even as China's energy demand grows. The Development Research Center of the State Council estimates that coal will account for 66 percent of primary energy consumption in 2010 (Worldbank, 2004). While China's coal resources are deemed sufficient for its needs in the coming two decades, the environmental cost of coal use is already beginning to take its toll, particularly through CO_x, SO_x, and NO_x emissions which are the leading causes of acid rain. In 2002, about 34 percent (6.6 million tonnes) of China's SO_2 emissions were released from power

Fig. 3.4: A small-scale mine in northern China (operated by local village government).

plants (Worldbank, 2004). Apart from power industry, coalfires are significantly responsible for emission of CO_x and SO_x, which is one the main environmental problems related to coalmining.

Table 3.1: China's Primary Energy Consumption (1980–2000).

	Total Consumption (in mil. tons)	Percentage				
		Coal	Oil	Natural Gas	Hydro Power	Nuclear Power
1980	602.8	72.2	20.7	3.1	4.0	
1985	766.8	75.8	17.1	2.2	4.9	
1990	987.0	76.2	16.6	2.1	5.1	
1995	1,311.8	74.6	17.5	1.8	5.7	0.4
1996	1,389.5	74.7	18.0	1.8	5.1	0.4
1997	1,381.7	71.5	20.4	1.7	5.8	0.4
1998	1,322.1	69.6	21.5	2.2	6.3	0.4
1999	1,301.2	68.0	23.2	2.2	6.2	0.4
2000	1,280.0	67.0	23.6	2.5	6.4	0.5

Source: ESMAP, 2004

Table 3.2: Raw Coal Output by Ownership (in million tonnes).

	Total	State - Owned Key Coal Mines	State - Owned Local Coal Mines	Township and Village Coal Mines
1980	620.1	344.4	162.1	113.6
1985	872.3	406.3	182.8	283.2
1990	1,029.9	480.2	205.1	394.6
1995	1,360.7	482.3	213.4	665.0
1996	1,396.7	537.3	222.1	637.3
1997	1,372.8	529.2	225.7	617.9
1998	1,250.0	503.5	212.9	533.6
1999	1,045.0	512.7	213.9	318.4
2000	1,000.0	534.0	199.0	256.0

Source: ESMAP, 2004

Coalmining industry is trailing behind China's power and oil/gas sub-sectors in terms of technology, management and efficiency. Even after tough measures have been taken by the authorities, most of the Chinese coal output is still from small scale mines producing a third of the country's coal (Table 3.2). These small mines (Fig. 3.4) are a major source of the coal mining sector's problems including lack of safety (some two-

thirds of the reported 6,000 coal mining fatalities per year occur in small coal mines) and environmental damage (small mines are the least equipped to address the environmental impacts of coal – only a small fraction of small mines wash their raw coal) (ESMAP, 2004). These small scale mines are often operated by local government (e.g. a town or village authorities).

3.3.1 Main environmental problems of Chinese coalmines

The main coalmining related environmental problems are directly and indirectly related to mining operations. Other than alteration of landscape, coalmines promote mainly air pollution (Fig. 3.5) (by means of increase of dust particle by blasting and transporting, and emission of several noxious gases), water pollution (by releasing untreated water from coal processing plants). Emission of methane from abandoned mines is also a severe problem in Chinese coalmines. Other than these negative impacts related on the environment, coalfire is still one of the biggest problems in Chinese coalmines. High ash content in some coalmines (e.g. Dongqu Mine, Shanxi province) is also a problem for proper waste management. As it was observed in an Indian coalmining area (Raniganj), disturbance in groundwater level is also evident in Chinese coalmines. In the Feicheng Mining Area (Shandong province), 47 km^2 of farmland has become unproductive due to mining related operations, such as: subsidence and disturbance in groundwater level

Fig. 3.5: Air pollution from a coal processing plant, Wuda, north China.

(ESMAP, 2004). The effect of coalmining on local flora and fauna is also obvious in several mining areas in China. In Wuda (Inner Mongolia province), it was observed that most of the area is only covered by occasional small bushes and sparse grass. The present day faunal pattern in Wuda, represents only a small percentage of original fauna of Wuda mining region. The decline in fauna diversity and richness becomes more obvious if one compares the fauna of adjoining non-coal mining area near the Yellow river. The Yellow River with its adjoining agricultural land represents a habitat for common birds found all over northern China (Gangopadhyay, 2003). In the Roqigou coalmining area (Ningxia province), it was observed by Li-ding (1999) that due to environmental pollution, plants growing in this area have been seriously influenced. The chemical composition in grass and poplar tree has shown that some elements in plants have already exceeded the normal range. Based on monitoring results by (Li-ding, 1999), it was concluded that coal fires have much more effect on the content of Cu, F and Zn and little effect on Cd, S and Pb in plants. The content of Cd, S and Pb in vegetation near coal fire areas is usually higher than that in the residential sample areas.

In the Roqigou coalmining area (Ningxia province), occurrence of slides has given rise to land degradation by destroying the original land cover. Particularly during the monsoon season, as spoil dump areas are prone to initiate debris flow, which is very dangerous for local people due to its high velocity and unpredictability. Such debris flows, which occurred in this area in 1992, had claimed 10 lives and resulted in significant building damage (Li-ding, 1999).

Coalfires in China originate at the outcrop of coal in the surface and underground, and have natural and manmade origins. It is estimated that up to 200 million tonnes of high-quality coal are lost every year, mostly in the northern half of China (Rosema *et al.*, 1999). Excluding the consumption of resources, coalfires primarily promote air pollution (by emitting several noxious gases) and frequent subsidence. Recent coalfire studies on China estimate that the country contributes 0.3% (Voigt *et al.*, 2004) of the world's annual output of CO_2 that is caused by fossil fuels. Some previous studies suggested this amount may be as much as 3% of the world's total output (Rosema, 1995), neither of which is a negligible amount. However, the aforementioned estimates are based on indirect methods, such as the total coal burnt in a certain area. Other than

gaseous emissions, coalfires increases the aerosol loading in the local environment. Coaldust and ashes are usually deposited in the nearby agricultural fields, in housing areas and in the water resources by wind and increase the toxic elements in food chain. According to several researchers, the Yellow River shows extremely high levels of pollution which is not only as a result of fertilizer and pesticide usage, but can also be attributed to mining related activities (Chen, 1997; Xie, 2001).

3.3.2 Mining accidents

China produces about 29% of the world's coal, but reported 80 % of the total deaths in coal mine accidents. From January 2001 to October 2004, there were 188 coal mining accidents and an average there were 10 deaths in every case. In 2003, the average coal miner in China produces 321 tons of coal a year; this is only 2.2 % of that in the United States and 8.1 percent of that in South Africa. However, the death rate for production of every 100 tonnes of coal is 100 times higher than that of the United States and 30 times higher than that of South Africa. (Zhao and Jing, 2004).

Most of these accidents occur in small scale town/village administrated mines that are very poorly equipped, and have poor safety measures (Fig. 4), as observed during a fieldwork campaign in 2002. Although the Chinese government has taken several strict steps in order to improve the situation, including the closures of these less equipped mines, China still lags far behind the developed countries in terms of coal mining safety.

3.4 Conclusions

Nevertheless, in most developing countries there is hardly any choice other than cheap and dirty energy resource like coal. However, a few measures can minimize the coal mining related environmental hazards, as discussed below:

- Limiting the number of mining operations in certain area at any given time.
- Voids of subsurface mines should be well stowed by sand and water in order to restore the stability.
- Open cast mines can be filled with spoil and mine refuse materials and afforested to regain the natural environment.

- Industrial requirements of water as far as possible should be met from pumped mine water itself.
- Dumping of mine waste should be avoided nearby natural water bodies.
- Coalfires can be controlled by dousing with water and sealant, or flooding open cut mines. In case of subsurface coalfires, stuffing overburden material in cracks or using other sealing materials could be useful.
- Evacuation of entire villages and townships in extreme cases for human security. Also, authorities should be discouraged to settle in near mining and other related industrial sites, and any planned labour colonies should be developed on 'non-coal areas' with general amenities.
- Provide adequate safety training to mining staffs and take proper safety measures to avoid accidents for best practice.

Chapter 4

Satellite derived emissivity and coalfire detection*

4.1 Introduction

As discussed earlier, satellite remote sensing is established as a significant tool in the field of coalfire detection and monitoring, although few constraints like direct comparison between satellite derived temperature and field measurements have been overcome to an extent. In general, coalfires are a very local phenomenon and in many cases they are not large enough to saturate a whole pixel in order to appear as an anomaly in comparison to the background. The aggregated temperature of a pixel depends on the location, spread, surface type and temperature of the fire/crack and its surrounding. An ASTER/TM pixel is big enough (90/120m) to accommodate few cracks with active fire, local rocks and (sometimes) sparse vegetation. These different types of landcover may have different temperature ranges to influence each other

*This chapter is based on the following articles: Gangopadhyay, P.K., Maathuis, B. and van Dijk P. (2005) ASTER Derived Emissivity and Coalfire Related Surface Temperature Anomaly: A Case study in Wuda, North China. *International Journal or Remote Sensing*, 26(24): 5555-5751 and Gangopadhyay, P.K., Lahiri-Dutt, K. and Saha, K. (2006) Application of remote sensing to identify coalfires in the Raniganj Coalbelt, India. *International Journal of Applied Earth Observation and Geoinformation*, 8: 188-195.

and finally appear as an anomaly or background with a certain pixel integrated temperature value. Also viewing angle, foot print, field of view (FOV) of sensor, distance from the object and operating range (wavelengths) between two types of sensors (handheld radiant thermometer and satellite) can introduce observation errors that are impossible to overcome.

Nevertheless, it is necessary to mention that most of the remote sensing based coalfire studies are based on a fixed emissivity (0.95 or 0.96) which is contrary to the real representation of the Earth's surface. Before multispectral thermal data (e.g. ASTER) was available it was not possible to obtain temperature and emissivity directly from passive radiometry separately, since the number of unknowns was always larger than the number of measurements (Becker, 1980). However, the knowledge of land surface emissivity is necessary to extract more reliable temperature from (a certain) thermal infrared data. Using a single thermal band it is impossible to get such information from the available methods such as Temperature Emissivity Separation algorithm (TES) (Gillespie *et al*., 1999). The TES method, based on ASTER data, returns a reliable land surface emissivity of an area under investigation (Gangopadhyay, 2003). In the case of single band thermal data a possible option to extract land surface emissivity could be a classified image, in which an emissivity value for each class is assumed. However, without very detailed knowledge of different classes of study area and a realtime (ground) data it will not be very functional (Dash *et al*., 2005). Another functional option could be to extract land surface emissivity from NDVI that has already been described by many researchers (van de Griend and Owe, 1993; Valor and Caselles, 1996; Sobrino and Raissouni, 2000; Sobrino *et al*., 2004). The method proposed obtains the emissivity values from the NDVI considering three different cases:

- NDVI < 0.2: Pixels with NDVI values less than 0.2 are considered as bare soil,
- NDVI > 0.5: In this case, the pixel is considered as mostly vegetated, and
- 0.2 < NDVI < 0.5: In this case, the pixel is composed by a mixture of bare soil and vegetation, and the emissivity can be calculated using the equations described by Valor and Caselles (1996). The detailed methodology is described in section 4.3.2.

This chapter discusses two case studies in northern China and eastern India. In the both cases, satellite derived emissivity (using the TES algorithm and NDVI derived) were used to obtain a better representation of surface temperature. In the first case (northern China) coalfire related anomalies were extracted qualitatively and an attempt was made to relate satellite derived temperature and pixel integrated temperature by taking local ground factors into account. In the second case (eastern India) NDVI was used to derive emissivity of different land surface in order to extract surface kinetic temperature.

4.2 Coalfire detection in northern China

4.2.1 Study area

4.2.1.1 Location

The study area, the Wuda coalmine area (also named Wuda syncline), is located in the Inner Mongolia autonomous region (Fig. 4.1). Physically the area is bounded by the Gobi desert in the north and the west, the Yellow river in the east, and by the Helan Mountain in the south. The extent of the Wuda coalmine area from north to south is 10km and from east to west is 3-5 km, with a total area of 35 sq km. Mining began in the Wuda mining region in 1958, but was subsequently subdivided into three mining zones: Wuhushan, Suhaitu and Huangbaici by the mining authority.

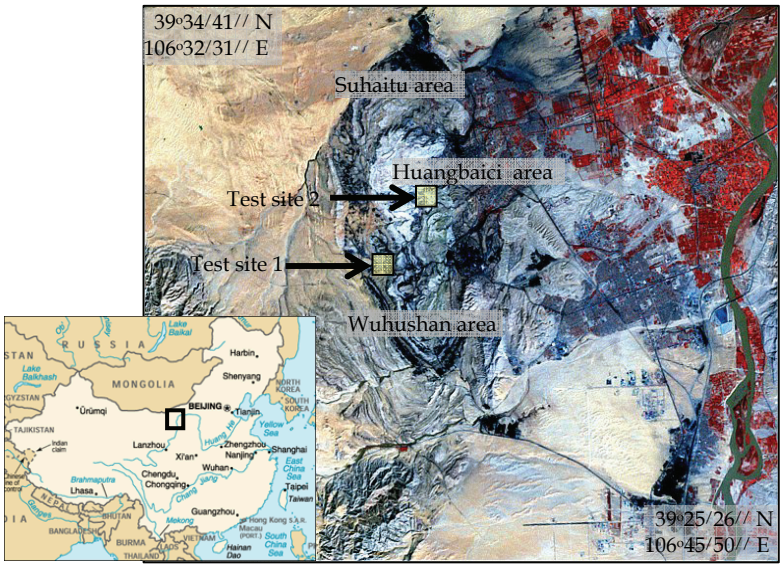

Fig. 4.1: Location of the Wuda coalmine area and test sites.

The first coalfire in Wuda mining region was recorded in 1961 in a small coalmine pit. Before 1989, the coalfires in Wuda were isolated and scattered in different places. These isolated fires gradually connected between 1989 and 1995, and the 'connected fires' have been spreading rapidly since 1995. In 2001, Wuda coalmine authority asked the Beijing Remote Sensing Corporation (BRSC) to investigate the extent of the coalfire areas in the Wuda coalmine area. In 2002, BRSC made a more detailed investigation of the areas affected by the coalfires and concluded that the total area affected by coalfires is 3.07 million m^2 covering 8.8% of the total area of the Wuda syncline (Source: Wuda Mining Authority).

4.2.1.2 Geology and coal

The Wuda coalfield consists of coal-bearing strata of Late Carboniferous and Permian age. Approximately 80% of the coal mined in China comes from Late Carboniferous coal seams (Dai *et al*. 2002). The paleogeography and lithofacies of Late Carboniferous age in northern China can be divided into three belts – the northern belt, the central belt and the southern belt. In the central belt, the sediments are characterized by alternating fine clastics and limestones, suggesting a shifting shoreline zone (Liu, 1990). The Wuda coalfield is located in the central

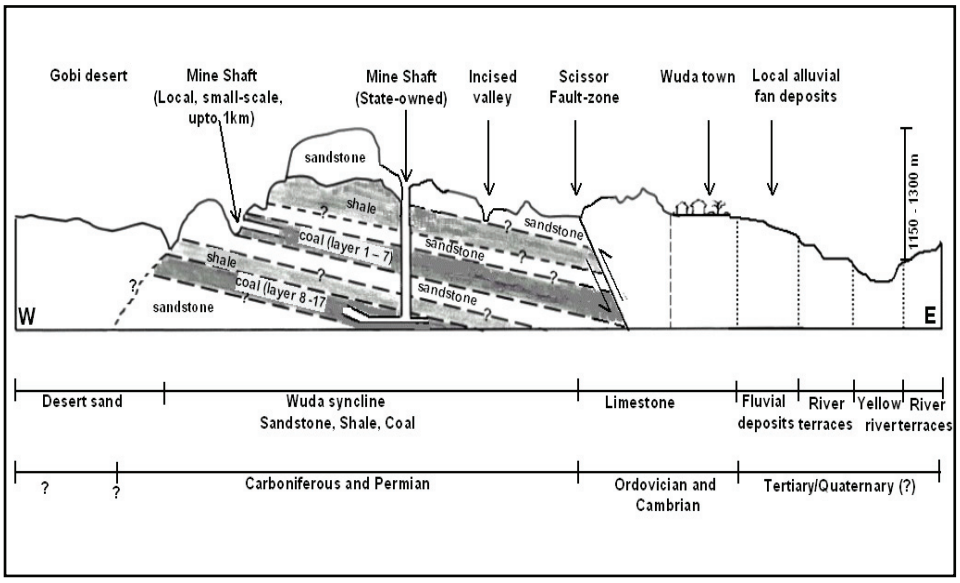

Fig. 4.2: Generalized cross-section (W-E) through the middle of the Wuda syncline (not to scale).

belt. The geological sequence is consisting of Upper Carboniferous and Lower Permian strata, of continental/fluvial origin (Fig. 4.2).

The east side of the ear-shaped syncline is cut by a reverse scissor fault dipping east with dip angle of 34-75°. The displacement of the fault varies from 30 to 600 m from north to south respectively. The fault brings the limestone rocks of Ordovician and Cambrian age east of the syncline in contact with the Carboniferous and Permian strata of the syncline. This coalfield has a reserve of 630 Mt coal – mostly fat coal and cooking coal. The total remaining coal reserve is about 280 Mt, of which about 100 Mt is not accessible due to the coalfires. There are a total of 24 coal seams in the Wuda syncline, of which 17 are mined. Minable coal seams are numbered from top to bottom (1-17). The top of the sequence (Permian) has 7 minable coal layers of low Sulfur (1.6-2.8%) and high ash content. The lower (Carboniferous) layers (8-17) generally have high Sulfur (3.5-5.5%) and low ash content.

4.2.1.3 Test areas

Two test sites were selected and surface temperature data were collected. These test sites are approximately 300m×300m and are nearly equal to nine ASTER pixels and are situated in Wuhushan and Huangbaici coalmining area, and are known as coalfire 7 and 8 respectively by the mining authority (Fig. 4.1). In the middle of these test areas, two trajectories were defined to measure surface temperatures on a realtime basis.

A) Test site I: In coalfire area 7 of Wuhushan coalmining area (Fig 4.1), an area was selected for night time measurements. The area is composed of sedimentary rocks, mostly sandstone (95%) and shale (5%). Due to active subsurface fires the surface is severely collapsed and now has an undulating appearance (due to room-and-pillar mining method). Topsoil in this area is mainly loose colluvial material and is covered with very few scattered small bushes or dry grasses (2-5% of groundcover). Due to the homogeneous surface characteristics, field data collected from this area is ideal for comparison with remote sensing data. In order to record surface temperature during satellite overpass, the test site was divided in two traverses, one is north to south and another is west to east.

B) Test site II: In coalfire area 8 (Fig 4.1), test site 2 was selected. This area has been severely affected by fire, as the surface is cracked or has collapsed due to underground fires. This area is mainly composed of sandstone (70%) and shale (15%) with locally coal waste deposits (10%). A small portion (~5%) situated on the northwest of test site is covered by loose colluvial material mixed with crushed shale and totally bare of vegetation.

4.2.2 Methodology

In the present study, the two levels selected for data collection are satellite and ground or field measurements in order to identify the thermal anomalies related to coalfires.

The aim of surface or ground data collection is to obtain information about geographic features and phenomena through *in situ* (during satellite overpass) measurements to validate processed satellite data. The five major components of ground data collection are:

- temperature,
- geographic position (X,Y,Z),
- attribute (surface properties – cracked/subsidence/exposure),
- spatial relationship (local geological setting) and
- time (satellite overpass time).

From 700 to 737 km above the earth surface, the ASTER instrument acquires data with a swath of 60 km. The repetitive cycle of the ASTER instrument is 16 days. The TIR (thermal infrared) region is covered by five bands, three bands for wavelengths shorter (8.125 to 9.275 µm) than the ozone-absorbing band (9.6 µm) and the other two bands for longer wavelength (10.25 to 11.65µm). The spatial resolution is 90 m, and the spectral resolution is 0.35 µm for bands 10, 11, 12, and 0.7 µm for bands 13 and 14 respectively. ASTER data is suitable to derive emissivity from satellite data because of its multi-band thermal coverage and high radiometric resolution. With a 12 bits signal quantization level, ASTER can detect very small differences in radiance (Gillespie *et al*., 1999). To extract thermal anomalies from ASTER TIR data, the TES algorithm was used (Gillespie *et al.*, 1999).

4.2.2.1 Pre-processing of ASTER data

ATCOR is a commonly used software extension that excludes the atmospheric effects of remote sensing image based on inbuilt atmospheric database. In the ATCOR model, the 16 bit data of ASTER TIR is not acceptable – it needs to be rescaled to 8 bits, which means loss of data precision. Another drawback of this model is that, only band 13 is used in the ATCOR model out of the five thermal bands available (Richter, 2005). So currently, ATCOR is only generating a ground temperature map but not a theoretically possible spectral emissivity map using all ASTER thermal channels. In the present study, a linear relation was drawn up between the radiance recorded by the sensor and the atmospheric transmittance, which is calculated from recorded data (by using a sun photometer) in the field. If the atmospheric transmittance is 90% then only 90% of the emitted energy is being recorded by sensor as radiance. So if the radiance value is increased by 10% then it can compensate for the atmospheric effects. Nevertheless, during validation with ground truth data it was found that the relationship between transmittance measured in visible range and radiance recorded at the sensor does not have the direct relationship that was expected. However, it is known that the interaction of energy with atmosphere in the visible domain is different than in the thermal domain. Nevertheless, the aforementioned method was attempted for experimental purposes only. As stated before, because of unavailability of a suitable atmospheric model (during this study) the raw data was processed without further atmospheric correction and was still found to be very close (>1 K) to the ground measurements during validation. Because of nominal variation in validation, it was decided the data can be further processed without further atmospheric processing.

4.2.2.2 Temperature/Emissivity Separation (TES)

A surface having a temperature more than absolute temperature emits energy, depending on the properties of the surface and is function of the wavelength. Emissivity is an inherent property of surface and is independent of irradiance. Planck's law describes the relationship between the temperature and radiance of a perfect emitter (i.e. a black body). The TES algorithm, developed by the ASTER team, can extract temperature (with an accuracy of $\pm$1.5 K) and emissivity (with an accuracy of $\pm$0.015), compared to field measurements (Gillespie, 1999) using multi-spectral thermal data. There are many TES methods developed by different scientists, basic of the method is described below.

At temperature T, the spectral radiance of a blackbody can be calculated using the Planck function:

$$L_j^{BB} = \frac{C_1}{\lambda_j^5 \pi \left[\exp\left(\frac{C_2}{\lambda_j T} \right) - 1 \right]} \tag{4.1}$$

where, L_j = blackbody radiance, (w m^{-2}) λ_j = wavelength of channel j(m), T = temperature of the blackbody (K), C_1 = first radiation constant (w m^{-2}), C_2 = second radiation constant (mK)

However, as most surface materials do not emit energy like a perfect blackbody, the spectral emissivity (ε_j) of a material refers to the ratio of radiation emitted by a blackbody and the surface. It can be defined as:

$$\varepsilon_j = \frac{L_j}{L_j^{BB}} \tag{4.2}$$

Temperature/Emissivity Separation (TES) algorithm consists of a few modules. It is closely related to the Mean-MMD (Mean Max Difference) method (Matsunaga, 1994), which is based on the Alpha-Derived Emissivity (ADE) technique (Kealy and Gabell, 1990; Hook *et al*., 1992; Kealy and Hook, 1993). Essentially, the TES algorithm uses the Normalized Emissivity Method (NEM) (Gillespie, 1985) to estimate T, from which emissivity ratios are calculated (RATIO algorithm). These β values are the NEM emissivity normalized by their average value.

The input data sets consist of *Land-leaving TIR Radiance* (L) and *sky irradiance* ($S\downarrow$). To subtract the reflected sky irradiance ($S\downarrow$) and estimate surface temperature, the NEM module is used. In this module, radiance R_b is estimated by subtracting reflected sky radiance:

$$R_b = L_b - (1 - \varepsilon_{max})\, S\downarrow_b \tag{4.3}$$

The NEM temperature is taken to be the maximum temperature calculated from R_b for image channels b=10-14.

$$T = \max(T_b); T_b = \frac{C}{\lambda_b}\left(\ln\left(\frac{C_1 \varepsilon_{\max}}{\pi R_b \lambda_b^5} + 1\right)\right)^{-1} \quad ; \quad \varepsilon_b = \frac{R_b}{B_b(T_b)} \tag{4.4}$$

where, C_1 and C_2 are the constants from Planck's Law (eq. 4.1) and value of ε_{max} is 0.96. Once T is known, NEM emissivity can be calculated and used iteratively to re-estimate equation $R_b = L_b - (1 - \varepsilon_{max})\ S_{\downarrow b}$. The relative emissivity, β_b, extracted by ratioing emissivity, as calculated from the NEM T and the atmospherically corrected radiances, in order to obtain the average emissivity as follows:

$$\beta_b = \varepsilon_b\ 5\ (\sum \varepsilon_b)^{-1};\ b = 10\text{-}14 \tag{4.5}$$

The β spectrum is scaled to actual emissivity values, and the surface temperature is recalculated from this new emissivity using the atmospherically corrected radiances. An empirical relationship predicting ε_{min} from MMD is used to convert β_b to ε_b. Its regression is established using laboratory reflectance and field emissivity spectra. The first step in the TES algorithm is to find the spectral contrast:

$$\text{MMD} = \max(\beta_b) - \min(\beta_b);\ b = 10\text{-}14 \tag{4.6}$$

From this, the minimum emissivity used to predict and calculate the TES emissivity is:

$$\varepsilon_{min} = 0.994 - 0.687 \times \text{MMD}^{0.737};\ \varepsilon_b = \beta_b\left(\frac{\varepsilon_{\min}}{\min(\beta_b)}\right);\ \text{b= 10-14} \tag{4.7}$$

Finally, the quantification of surface temperature together with atmospherically corrected radiance R and the TES emissivity spectrum uses the following equation:

$$T = \frac{C_2}{\lambda_b}\left(\ln\left(\frac{C_1 \varepsilon_b}{\pi R_b \lambda_b R} + 1\right)\right)^{-1} \tag{4.8}$$

Where, b is the ASTER band for which emissivity ε_b is maximum (and correction for $S_{\downarrow}$ is minimum).

Reference Channel Method (RCM)
In this method it is assumed that a pixel has a constant emissivity (0.95) value in the higher wavelength region (ASTER band 14, 10.9µm-11.6µm), because in this spectral region, the emissivity differences are less compared to those recorded by other ASTER channels. After knowing the emissivity, *T* can be calculated by

$$T_R = \frac{C_2}{\lambda_R \ln\left[\frac{\varepsilon_R C_1}{L_R \lambda_R^5 \pi} + 1\right]} \tag{4.9}$$

where the subscript *R* refers to the reference channel. This *T* is used together with eq. 4.1 and 4.3 to estimate emissivity values for the other channels.

Emissivity Normalization Method (NEM)
For the present method, a constant emissivity value (0.96) was used for each channel in order to calculate the temperature, where the highest temperature was designated as the temperature of the pixel. Then the emissivity was recalculated for other channels with the defined temperature.

4.2.2.3 Field based methods

To estimate the temperature of different surfaces and crack/fires, a handheld Raytek radiant thermometer was used. This instrument operates in a wide region of temperature (241 to 760 K), spectral coverage (8 to 14 µm) and the emissivity can be defined with a precision of 0.01. A laser pointer makes it easy to point at a particular object from a distance. Most measurements were recorded along the predefined trajectories (see the study area) from a typical distance of ~1 m except for some inaccessible areas. In those cases the measurements were recoded from a distance of ~5m. With an accuracy of $\pm$1 K it was the best available instrument during fieldwork. Also a contact thermometer (precision $\pm$1 K) was used to measure kinetic temperatures in the Yellow river and some other relevant locations e.g. in topsoil and coal (waste) dumps etc.

4.2.3 Results and discussions

The temperature maps extracted from ASTER nighttime data (21.09.02) show a good contrast between anomaly and background. In order to avoid any kind of influence from the surrounding pixels, the raw images were first processed using NEM and RCM approaches and a total of ten temperature maps were extracted. After processing, the images were geo-rectified and resampled using the 'nearest neighbour method' in order to minimize the influence from the surrounding pixels. The sigma value (Σ) was kept less than one pixel to accurately correlate the ground observations with those of the satellite images. The RCM BAND 14 was excluded because of its constant emissivity (0.95). Although one of the main aims of the present study was to extract the anomalous pixels in order to identify the coalfires qualitatively, satellite derived emissivity values were also used to derive kinetic temperature to validate the

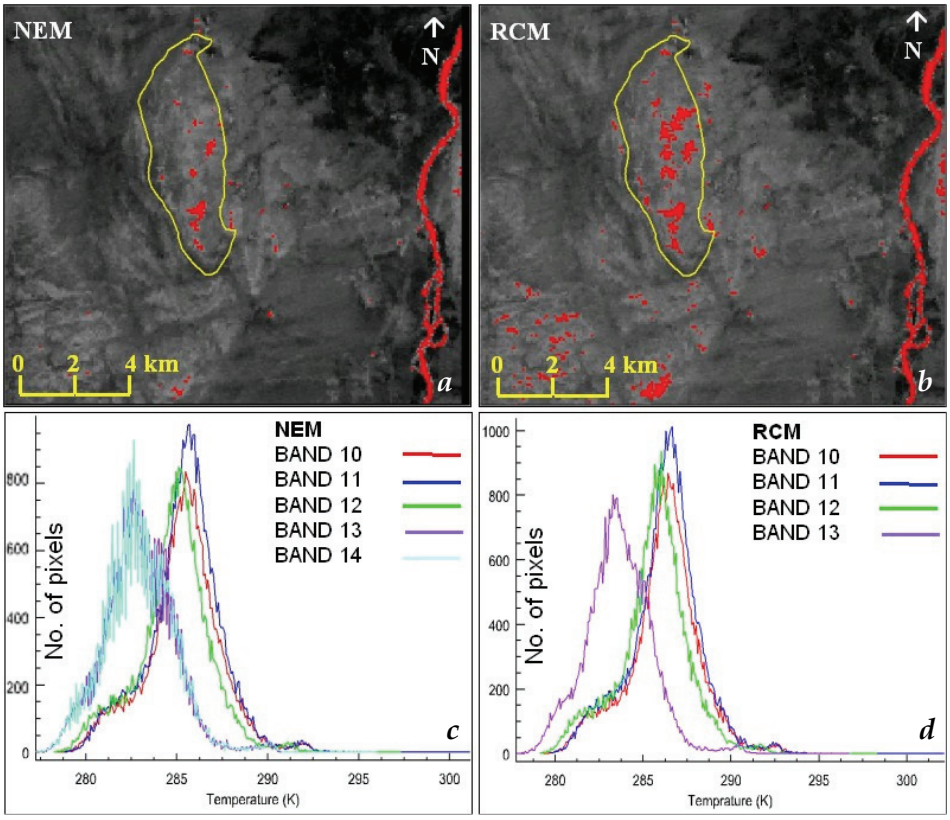

Fig. 4.3: Temperature anomaly extraction from ASTER data by NEM and RCM method and their graphical representation.

processed images before threshold determination. In order to determine the threshold value, several realtime temperature measurements of different surface types were collected, and later the average of these measurements was taken as maximum background temperature (286.83 K) to delineate coalfire related anomalous pixels.

Table 4.1: Temperatures comparison of different bands of NEM & RCM.

BAND	Min T (K)	Max T (K)	Mean	STD
NEM Band 10	278.347137	297.710083	285.366524	2.08
NEM Band 11	278.773682	301.115875	285.456218	2.05
NEM Band 12	278.229950	297.294647	284.857645	2.04
NEM Band 13	277.240021	295.972809	282.976196	1.91
NEM Band 14	277.259491	296.003845	282.976230	1.93
NEM AVG.	278.027252	297. 619446	284.326563	1.98
RCM Band 10	279.317596	298.753052	286.207279	2.05
RCM Band 11	279.709900	302.124878	286.260557	2.02
RCM Band 12	279.126404	298.250702	285.627791	2.02
RCM Band 13	277.770477	296.791718	283.633701	1.86
RCM AVG.	279.024384	298.980103	285.432332	1.97
AVG.	278.502258	298.224182	284.818016	1.97

Fig. 4.3a and 4.3b show the average temperature maps which are derived by NEM and RCM respectively, where the Yellow line shows the border of the mining area. Because of the presence of some high thermal inertia rocks like quartzite, basalt and industrial activities, some pixels appear as a false anomaly in the south and southwestern part of the image. The Yellow river also appears with high temperature because water has a high heat capacity (i.e. relatively warm during the night).

It is evident from Fig. 4.3a and 4.3b that the anomalous pixels are different for the two methods. This can be explained by the different ranges of emissivity obtained for the different methods. Because emissivity differs less in longer wavelength, and the emissivity range is comparatively high (0.93-0.96) so temperature range is comparatively low for band 13 and 14 (Fig. 4.3c and 4.3d). The temperature range of each band of NEM and RCM is shown in the Table 4.1.

The average temperatures derived from NEM (5 bands) and RCM (4 bands) are shown in Fig. 4.4a. Temperature derived using NEM, RCM methods and their average were compared with field data and the NEM

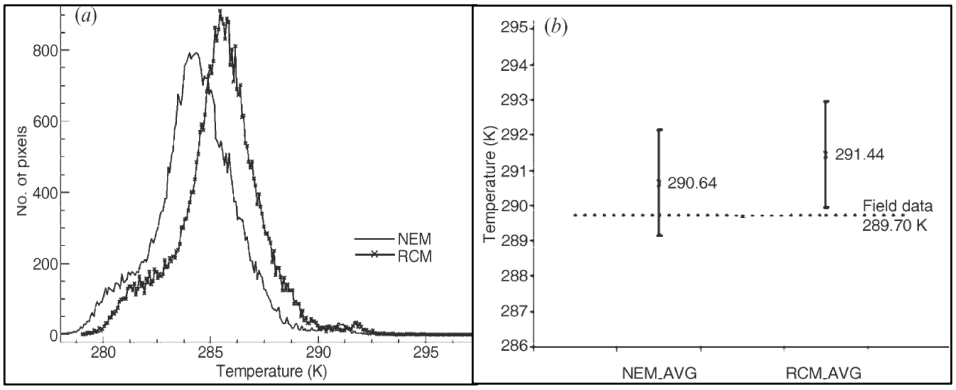

Fig. 4.4: (a) Extracted temperature comparison (b) A graphical comparison of satellite derived surface temperature with ground truth.

temperatures have a close correlation with field data. Fig. 4b presents the comparison of different results with ground truth point measurements of the Yellow river for validation and further processing. As large water bodies are more homogeneous and more stable (in temperature) than land surface, it was for this reason that the Yellow river was chosen for the validation purpose. Here NEM_AVG, RCM_AVG, represents, average NEM temperature and average RCM temperature respectively. It is clear from Fig. 4.4b that average NEM has the closest relationship with the field measurements, and for further processing, the NEM average temperature was used.

The satellite derived temperature maps of ASTER (Fig. 4.5a) were compared with a coalfire map created from ground truth by the Wuda Mining Authority (WMA). The reasons behind some discrepancies between WMA provided coalfire map and satellite derived coalfire map are, firstly the map is one year old and secondly some coalfires are already extinguished, which was experienced in the field study. Also as the WMA map was prepared by random field observations and local geological map that may be somehow overestimated. However, the WMA coalfire map was used only to obtain a general idea of spread of fire and exclude the false anomalies related to industry like coke processing plant and thermal power plant, urban area etc.

By comparing the two sources of data (field observations and remote sensing image), the locations of the fires can be identified. In Fig. 5b the comparison between field observations and satellite derived anomalies

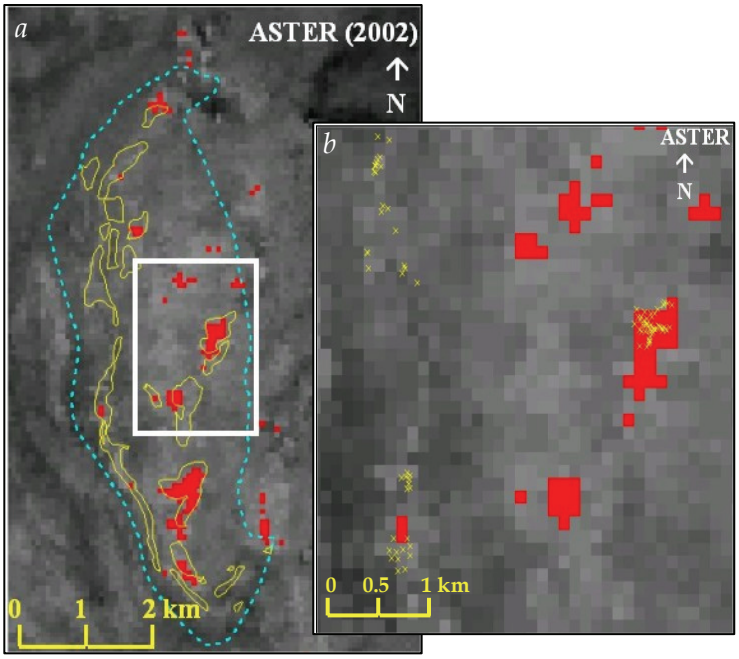

Fig. 4.5: (a) A comparison between satellite-derived surface temperature and ground data (the cyan lines represent the mining area and yellow polygons represent the fire-affected areas demarked by WMA). (b) A close up view of (a) (the yellow cross represents the location of anomalies observed on the ground).

are shown in larger scale. These figures show a good correlation between remote sensing images extracted surface temperature anomalies and field observations. From Fig. 4.5b it can be concluded that, if the area affected by coalfires is not big enough to influence the whole pixel, it will not appear as an anomaly, which is evident in the north-western part of the image.

4.2.4 The relation between crack and satellite derived temperature

As described before, viewing angle, distance from the object, foot print, field of view (FOV) and operating range (wavelengths) of two types of sensors (satellite and handheld) will introduce errors during comparison, however, the following method was adopted to assess its suitability.

During field survey, sample points were taken as well very randomly distributed and the temperature values are unevenly distributed (Fig.

4.6). The width of cracks, depth of the fires, the conductivity and thermal inertia of the local rock type are the prime factors of this phenomenon, which was observed during the field survey.

Comparing the locations of cracks in the pixel and area covered by the cracks, these were considered to be the main factors to determine the pixel integrated temperature. A relationship between crack temperatures (with were measured with a distance of ~1 m) and satellite derived temperature is quite complicated because of differences in the scaling factor, viewing angle and atmospheric attenuation. Therefore, a simple method was attempted to establish a relationship between ground truth and satellite acquired temperatures.

To find the contribution to the pixel integrated temperature due to crack temperature, a simple weighting factor was used. Every pixel under investigation was divided into 16 sub pixels, and then if the crack location was in the middle of the pixel, the weighting factor was 1. However, if it was in the next category, a weighting factor of 0.5 and then 0.25 was assigned.

The average temperature of pixel that can be expected as pixel integrated temperature was calculated using crack coverage, location of

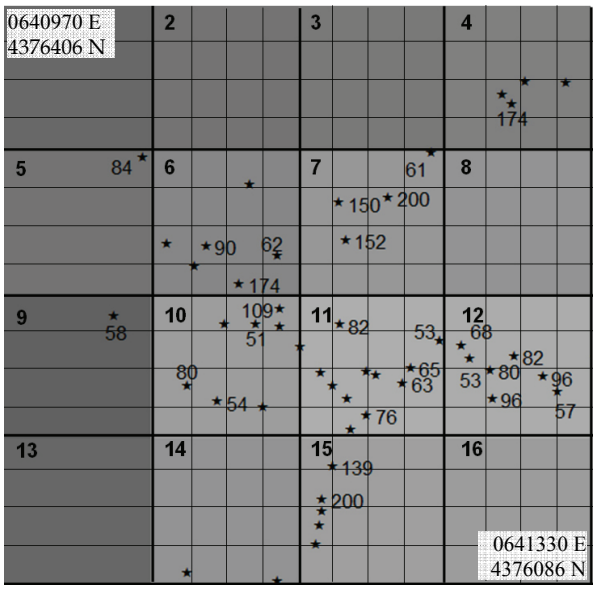

Fig. 4.6: A comparison between satellite-derived surface temperature and ground data.

crack and weight factor. Then a comparison was made between calculated pixel integrated temperature (using ground truth) and satellite derived temperature (Table 4.2). The following findings were observed.

- Pixels with very low crack coverage and a medium or low temperature (but more than the background) can appear without any thermal anomaly in a satellite image.
- Pixels with low crack coverage and medium temperature can be close to satellite derived temperature.
- Pixels with medium crack coverage and high or very high temperatures can be more than satellite derived temperature.

A paired t-test was performed to determine if there was a significant difference between the two observations (satellite and surface based, see Table 4.2). The result t=1.9 (p-value=0.096) indicates that there is indeed a certain correlation between satellite derived and field observed temperature.

Table 4.2: Comparison of satellite derived and crack temperatures of certain pixels under consideration.

Pixel no.	Crack cover (approx. m2)	% of pixel Cover by crack	Field temp (K)	Weighting factor in relation to location	Contributory temp to pixel (K)	Avg. temp Average temp. of cracks (K)	Probable temp contribution in relation to coverage (K)	Probable temp of pixel with crack temp contribution (K)	Satellite derived Temp(K)	Difference (K)
4	506.25	6.25	447	0.5	294	360	277.69	291.52	288.2	3.32
5	506.25	6.25	357	0.25	318	294	273.56	287.39	287.38	0.01
6	1518.75	18.75	363	0.5	288.5	307.67	277.25	291.08	288.71	2.37
			335	0.25	316.5					
			447	0.25	288.25					
7	2025	25	334	0.25	348	339.56	286.64	300.47	290	10.47
			423	0.5	373					
			473	0.5	349					
			425	0.5	287.5					
9	506.25	6.25	331	0.25	285.75	287.5	273.16	286.99	286.08	0.91
10	2025	25	324	0.25	300.25	294.75	275.44	289.27	290.42	-1.15
			382	0.25	293					
			353	0.25	300					
			327	0.5	293.5					
11	2531.25	31.25	355	0.25	286.25	293.1	275.53	289.36	291.65	-2.29
			326	0.25	289.25					
			338	0.25	304.5					
			336	0.5	292					
			349	0.25	290					
12	2531.25	31.25	341	0.25	286.25	306.68	279.77	293.6	291.56	2.04
			326	0.25	314					
			355	0.5	313					
			353	0.5	321					
			369	0.5	321					
			369	0.5	301.5					
			330	0.5	342.5					
15	1518.75	18.75	412	0.5	373	350.33	285.25	299.08	291.56	7.52
			473	0.5	294					

4.3 Coalfire detection in eastern India

4.3.1 Study Area

4.3.1.1 Location

The Raniganj coalbelt (Fig. 4.7) comprises a total area of nearly 1,260 square kms, and is located about 250 kms northwest of Kolkata, the capital of West Bengal, an eastern state of India. The area is bounded by 23° 33' and 23° 53'N latitude and 86° 37' and 87° 23'E longitude. A major part of the Raniganj coalfield (according to the Coal India Limited definition) falls within Burdwan district (of West Bengal), which we have identified as our study area.

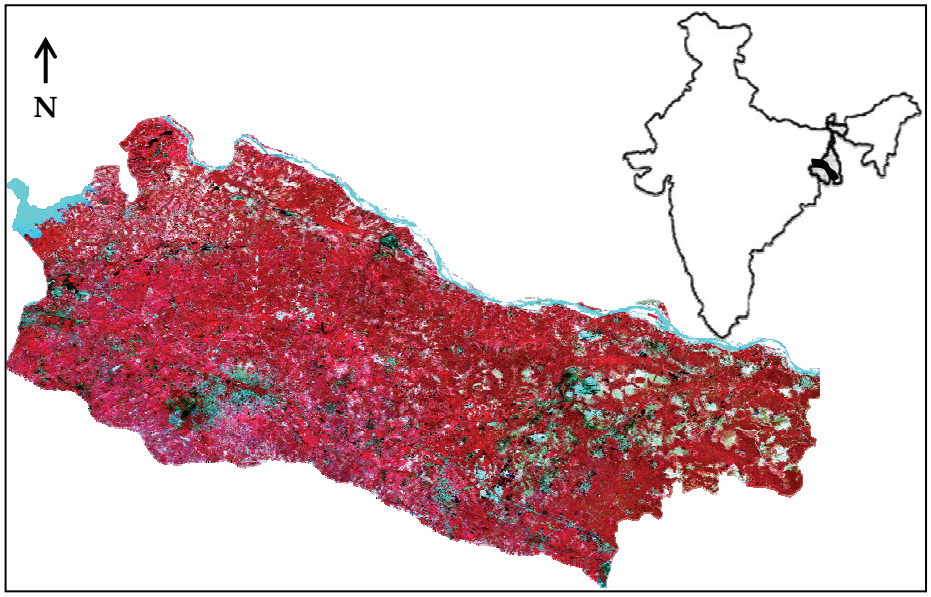

Fig. 4.7: Location of Raniganj coalmining area, India.

4.3.1.2 Geology

The sedimentary rock formations which comprise Raniganj coalbelt – excluding the recent and subrecent alluvial and lateritic deposits – all belong to Gondwana system which extended over a considerable portion of the southern hemisphere (Gee, 1932). Permocarboniferous rock formations of Talcher, Barakar, Barren measures, Raniganj and Panchet series are exposed in many places (Fig. 4.8). The southern boundary is represented by a well defined fault of an immense down throw to the north (Blanford, 1861). According to a recent Geological

Survey of India (GSI) report, the Raniganj coalbelt has the second largest resource of coal (25 billion tonnes) in India (GSI, 2004).

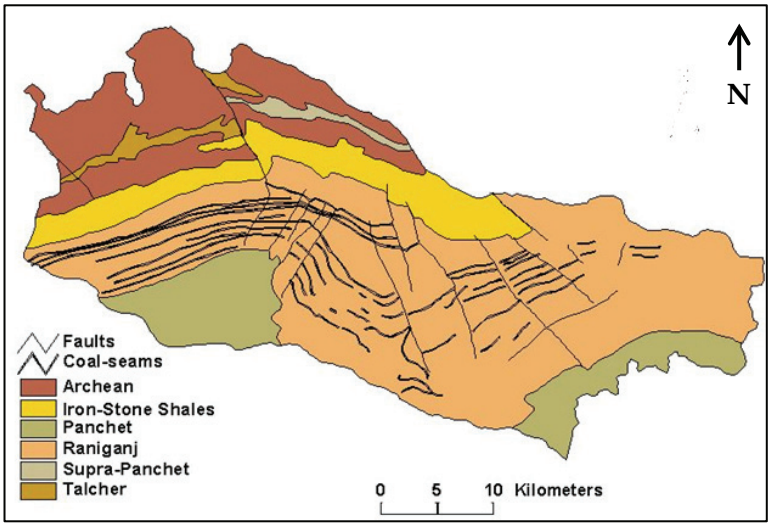

Fig. 4.8: Geological settings of Raniganj coal coalmining area.

4.3.2. Methodology

Landsat 5 thematic mapper (TM) bands 3, 4 and 6 acquired on 30th April, 1997 (daytime) were used for the study. In order to identify the thermal anomalies related to coalfires, satellite and ground (or field) measurements are used. The aim of surface or ground data collection is to obtain information about geographic features and phenomena through *in situ* measurements to validate processed satellite data. The five major components of ground data collection are: (a) temperature, (b) geographical position, (c) attribute or surface properties, (d) spatial relationship and (e) satellite overpass time.

4.3.2.1 Pre-processing of Landsat TM data

To reduce the atmospheric effect of Landsat TM3 and TM4 data ATCOR2 (Richter, 2005) was used. As the area is characterized by a very gently undulating topography with average height of the ground level varying between 73m and 120m, it was expected that solar heating did not have much of a role to play in producing false anomalies. However, these atmospherically corrected images were used for further processing.

4.3.2.2 Processing of TM data

The atmospherically corrected red and infrared bands were later used for NDVI calculation to extract surface emissivity. Thermal infrared band or TM6 of Landsat was used to extract brightness temperature by using the method described below.

The digital values of thermal band were converted to spectral radiance using the following equation (Markham and Baker 1986):

$$L_\lambda = L_{\min(\lambda)} + \frac{L_{\max(\lambda)} - L_{\min(\lambda)}}{Q_{cal\max}} Q_{cal} \tag{4.10}$$

where, L_λ = Spectral radiance, $L_{\min(\lambda)}$ = Minimum detected spectral radiance for the scene (0.1238 mw cm^{-2} sr^{-1} μm^{-1}), $L_{\max(\lambda)}$ = Maximum detected spectral radiance for the scene (1.56 mw cm^{-2} sr^{-1} μm^{-1}), Q_{cal} = The grey level for the analysed pixel, $Q_{calmax(\lambda)}$ = The maximum grey level.

Once the spectral radiance (L_λ) for TM Band 6 is computed, it is possible to calculate radiant temperature directly by the following equation:

$$T_R = \frac{K_2}{\ln\left(\frac{K_1}{L_\lambda} + 1\right)} \tag{4.11}$$

where, T_R= Radiant temperature (K), L_λ= Spectral radiance (mw cm^{-2} sr^{-1} μm^{-1}). K_1= Calibration constant (60.776 mw cm^{-2} sr^{-1} μm^{-1}), K_2= Calibration constant (1260.56 K)

To enhance the vegetation characteristics over an area under consideration, the vegetation index is widely used in many applications. One of the most common vegetation indices is NDVI, which can be calculated as

$$NDVI = \frac{(\rho_2 - \rho_1)}{(\rho_2 + \rho_1)} \tag{4.12}$$

where, ρ_2 = spectral reflectance measured in NIR band (TM 4), ρ_1 = spectral reflectance measured in red band (TM 3).

In order to calculate the emissivity it is necessary to calculate the NDVI of a mixed pixel. Considering a mixed pixel of TM6 in which vegetation has occupied an area P_V and soil occupied (1 - P_V) (Fig. 4.9), the NDVI becomes (Valor and Caselles, 1996):

$$i = i_v P_v + i_g (1 - P_v) \qquad (4.13)$$

where, i - is the NDVI value of the mixed pixel, and i_v and i_g are the values of the vegetation and ground.

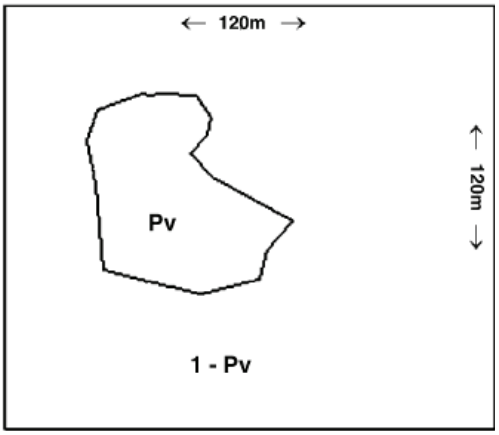

Fig. 4.9: A mixed pixel of TM6 in which vegetation has occupied an area P_v and soil occupied (1 _ P_v).

The value of i (NDVI of a mixed pixel) is calculated through the satellite data using the following equation:

$$P_v = \frac{\left(1 - \frac{i}{i_g}\right)}{\left(1 - \frac{i}{i_g}\right) - \kappa\left(1 - \frac{i}{i_v}\right)} \qquad (4.14)$$

where, i = NDVI value of mixed pixel, i_V = is the NDVI value of pure vegetation, i_g = is the NDVI value of pure soil and

$$\kappa = \frac{\rho_{2v} - \rho_{1v}}{\rho_{2g} - \rho_{1g}} \qquad (4.15)$$

where, ρ_{1v} and ρ_{2v} are reflectance values of vegetation in red and NIR, ρ_{1g} and ρ_{2g} are reflectance values of soil in red and NIR.

The emissivity values were calculated using the following equation (van de Griend and Owe, 1993):

$$\varepsilon = a + b \ln(i) \quad (4.16)$$

With a correlation coefficient of 0.941 with a=1.0094 and b=0.047 at a 0.01 level of significance.

The radiant temperature can be converted into kinetic temperature using the following equation:

$$T_R = \varepsilon^{1/4} T_K \quad (4.17)$$

where, T_R = Radiant temperature (K), ε = Spectral emissivity, T_K = Kinetic temperature (K).

The digital values Landsat-5, TM6 have been converted into kinetic temperature using the above equations. Then applying suitable corrections, land surface temperature mapping has been undertaken and the locations of the mine fires were identified. The isothermalzonation on the basis of temperature gradient has also been undertaken. The temperature of different landcover types was found to be in close agreement with the ground realities as observed in the field and satellite data.

4.3.2.3 Field based methods

In order to estimate the temperature of different surfaces and crack/fires a handheld Raytek radiant thermometer was used. Specification of this instrument has been discussed in Section 4.2.2.3. During field campaign, all measurements were recorded at a typical distance of 1-3m depending on accessibility in that particular area. It should be noted that the Raytek instrument has an operating window of 8–14 μm, whereas band TM6 is located in the range of 10.40–12.50 μm. Due to this difference in operating region of EMR, some errors are to be expected.

4.3.3 Results and Discussions

The Landsat TM recorded on 30 April 1997 of the Raniganj coalbelt and its surrounding area was used for the present study. In terms of the raw data itself, there was good contrast between suspected coalfire area and

the surroundings. After processing the thermal data, some point measurements were undertaken in a nearby water reservoir (located north-west of study area) which has relatively homogenous pixels, for validation purpose. The surface temperature and density sliced image (Fig. 4.10) of the study area displays the different zone of temperatures. The density sliced image shows five temperature zones, four of them are in different colours (blue=coolest and red=hottest) that represents a range of 288 to 341 K. The bright red patches in southwest part of the image show high temperature events due to surface and subsurface coalfires.

The total area can be grouped into five categories (based on ground observations):

- areas of prominent temperature anomalies (in red),
- areas of heat flow from those anomalies and habitation (in white),
- surrounding areas (in yellow),
- vegetated/agricultural land (in cyan) and
- water bodies, swamps (in blue).

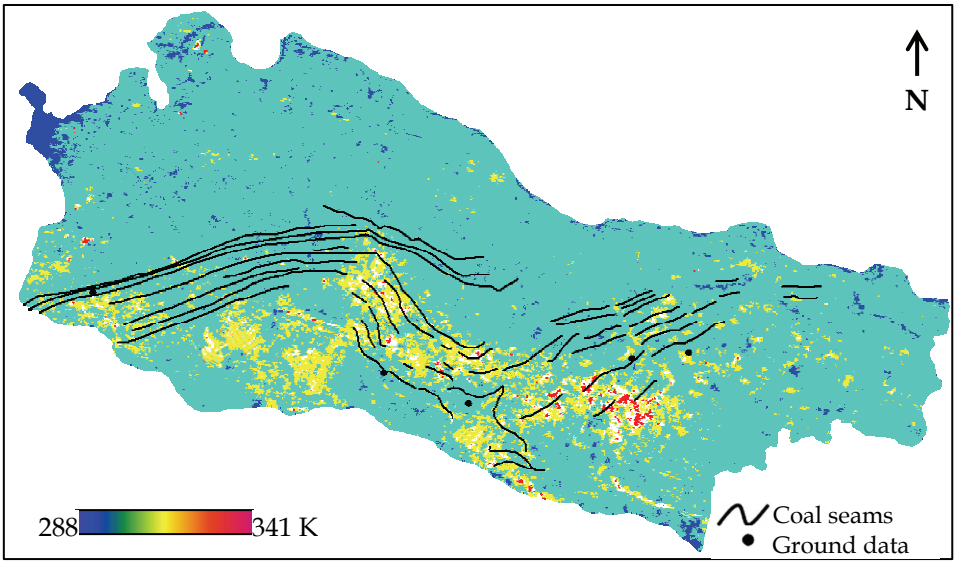

Fig. 4.10: Density sliced surface temperature map with high temperature anomalous areas.

Over water surface the temperature was found to be 288-295 K, whereas the temperature over vegetation was found to be in the range of 294-296 K including agricultural and dense vegetation cover. This is because vegetation tries to attain equilibrium with the air temperature (Metzier *et al*. 1985). The temperatures of barren and fallow lands with sparse vegetation were found to be in the range of 302-311 K, but some absolutely open bare soil and coal spoil dumps display higher temperatures (+313 K). Over the settlements the temperatures were found in the range of 301-307 K. The temperatures on the overburden dumps of the open cast mines were found to be between 301 and 305 K and inside the mine between 308 and 311 K. The maximum temperature was observed over the coal seams, which extends from east to west. The temperatures over the coal seams at some places are more than 323 K. In some places the temperature was found to be as high as 341 K (Fig. 4.11).

Fig. 4.11: Smoke is coming out from a crack from a shallow coalfire on the surface that is partially subsided.

It is known that TM6 saturates at 341 K (Rothery *et al*. 1988). In this study the pixels with saturation temperature are assumed to be the surface coalfire. The possible other hotspots such as factory chimneys were identified during the ground truth survey and with help of Survey of India topographical sheets, and were eliminated from the analysis . The final surface temperature map shows the surface coalfire affected areas (Fig. 4.12) in relation to local geological setting and ground information.

Emissivity is not only a factor affecting the accuracy of satellite temperature data, but also depends on the local atmospheric condition. However, in the present research, the thermal channel data was used

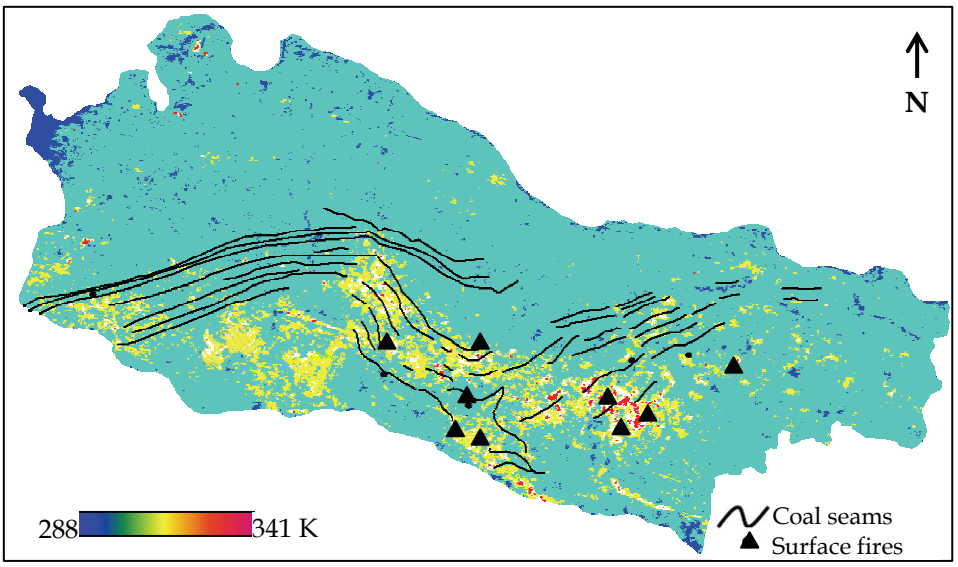

Fig. 4.12: Density sliced surface temperature map with identified surface coalfires.

without any atmospheric correction because during primary validation it was found the temperature difference between processed data and ground truth is very close (±2 K) in a homogeneous area like a water reservoir.

4.4 Conclusions

Since the 1960s, remote sensing has been used as a reliable tool for coalfire detection and monitoring. On the basis of the results of this chapter the following conclusions can be drawn:

In the first case it was observed that ASTER is quite useful for detecting thermal anomalies as accurate as ±1.5 K. But in some cases, inaccurate pixel integrated temperatures are expected because of mixing of high temperature events (coalfires) and background. Also a good knowledge of local geology can interpret and differentiate the coalfire induced anomalies more accurately from some low thermal inertia rocks like basalt (0.53), sandstone (0.54), quartzite (0.74) that can also appear as high temperature event in nighttime thermal image. It is known that in longer wavelength emissivity differs less than shorter wavelength. While estimating temperature using the ASTER band 13 and band 14 emissivity it is found that the temperature range is comparatively narrower than the other three bands (10, 11 and 12). This clearly shows

the effect of the atmosphere over these two spectral regions. Between the two TES methods (NEM and RCM), NEM is more reliable to estimate surface temperature from multispectral thermal remote sensing data like ASTER. Also it has been observed, that in a case of mixed pixel, there is hardly any direct comparison possible between satellite derived temperature and real scenario in the ground. But a wide homogeneous and constant surface like the Yellow river can be used for a more reliable absolute temperature determination for validation purpose. Also a higher spatial resolution data can reveal the coalfire related surface temperature anomalies more accurately by minimizing the effect of mixing of different surface types.

The present study shows that Landsat-5 thermal remote sensing image can reveal the surface temperature anomalies effectively for quantitative study of coalfire. But in some cases, inaccurate pixel integrated temperatures are expected because of mixing of high temperature events (coalfires) and background, which is a major drawback of low resolution data. Furthermore, a good knowledge of local geology can interpret and differentiate the coalfire induced anomalies more accurately from some low thermal inertia rocks. The results also shows use of NDVI derived emissivity can return a more reliable surface temperature rather than use of a fixed emissivity for all types of landcover. However, it should be noted that vegetation type, water content of leaf and view angle can influence the expected result. Although in a mining area like the Raniganj coalbelt, where the average height is between 73 m to 120 m, solar heating does not play an important role in producing false anomalies. However, some overburden dumps of opencast mines with low thermal inertia rocks and coaldust can still appear as false anomalies. Therefore, in order to eliminate solar heating related false anomalies the well established method of DEM correction (Dymond and Shepherd, 1999) can be applied. . However, in a very active mining area like Raniganj, where topography changes rapidly with mining activity, DEM correction is not feasible because of the non-availability of a terrain model during the time of satellite acquisition.

Chapter 5

Monitoring coalfire using remote sensing*

5.1 Introduction

In order to reduce coalfire related GHG emissions it is crucial to understand and manage coalfires effectively. Proper understanding of the nature of migration of a coalfire (i.e. dynamics) could be helpful for a better management of coalfires to reduce the emissions of GHGs in local environment. To understand the dynamics of coalfires multi-temporal thermal infrared data with adequate knowledge of study area can be used for monitoring purposes. Multitemporal spaceborne remote sensing data can be used to study this migration and expresses the results as vectors, indicating direction and speed of migration. In the present study, different thermal infrared images were acquired over time and processed to detect the hotspots and their variation over time in the area under investigation. During geocorrection of the dataset, the sigma value (Σ) was kept less than one pixel so that different layers could be overlaid up to pixel level to avoid positional error. This chapter explores the possibilities of migration of fire by simulating different

*This chapter is based on the following article: Gangopadhyay, P.K., van der Meer, F.D., and van Dijk, P.M. - Monitoring coalfires using remote sensing, *in* Spontaneous Coal Seam Fires: Mitigating a Global Disaster, ERSEC Ecological Book Series, UNESCO, Beijing (in press).

scenarios with the feed from real thermal satellite data and local geological knowledge. The simulated maps were generated in IDL (Interactive Data Language) environment and later crosschecked by thermal satellite data. However, the possibilities of error for human induced interferences such as extinguish/extraction of fire can not be ruled out as seen in the present study area.

5.2 Study area

The study area, the Wuda coalmine area (or Wuda syncline), is located in the Inner Mongolia autonomous region. The area is demarcated in north and west by the Gobi desert, in east by the Yellow river, and in the south by the Helan Mountains. The extent of the Wuda coalmine area from north to south is 10 km and from east to west is 3-5 km, with a total area of 35 km². The Wuda mining region has been subdivided into three mining zones: Wuhushan, Suhaitu and Huangbaici by the mining authority. The details of the study area are discussed in Section 4.2.1. The overview of the study area and test site is shown in Fig. 5.1.

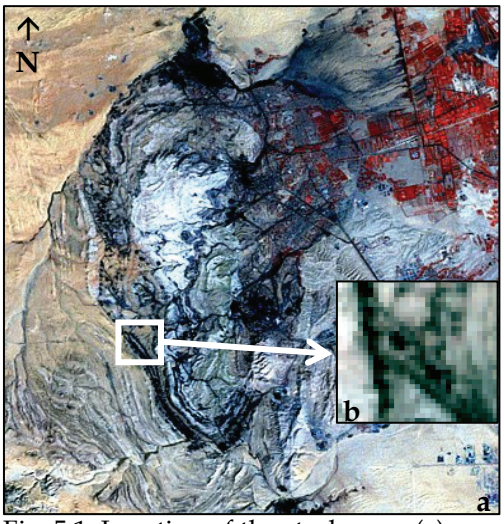

Fig. 5.1: Location of the study area (a) and test site (b).

5.3 Previous research

Modelling plays an important role in coalfire management, in assessment of the current situation, projecting into the future, and especially in the evaluation of alternatives. Based on influence factors, different scenarios can be modelled over decades and centuries and can be evaluated beyond the range of experience.

For a better understanding and management of coalfire several remote sensing/GIS and model based studies have been proposed. Many of the models of spontaneous combustion of coal are based on coalfires of stock piles (Arisoy and Akgun, 1994; Krishnaswamy *et al.*, 1996). To

study the rate of spontaneous combustion of an exposed coal seam, a numerical solution was proposed by Rosema *et al*., (2001). Later a two dimensional model was recommended by Huang *et al*., (2001) where they observed that, in order to enhance natural convection (of coalfire), fractures and higher permeability are necessary. In the present study, a two dimensional model is proposed where crack location and density, rock porosity and seam location along with dip angle were considered as prime factors in order to define the speed of the coalfire. With an adequate knowledge of local geological settings and conditions of the study area (e.g. crack distribution) the model can be a successor of the previous studies for better understanding of coalfires. Furthermore the present study would be a useful tool for prediction of future migration of coalfire for better management of coal resources and reduce GHG emissions.

5.4 Methodology

The methodology of the present study can be divided in two components. The first component deals with processing of thermal remote sensing data and demarcation of surface temperature anomalies related to coalfires. The second component deals with the simulation of coalfires in relation to spatial distribution of coal seams, cracks on the surface, dip angle of the coal seam and properties of overburden rock. A schematic overview of the whole method is shown in Fig. 5.4.

In the EMS, the 3-14 μm region is referred as thermal infrared region (Lillesand and Kiefer, 2000). Thermal remote sensing uses atmospheric windows in 3-5 μm and 8-14 μm regions because these parts of the EMS are not so much affected by atmospheric interaction. It exploits the fact that everything above absolute zero (0 K or -273 C) emits radiation in the thermal infrared region of EMS. Thermal infrared radiation of an object is controlled mainly by the following factors: the emissivity, geometry of the object and its temperature. Thermal infrared sensors record differences in the received infrared radiation from various objects of interest.

Thermal infrared data from Landsat 5 TM of 30 August 1991 (day-time) and Landsat 7 ETM of 12 August 1999 (day-time) were used in this study, along with ASTER-derived DEM of 2002. To reduce the terrain effect, ATCOR3 (Atmospheric and Topographic Correction, version 3) was employed in combination with satellite-derived DEM (Richter 2005).

The digital values of thermal band were converted to spectral radiance using the following equation (Markham and Baker 1986):

$$L_\lambda = L_{\min(\lambda)} + \frac{L_{\max(\lambda)} - L_{\min(\lambda)}}{Q_{cal\max}} Q_{cal} \quad (5.1)$$

where,
L_λ =Spectral radiance, $L_{\min(\lambda)}$ = Minimum detected spectral radiance for the scene (mw cm^{-2} sr^{-1} μm^{-1}), $L_{\max(\lambda)}$= Maximum detected spectral radiance for the scene (mw cm^{-2} sr^{-1} μm^{-1}), Q_{cal}= The grey level for analysed pixel. $Q_{calmax(\lambda)}$ = The maximum grey level.

Once the spectral radiance (L_λ) for TM Band 6 is computed, it is possible to calculate radiant temperature directly by the following equation:

$$T_R = \frac{K_2}{\ln\left(\frac{K_1}{L_\lambda + 1}\right)} \quad (5.2)$$

where,
T_R= Radiant temperature (K), L_λ= Spectral radiance (mw cm^{-2} sr^{-1} μm^{-1})
K_1= Calibration constant (mw cm^{-2} sr^{-1} μm^{-1}), K_2= Calibration constant.

The geo-corrected radiance images of 1991 and 1999 were processed using eq. 5.2, to create isothermal maps with a spatial resolution of 10 m. Local geological and ground-truth data collected in 2002 served to identify potential coal fire areas in these maps.

To define the threshold temperature on the basis of these data, the following procedure was applied:

1) First, the temperature difference between the two images (1991 and 1999) at a specific point of a nearby blackbody (here the Yellow River) for which ground-truth data had been collected during satellite overpass time was determined.
2) This difference was then compensated by adding or subtracting from the threshold value of 2002 (determined by averaging temperatures of different land covers during satellite overpass time).

3) After definition of the threshold value, coal fire locations were identified in the isothermal maps depending on the local geological setting.

To collect ground-truth data of different surfaces and crack/fires a handheld Raytek radiant thermometer was used. This instrument operates in a wide region of temperature (241 to 760 K), spectral coverage (8 to 14 μm) and the emissivity can be defined with a precision of 0.01. A laser pointer makes it easy to point at a particular object from a distance. Most measurements were recorded from a typical distance of ~1 m except for some inaccessible areas.

As expected, few pixels with higher-than-average temperature were found that could be defined as related to active coalfires. In view of the study area's complex mixed land cover, a small plot of 4 km² was therefore chosen to test fire propagation modelling (Fig. 5.1). Coalfire basically is a very local phenomenon and other than coal quality and effective area, few factors such as crack density/location on the surface, physical properties (e.g. porosity) of overburden rock and dip angle of the coal seam play significant role to determine the speed of fire. In the present study the impact of these factors were evaluated.

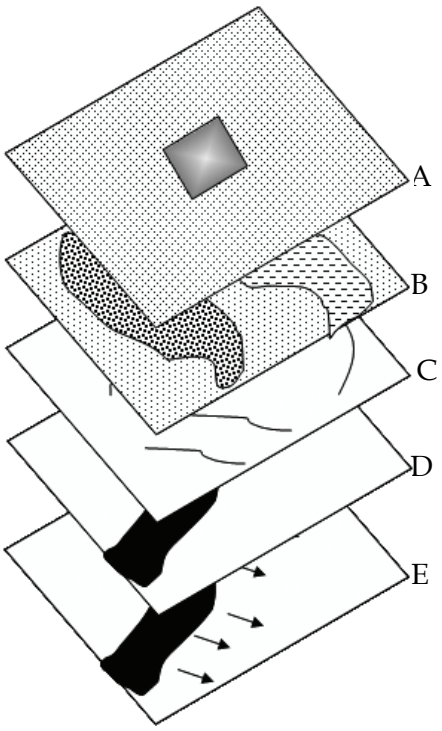

Fig. 5.2: Different layers of the proposed model (A: initiation point, B: rock type, C: crack, D: coal seam and E: dip angle.

A start point of coalfire was identified from 1991 thermal remote sensing data (Landsat TM band 6) of the study area. The method of data processing has been described earlier. The anomalous pixel identified from 1991 remote sensing data was taken as *initiation point* of a coalfire in the model. In IDL environment location and dip

angle of coal seam, crack location and density, porosity of the overburden rock were taken as different layers along with the location of initiation point of coalfire (Fig. 5.2). By considering the weighing factors of different layers with the base speed of coalfire (10 m yr^{-1}) the model is capable to simulate speed of coalfire of a certain pixel. After consuming the 'fuel' of a certain pixel the fire follows the coal seam for next pixels and determines the 'speed of fire' for that pixel. This process continues for a certain predefined time period.

To estimate the significance of each layer, using the aforementioned model different weighing factors were assigned for each layers and tested with changing scenarios.

On average, coalfires propagate 10 m yr^{-1}, as was suggested by the local experts and estimates from field observations. The present study accepts the average speed of coalfire is 10 m yr^{-1} and the effects of contributing factors can increase or decrease the speed. In the present study the effect of dip angle and location of the coal seam was integrated and was used as a single factor for further processing.

At first the weighing factor of coal seam (including dip angle) was assigned as 1.0 and other parameters (crack and porosity of bedrock) were changed in order to estimate the effect of certain layer. Later the weighing factors of different layers were changed to evaluate their significance in the process. The location of initiation point (of coalfire), location of coal seams and cracks are shown in Fig. 5.3.

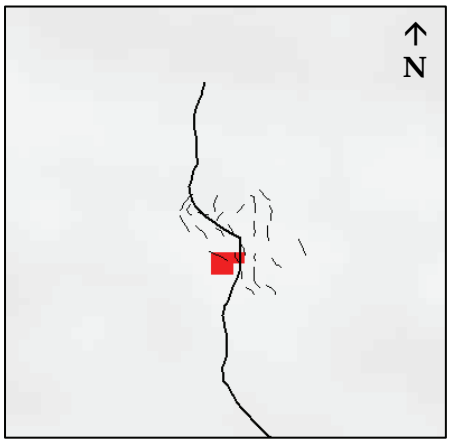

Fig. 5.3: Initiation point in 1991 image with coal seams and cracks.

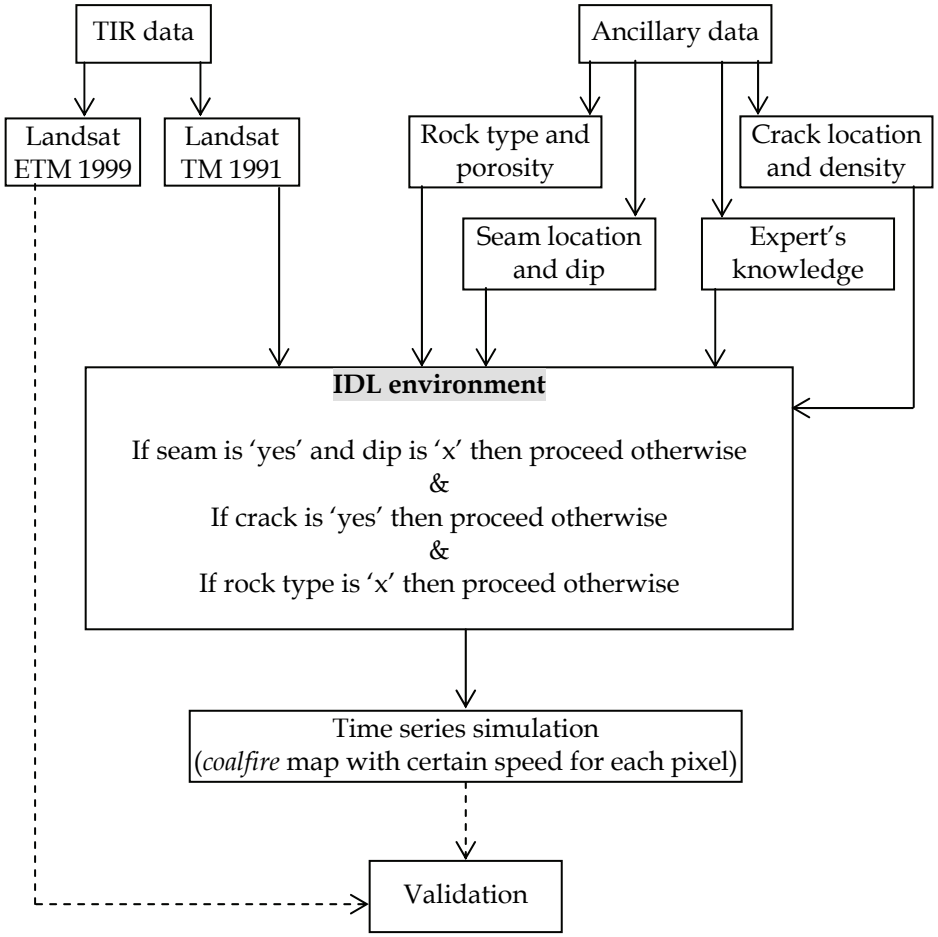

Fig. 5.4: An overview of the proposed model.

5.5 Results and discussion

The effect of the three contributing parameters (seam and dip, crack location and density and rock porosity) were tested with different weighing factors. Some of the results are shown in Table 5.1. It is clear from the observations that sufficient airflows to a coalfire via porous rocks and cracks will increase the speed of coalfires. It was also observed that a higher weighing factor of rock porosity could increase the speed of fire uniformly for each pixel depending on the overburden rock type. With a higher weighing factor, crack could suddenly increase the speed of the fire for few pixels depending on the location and density. The influence of dip angle is the steadiest among the three parameters, and is

inversely proportional to the speed of coalfire (detectable from the surface).

Table 5.1: Weighing factors of different parameters of simulations.

Sl.	Weighing factors			Speed (m)			
	Porosity	Crack	Dip	Min	Max	Mean	Stdev.
1	0.02	0	0	10.00	10.20	10.10	0.14
2	0.05	0	0	9.96	10.21	10.09	0.18
3	0.1	0	0	9.96	11.00	10.48	0.74
4	0.15	0	0	9.96	11.50	10.73	1.09
5	0.2	0.6	0.75	7.45	14.40	10.93	4.91
6	0	1	1	9.96	20.00	14.98	7.10
7	0.2	0.7	0.75	7.44	15.30	11.37	5.56
8	0.2	0.8	0.75	7.49	16.13	11.81	6.11
9	0.2	0.9	0.75	7.44	17.10	12.27	6.83
10	0.2	1	0.75	7.48	18.00	12.74	7.44
11	0.2	0	0.8	7.98	9.60	8.79	1.15
12	0.2	0	0.85	8.48	10.20	9.34	1.22
13	0.2	0	0.9	8.97	10.80	9.89	1.29
14	0.2	0	0.95	9.47	10.50	9.99	0.73
15	0.2	0	1	9.97	12.00	10.99	1.44
16	0.2	0.6	1	9.93	19.20	14.57	6.55
17	0.2	0.7	1	9.92	20.40	15.16	7.41
18	0.2	0.8	1	9.99	21.59	15.79	8.20
19	0.2	0.9	1	9.92	22.79	16.36	9.10
20	0.2	1	1	9.97	24.00	16.99	9.92
21	0.3	0	1	9.99	13.00	11.50	2.13
22	0.3	1	1	9.99	26.00	18.00	11.32
23	0.4	0	1	9.99	14.00	12.00	2.84
24	0.4	1	1	9.99	28.00	19.00	12.73
25	0.5	0	1	9.99	15.00	12.50	3.54
26	0.5	1	1	10.00	30.00	20.00	14.14

In the Fig. 5.5, x and y axis represents different simulation scenarios and speed of coalfire respectively. The simulation results show a wide range of speed of coalfire in different setups.

The following figures (Fig. 5.6 and Fig. 5.7) display an average case and an extreme case (maximum spread over the time). For the average case, the location of the fire was simulated as 10 m yr^{-1} without any influence of the other deciding factors (such as dip angle, rock porosity and crack location and density). For Fig. 5.6, the weighing factor 1.0 was used for rock porosity. It was observed from simulations of different scenarios (using different weighing factors) that rock porosity is the most significant factor to predict the speed of coalfire followed by crack and dip angle respectively (Fig. 5.8). By providing oxygen, cracks are important parameters to continue the burning process. However, cracks could be unevenly distributed over the area, whereas, porous overburden rocks could supply the necessary oxygen more consistently to the active fire.

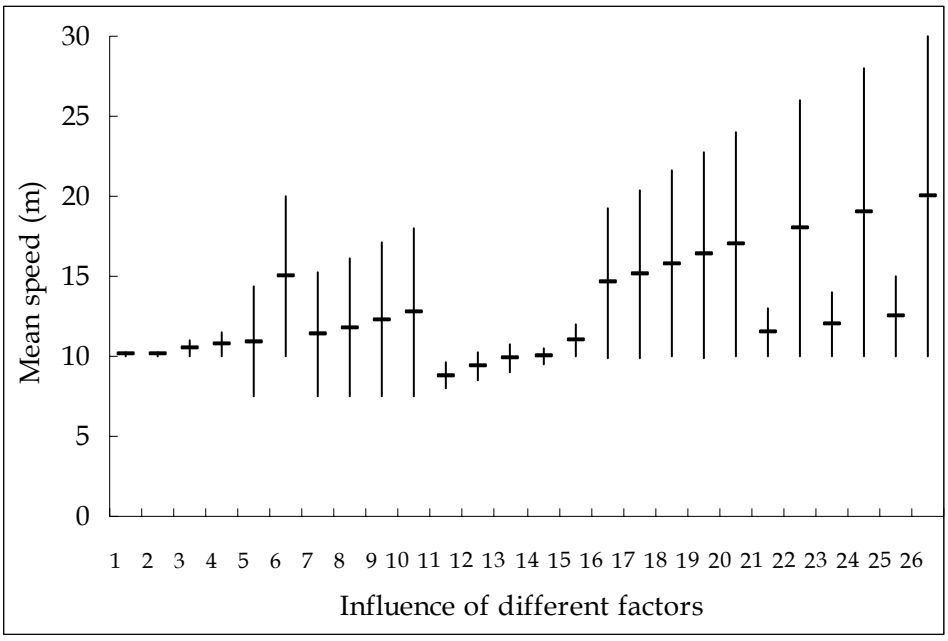

Fig. 5.5: Effect of different parameters with changing weighing factors (as referred in Table 5.1).

However, it should be noted that the maximum dip angle for the coal seam was assigned as 15°. If the other factors are taken constant, the speed of coalfire is inversely proportional to the sine of the dip angle. Also it was observed that if the dip angle is 45° and there is no influence from crack or rock porosity – the fire stops within 2.5 m.

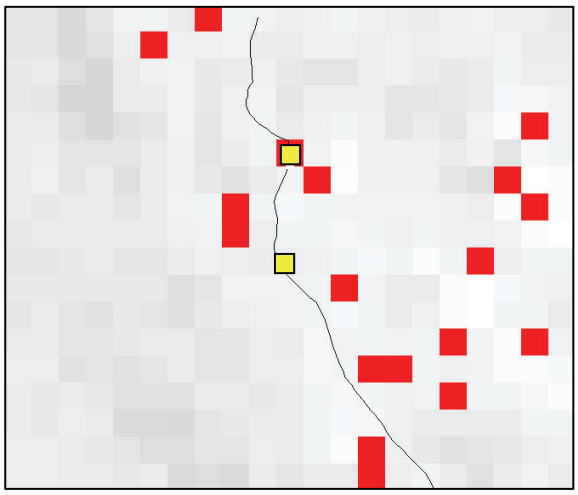

Fig. 5.6: The comparison of processed image (red) and predicted location of coalfires in *average* case in 9 years (yellow).

The predicted locations of fires in 1999 (simulated image) in relation to processed image of 1999 (Fig. 5.6) are not overlapped exactly because of several unpredictable factors (e.g. subsidence, human interference). Nevertheless, it is worth mentioning that other than location of coal seams, dip angle, crack location and density, and rock porosity, the propagation of a coalfire is dependent on a few local factors such as air speed, rain fall (moisture content in the air). The present study does not deal with these factors because of lack of data and simplification of the model. Despite this discrepancy, the present model offers a promising avenue for further research on coal fire propagation and its simulation.

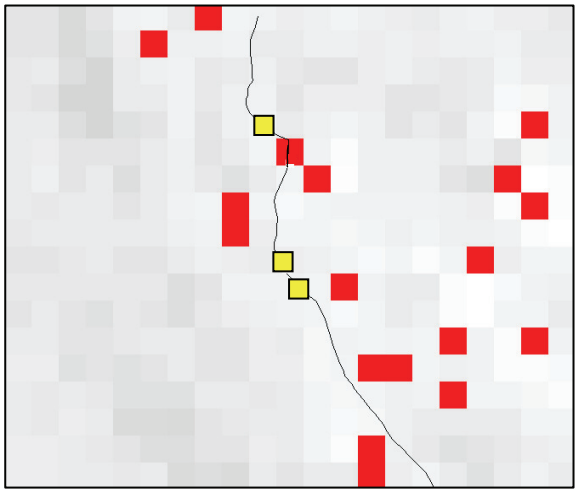

Fig. 5.7: The comparison of processed image (red) and predicted location of coalfires in an extreme case in 9 years (yellow).

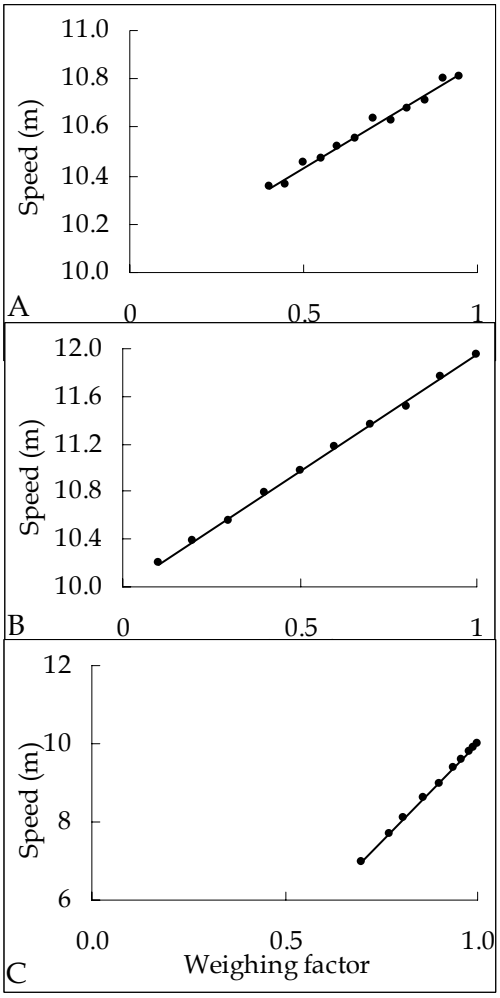

Fig. 5.8: The relation between average speed yr^{-1} and weighing factor (A: Crack, B: Porosity, C: Dip, here dip angle 0°=1 and 90°=0).

5.6 Conclusions

Remote sensing plays an important role in detecting and monitoring coal fires and can help prevent economic loss and environmental disaster. A suitable simulation model with adequate local knowledge have the potential to predict the direction and velocity of coal fire propagation, which may prove useful in fire fighting planning and implementation. The local factors that are mainly responsible for coalfire speed are discussed here. Nevertheless, several uncertainties and

unpredictable factors can decide the final speed of fire and location, such as the sudden increase of oxygen supply by subsidence, which can not be accounted for in the model.

Chapter 6

Atmospheric modelling of CO_2 absorption bands for remote sensing applications*

6.1 Introduction

Over the past two centuries, anthropogenic emissions of greenhouse gases (GHG) have increased to an alarming level. This steady increase of GHGs in atmosphere acts as a blanket that retains solar radiation in the atmosphere and is thought to cause global warming. Among all GHGs, CO_2 has a significant status in this phenomenon. Several researchers suggested that the concentration of CO_2 in the atmosphere has unambiguously increased since the industrial revolution (Keeling and Whorf, 1999; Etheridge *et al.*, 1996). This linear increment of concentration of CO_2 is not only influenced by human activity such as rapid industrialization, deforestation but also some geo-natural events such as leakage from hydrocarbon reservoirs, naturally occurring coalfires etc. In most coal-producing countries, subsurface and surface coalfires are a serious problem, which is evident in China, India,

*This chapter is based on the following article: Gangopadhyay, P. K., van der Meer, F. and van Dijk, P. Atmospheric modelling using FASCOD to identify CO_2 absorption bands and their suitability analysis in variable concentrations for remote sensing applications. *Journal of Quantitative Spectroscopy and Radiative Transfer*, 109(4): 670-683.

Indonesia and other countries (Gangopadhyay *et al.*, 2005a; 2006). It has been estimated that the CO_2 emissions from Chinese coalfires alone contributes about 2-3% of the world's total (Rosema *et al.*, 2001), whereas other scientists suggested this amount to be 0.3% of total CO_2 emitted from fossil fuels (Voight *et al.*, 2004).

Derived from historical data, based on energy source, the total CO_2 emission into the global atmosphere has increased at an alarming rate (Andres *et al.*, 1999)(see Fig. 2.2). Also various researchers have confirmed that current CO_2 concentration has increased to 375 ppmv, which increased the radiative forcing to 1.46 w m^{-2} (Ramaswamy *et al.*, 2001). Currently, the ocean and the land both take up approximately half of the anthropogenic CO_2 emissions, the other half remains in the atmosphere (Mao and Kawa, 2004). The observational foundation of global carbon studies in the National Oceanic and Atmospheric Administration Climate Monitoring and Diagnostic laboratory cooperate air sampling network of worldwide measurements for carbon cycle GHGs (Conway *et al.*, 1990). Approximately fifty six fixed base observatories complemented with ships and aircraft are distributed all over the globe. Their *in situ* measurements are quite accurate but for assessing the global process their distribution is very limited over space and time. Based on this network the observed uncertainty of the global carbon budget is 2-3 GtC yr^{-1} (Tans *et al.*, 1990; Rayner and O'Brien, 2001; Gurney *et al.*, 2002). Undoubtedly, a space borne, high spatial resolution, highly accurate and dedicated sensor could provide much information on global CO_2 distribution in the atmosphere. More precisely, a polar orbiting satellite with low solar zenith angle (to reduce atmospheric scattering) can be quite useful to atmospheric CO_2 retrievals. However, the weaker transitions will have different temperature dependences, pressure broadening, and pressure shift characteristics than the stronger transitions, requiring the best possible knowledge of the line-by-line parameters for all CO_2 transitions in the near infrared spectral window above the 0.3% threshold in order to ensure precise remote sensing retrievals of CO_2. So far an ambitious project has been taken up by JPL, NASA and OCO (the Orbiting Carbon Observatory, which will supposedly be launched in 2008, Miller *et al.*, 2005).

It is possible to infer the spatial distribution of the carbon sources and sinks by using repeated CO_2 measurements on a global network of observatories. The atmosphere is a powerful integrator of the surface

fluxes at large scale, which makes it possible to relate small but persistent concentration gradients to sources and sinks, provided that the air-mass transport is known. Hence atmospheric transport models can be used to interpret atmospheric measurements in terms of surface fluxes by using inverse methods (Enting *et al.*, 1995; Ciais *et al.*, 1995; Rayner *et al.*, 1999; Dufour and Bréon, 2003).

Several instruments such as a Fourier transform spectrometer, lasers, hyperspectral sensors are being used, boarded on air/satellite based platforms for estimation of different atmospheric gases with a proper analysis of atmospheric spectra and reliable retrievals. Some of these models that are based on band ratioing exploit the absorption features of different atmospheric gases in certain wavelengths. However, water vapour retrieval from hyperspectral remote sensing data such as AVIRIS has been standardized (Gao and Goetz, 1990; Schläpfer *et al.*, 1998) because of presence of several wide and distinct water vapour absorption bands in the visible to shortwave infrared range of the electromagnetic spectrum. Nevertheless, retrieval of CO_2 from these types of sensors is still difficult as most of the CO_2 absorption bands situated in the operating range of typical hyperspectral instruments (0.4 to 2.4 μm) are relatively narrow and influenced by other atmospheric gases such as water vapour. However, the problem of narrow absorption bands (>5 nm) can hardly be solved as most of these sensors typically have a bandwidth of ~10nm covering the whole visible and some part of the short-wave infrared region. With a relatively small FWHM, SCIAMACHY is an imaging spectrometer whose primary mission objective is to perform global measurements of trace gases in the troposphere and in the stratosphere. The channel 7 of this satellite was specially designed for CO_2 observations, which unfortunately is now non-operational due to ice formation on sensor (Buchwitz, 2006).

There are only few remote sensing based studies that deal with atmospheric CO_2 retrieval and they are either very coarse resolution (~100 km) or focused on specific atmospheric layers or ground based.

To evaluate the possibilities of CO_2 retrieval from presently available sensors, atmospheric models were simulated in radiative transfer code. These atmospheric models were simulated in FASCOD (Clough *et al.*, 1986), which is a useful tool to perform calculations from the ultraviolet through the visible, infrared & microwave spectrum (0-50000 cm^{-1}). This

radiative transfer model accommodates atmospheric profiles, numerous aerosol models, water and ice cloud models with variable CO_2 concentrations. Spherical refractive geometry calculations are performed for any arbitrary line of sight chosen. Using spectroscopic parameters obtained from the HITRAN (Rothman, *et al.*, 2001), FASCOD performs the line by line calculations.

The present study made an attempt to identify the most CO_2 susceptible bands in the operating region of most present-day hyperspectral instruments with different atmospheric conditions and variable CO_2 concentrations. Identifying these distinct absorption features can help to recognize the most suitable bands of a certain hyperspectral instrument such as HYPERION, AVIRIS etc. As mentioned above, FASCOD was used to simulate different atmospheric conditions and later to establish an empirical relationship between transmission and concentration of CO_2 (ppmv) in simulated atmosphere. Later the precalculated transmission spectra were resampled according to central wavelength and FWHM of some available hyperspectral instruments for sensitivity analysis.

6.2 Radiative transfer in atmosphere

In optical remote sensing the main source of energy is the sun, which contributes more than 99.9% of sensor signal. The Earth's atmosphere modulates any surface signal that affects the distribution of incoming solar radiation at the surface related to the surface reflectance response. Secondly, before reaching to the sensor, the solar radiation reflected by the surface is further scattered and absorbed by the Earth's atmosphere. As most of the remote sensing sensors are positioned in the middle or at the top of the atmosphere, the radiance at sensor is a combined effect of atmosphere and surface. The quantitative study of the transfer of radiant energy through a medium which can scatter, absorb and emit radiation is referred to as 'radiative transfer theory'. The radiation of an incident beam is attenuated by both scattering and absorption in atmosphere. Aerosol particles, cloud drops and gases scatter and absorb as a function of wavelength.

6.2.1 The formal solution

In the case of a beam of monochromatic radiation with radiance $L_\lambda(\lambda, s, \theta, \phi, t)$ which travels a path s in a direction θ, ϕ, the change in radiation

over the distance can be written in the following components, neglecting the changes with time:

$$\frac{dL_\lambda(\lambda,s,\theta,\phi)}{ds} = \varepsilon(\text{spontaneous emission}) + \varepsilon(\text{simulated emission}) + \varepsilon(\text{in - scattering}) + \varepsilon(\text{intrinsic}) - \varepsilon(\text{absorption}) - \varepsilon(\text{out_scattering}) \quad (6.1)$$

The term in-scattering refers to the radiation which is scattered from all directions into a specific direction θ,ϕ. This depends on the radiation field and is given by:

$$\varepsilon(\text{in scattering}) = \frac{k_s^{'}(\lambda,s)}{4\pi}\int_{4\pi} p(\lambda,s,\theta,\phi,\theta',\phi')L(\lambda s,,\theta,'\phi')d\Omega \quad (6.2)$$

where, $k_s^{'}(\lambda,s)$ is the volume scattering coefficient.
Loss of radiation occurs by means of absorption and the scattering or radiant energy out of the beam which are given by:

$$\varepsilon(\text{absorption}) = -k_a^{'}(\lambda,s)L_\lambda(\lambda,s,\theta,\phi) \quad (6.3)$$

and

$$\varepsilon(\text{out - scattering}) = -k_s^{'}(\lambda,s)L_\lambda(\lambda,s,\theta,\phi) \quad (6.4)$$

where, $k_a^{'}(\lambda,s)$ is the volume scattering coefficient. The quantities can be combined as an extinction coefficient $k^{'}(\lambda,s)$:

$$k^{'}(\lambda,s) = k_a^{'}(\lambda,s) + k_s^{'}(\lambda,s) \quad (6.5)$$

Combining all of these terms gives the net gain in radiance per unit length:

$$\frac{dL_\lambda}{ds} = \gamma'(\lambda,s)J(\lambda,s,\theta,\phi) + \gamma''(\lambda,s)L_\lambda(\lambda,s,\theta,\phi) + \frac{k_s'(\lambda,s)}{4\pi}\int_{4\pi} p(\lambda,s,\theta,\phi,\theta',\phi')L_\lambda(\lambda,s,\theta',\phi')d\Omega' + q(\lambda,s,\theta,\phi) - k'(\lambda,s)L_\lambda(\lambda,s,\theta,\phi) \quad (6.6)$$

where, $\gamma(\lambda,s)$ is a coefficient for spontaneous emission and $J(\lambda, s, \theta, \phi)$ is the source function which is independent of the radiation field. Similarly $\gamma'(\lambda,s)$ is the corresponding coefficient for stimulated emission and $q(\lambda, s, \theta, \phi)$ is the intrinsic emission term.

By limiting the description of radiation in an atmosphere in which there are no intrinsic sources, the equation becomes:

$$\frac{dL_\lambda}{ds} = -k'(\lambda,s)\left\{L_\lambda(\lambda,s,\theta,\phi) - \frac{\omega_0(\lambda,s)}{4\pi}\int_{4\pi} p(\lambda,s,\theta,\phi,\theta',\phi')\,L_\lambda(\lambda,s,\theta',\phi')d\Omega' - [1-\omega_0(\lambda,s))]L_\lambda^*(\lambda,T)\right\} \quad (6.7)$$

The formal solution of the time-independent integro-differential equation of radiative transfer (eq. 6.6) can be written as:

$$\frac{1}{k'(\lambda,s)}\frac{dL_\lambda}{ds} + L_\lambda(\lambda,s,\theta,\phi) = -\frac{\omega_0(\lambda,s)}{4\pi}\int_{4\pi} p(\lambda,s,\theta,\phi,\theta',\phi')\,L_\lambda(\lambda,s,\theta',\phi')d\Omega' - [1-\omega_0(\lambda,s))]L_\lambda^*(\lambda,T) \quad (6.8)$$

for which the solution is:

$$L_\lambda(\lambda,s,\theta,\phi) = L_\lambda(\lambda,s_0,\theta,\phi)\exp\left[-\int_{s_0}^{s} k'(\lambda,s')ds'\right] + \frac{1}{4\pi}\int_{s_0}^{s} \omega_0(\lambda,s)k'(\lambda,s)\int_{4\pi} p(\lambda,s,\theta,\phi,\theta',\phi')\,L_\lambda(\lambda,s,\theta',\phi')d\Omega' \exp\left[-\int_{s'}^{s} k'(\lambda,s'')ds''\right]ds' + \int_{s_0}^{s}[1-\omega_0(\lambda,s')]L_\lambda^*(\lambda,T) \exp\left[-\int_{s'}^{s} k'(\lambda,s'')ds''\right]k'(\lambda,s')ds' \quad (6.9)$$

where s is a general point along the path and s_0 is a boundary. Here the first term represents the attenuation of the boundary radiance, second term represents the contribution of all scattered radiation along the path and the last term represents the thermal radiance along the path (LaRocca and Turner, 1975).

6.3 Research approach

CO_2 is the main constituent among the fixed gases in absorption and emission of atmospheric radiation. It is a well mixed and long lived GHG and has shown a consistent long-term trend at the different observations across the hemisphere for the past half century (NOAA, 1999). As a chemically unreactive gas, CO_2 has its main sources and sinks at the Earth's surface. Its concentration is variable in the planetary boundary layer (PBL), but at higher levels its mixing ratio is nearly constant below the dissociation level of molecular oxygen (~90 km), above this level, CO_2 dissociates and its concentration is quickly reduced with altitude (Fig. 6.1).

As a polyatomic molecule, CO_2's three atoms lie along a straight line with the two oxygen atoms equidistant from the carbon atom. Such a molecule has nine degrees of freedom, i.e. nine numbers are needed to describe the motions of its atoms: three for translation, two for rotation, and four for vibration. The stretching and bending of the bonds in the internal modes produces the infrared absorptions seen in CO_2 spectra. Out of the four vibrational modes, three are vibration-rotation bands (two of which are the same frequency and are responsible for the fundamental-vibration spectra of CO_2) and a fourth band that is infrared inactive. Other absorptions are seen in CO_2 spectra, and these

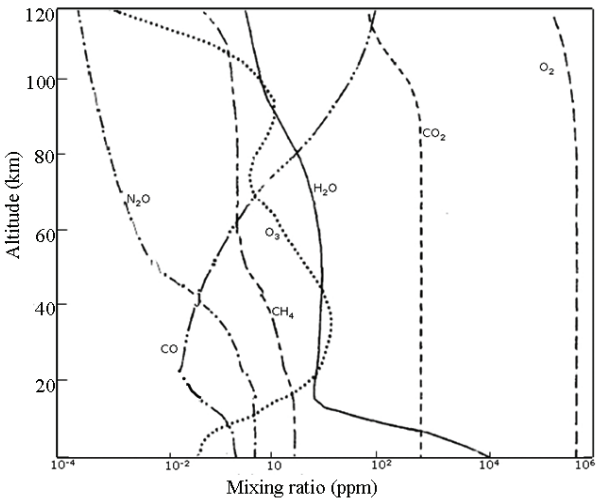

Fig. 6.1: FASCOD simulated mixing ratios of main atmospheric constituents.

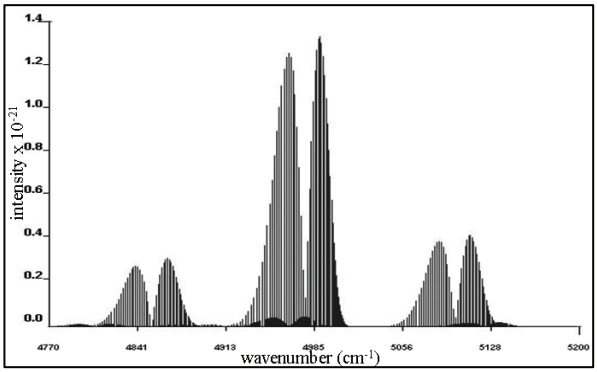

Fig. 6.2: CO_2 line intensities in HITRAN data base (JavaHAWKS output).

are due to overtones and combinations of the original fundamentals. The near-infrared absorptions of interest in this study are combination bands cantered around 2.0 µm. Intensity of absorptions are affected by both the level of fundamental mode (Gaffey *et al.*, 1993), and the relative amount of the material causing the absorptions (the total absorptance increases with the amount of material present) (Schurin and Ellis, 1968). Widths of bands are greatly affected by temperature and pressure, with increasing values causing absorptions to widen (Martini, 2002).

Radiance at satellite in a specific CO_2 absorption band can reflect the total columnar CO_2. There are several CO_2 absorption bands in the incoming solar radiation and outgoing atmospheric thermal emission (i.e. infrared and thermal infrared zone of spectrum). The strong CO_2 emission bands at 15 and 4.3 µm are used to derive atmospheric temperature profiles, with an assumption that the CO_2 concentration through the whole atmosphere is fixed (Smith, 1970; Chahine, 1970; Rodgers, 1976, McMillin and Fleming, 1976). However, the sensitivity of space-observed radiance to emission temperature in both bands is much larger than the sensitivity to CO_2 concentration change. In addition, water vapour has significant interference in both bands.

Several dedicated and specific research oriented and few commercial radiative transfer codes are being used by researchers. Among them 6S (Vermonte *et al.*, 1997), SBDART (Ricchiazzi *et al.*, 1998), RATRAN (Hogerheijde and van der Tak, 2000), RTTOV (Saunders, *et al.*, 1990), ARTS (Buehler *et al.*, 2005), AMARTIS (Miesch, *et al.*, 2000), MODTRAN (Kneizys *et al.*, 1996) and FASCOD (Clough *et al.*, 1986) are well-known.

FASCOD calculates spectral transmittance, radiance, or optical depth for a given path by using line-by-line calculation for very high spectral

resolution. FASCOD uses a line-by-line calculation algorithm with continuum models, a spherical refractive geometry package and standard atmospheric and aerosol profiles in order to provide a real world atmospheric model. Spectral lines (emission or absorption) occur at very specific monochromatic frequencies, but in reality these single frequency emissions are broadened, both by collisions with other molecules and by Doppler's shifts caused by the velocity of the radiating molecule. In the present study, FASCOD was used in combination with the HITRAN2K spectral database to simulate atmospheric models.

The HITRAN2K database includes thirty two molecular species along with values of cross-sections of heavy molecules such as CFCs (Varanasi and Nemtchinov, 1994). The spectral absorption, transmission and emission of radiation in the atmosphere are influenced by the shape, location and intensity of the absorption line. The HITRAN database provides line position (cm^{-1}), the intensity of the transition (cm^{-1} $molec^{-1}$ cm^2), air-broadened half width (cm^{-1} atm^{-1}) and the energy of the lower state of the transition (cm^{-1}). In Fig. 6.2 CO_2 line intensities are shown in the range of 4770 – 5200 cm^{-1} (1923.08 – 2096.44 nm).

In the present research, FASCOD was used to simulate customised atmospheric conditions with different CO_2 concentrations (330–570 ppmv) with 31 other atmospheric gases including CFCs. All the models were constructed based on conditions expected in a possible test area in a coal mining region in northern China. The mid-latitude winter was used for atmospheric profiles with an extension up to 100 km with a '*desert extinction*' type and range. The vertical layers of the models were defined by default values by FSTCAM which generates an optimum layering arrangement from a default model atmospheric profile/radiosonde data. Default values for the Voigt parameter ratio and temperature difference provided a good compromise between run-time length and lineshape accuracy.

6.4 CO_2 absorption bands and their suitability analysis

To identify the discrete CO_2 absorption bands, two types of atmosphere were simulated using FASCOD considering the atmospheric conditions expected in the proposed study area. The first simulated atmosphere consists of only CO_2 i.e. without water vapour, other atmospheric gases and aerosol. The other consists of all atmospheric constituents except CO_2. Later these two data sets were resampled in 1 nm resolution to

understand the phenomenon in the range of 700-2500 nm that covers most of the hyperspectral remote sensing sensors. From Fig. 6.3, it is evident that energy is being influenced simultaneously by CO_2 and all other atmospheric constituents throughout the spectrum below ~2000 nm. At around 2000 nm, the energy is only absorbed by a few strong CO_2 absorption bands. For clarity, a close-up of that part of spectrum (1.995-2.014 µm) is shown in Fig. 6.4.

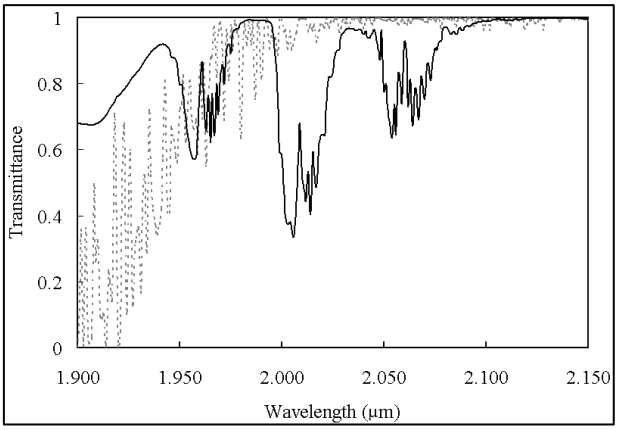

Fig. 6.3: Absorption of CO_2 (black line) and other atmospheric gases (dotted line) in the wavelength region of 1.9-2.15 µm.

As seen in Fig. 6.3 and 6.4, the 1.998-2.003 µm and the 2.007-2.013 µm ranges apparently have the lowest influence of other atmospheric gases than CO_2 of the whole spectrum. The detailed view of Fig. 6.4 shows that very strong CO_2 absorption lines are present at 1.998, 2.001, 2.010, and 2.016 µm which are not significantly influenced by other atmospheric gases.

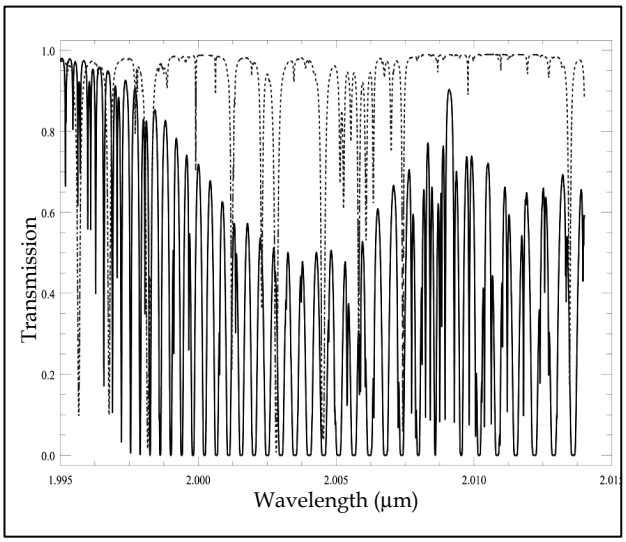

Fig. 6.4: Absorption of CO_2 (black line) and other atmospheric gases (dotted line) in the wavelength region of 1.995-2.014 µm.

To estimate the significance of these

absorption bands, partial least square regression (PLSR) was used with different concentrations of CO_2 (330-570 ppmv) in the same wavelength region. Among the significant bands three absorption bands were chosen which are not influenced by any other atmospheric constituents such as water vapour. These three bands are situated at 1.998, 2.001 and 2.01 μm (Fig. 6.5). Later, one of these three particular absorption bands (2001 nm) was tested with different concentrations of CO_2 to find out their sensitivity with changing gas concentration (330-570 ppmv), which appears to be a good relation between CO_2 concentration and transmission (Fig. 6.6).

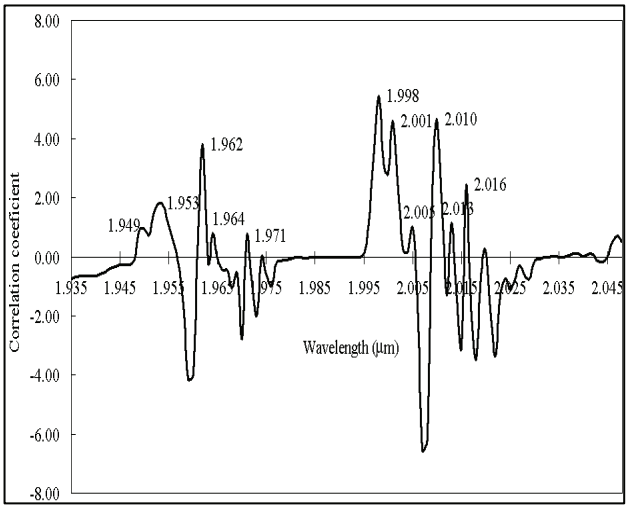

Fig. 6.5: Distribution of significant CO_2 absorption bands.

To understand how much it can influence the energy in that particular region, different concentrations (ppmv) of CO_2 were used to simulate atmospheric models. The present atmospheric concentration of CO_2 (375 ppmv) was taken as a base and then different higher concentrations of CO_2 were plotted using the same model. The concentrations were observed in the test

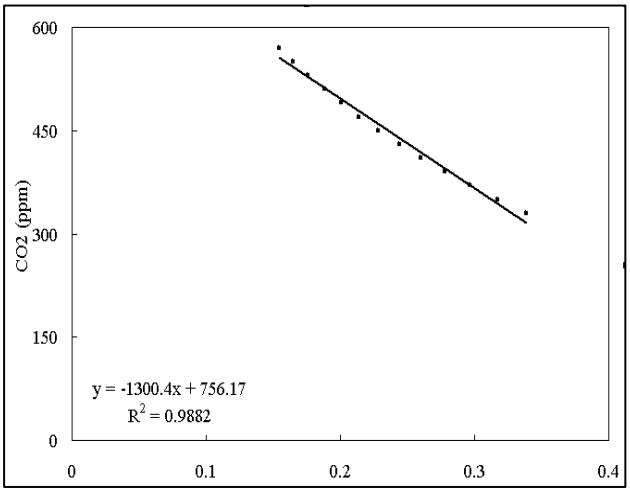

Fig. 6.6: Relation between CO_2 concentration and transmission at 2001nm.

area of northern China have a range of 407 to 127994 ppmv (407, 421, 70762, 86189, 100558, and 127994 ppmv). It was observed that the transmittance had decreased with the increment of CO_2 concentration and in the case of 70762 ppmv (as in an analyzed gas sample, collected from a vent in a coalfire in northern China), the transmittance had decreased drastically. As stated earlier, *in situ* measurements are much more accurate whereas the accuracy level falls significantly with the increment of field of view and height of the measuring sensor. Other than these two factors, the local wind speed/direction can play an important role to finalize the CO_2 concentration in the PBL in a certain line of view. However, for a spaceborne sensor, located at ~700 km over earth's surface, these factors will play a bigger role because of the larger path length.

6.5 FASCOD simulated models and sensor suitability analysis

Noise is a random background event which has to be dealt with in every signal processing system. Basically, noise could be caused by a wide range of sources such as detector sensitivity, atmospheric variations, nature of radiation, transmission or quantization errors. There are several systems currently available which deal with these superfluous signals in order to extract the real signal. However, an attempt was made here by introducing additive and multiplicative noise in reference spectra in order to understand the sensitivity of some remote sensing sensors (AVIRIS, DAIS, HYMAP and Hyperion) for their suitability to determine the variation of CO_2 in certain wavelengths.

The additive noise was modelled based on a zero-mean Gaussian distribution ($N\sim(\mu,\sigma^2)$) described by its standard deviation or variance by using central wavelength and FWHM of a certain remote sensing sensor.

As atmospheric transmission statistics are not strictly Gaussian and small bump and other deviations from Gaussian probability distributions are often experienced, multiplicative noise was introduced by LN of Gaussian distribution on model spectra that are resampled in bandwidth of different sensors.

Additive and multiplicative noises were added to the full spectrum of 700 to 2500 nm on FASCOD simulated model which are resampled

based on central wavelength and FWHM of certain sensor. The results are presented next to model spectra in Fig. 6.7 for a visual comparison. The relation (R^2) between every sensor and model spectra is presented in Table 6.1. It is evident from the Table, that for an additive noise scenario, all the sensors are not very much influenced. Nevertheless, in the case of multiplicative noise, DAIS returned the worst scenario whereas Hyperion is much more consistent.

Table 6.1: Relation between reference and noise added spectra for different sensors.

Sensor	Additive noise	Multiplicative noise
AVIRIS	0.9997	0.9779
DAIS	0.994	0.8566
HYMAP	0.9985	0.9019
Hyperion	0.9997	0.9832

Furthermore, the same additive and multiplicative noise models were introduced to FASCOD simulated spectra in the 1850-2050 nm region with the specific spectral resolution of certain remote sensing sensor with variable CO_2 concentrations (ppmv). The results of additive and multiplicative noise added spectra with reference spectra are presented in Fig. 6.8 and Fig. 6.9 respectively. However, only results of the lowest and the highest concentrations of CO_2 are displayed. The relation (R^2) between reference spectra and noise added spectra are presented in Table 6.2. As seen in the following table, additive noise on AVIRIS, HYMAP and Hyperion has no effect, but DIAS has little displacement with the change of CO_2 variation. For multiplicative noise: AVIRIS, Hyperion and HYMAP closely agree with in next reference spectra and DAIS to a lesser extent.

Table 6.2: Relationship between reference and noise added spectra with different CO_2 concentration.

	AVIRIS		DAIS		HYMAP		Hyperion	
CO_2 conc.	Add.	Multi.	Add.	Multi.	Add.	Multi.	Add.	Multi.
330ppm	1	0.9992	0.999	0.9902	1	0.9979	1	0.999
390ppm	1	0.9955	0.999	0.9898	1	0.998	1	0.999
450ppm	1	0.997	0.999	0.988	1	0.998	1	0.999
510ppm	1	0.9996	0.999	0.9891	1	0.9981	1	0.999
570ppm	1	0.9971	0.999	0.9887	1	0.9982	1	0.999

6.6 Error contributing factors

Several factors, such as spatial/spectral resolution, sensor noise, scattering can contribute to a significant amount of error on CO_2 retrieval. The present research has not discussed the error contributing factors sensor specifically. The following paragraphs discuss the main error contributing factors in general.

A sensor with larger footprint can retain higher SNR, but it increases the possibilities of heterogeneity of landcover and makes CO_2 retrieval much more complicated. Therefore, the spatial resolution of the sensor should be in a range such that the SNR will be acceptable.

As most of the sensors have a typical spectral resolution of ~10 nm (which is wider than CO_2 absorption bands in the SWIR range) a suitable absorption window should be selected in order to avoid interference from atmospheric constituents e.g. water vapour. Although in a wider absorption window the overall retrieval error will be less, in a narrower window scattering by aerosol and the H_2O continuum can be assumed to be constant. Additionally at a certain sampling rate, a narrower spectrum will be acquired faster and thus less contaminated by the artefacts due to the spatial variation of surface reflectance, pressure, temperature profile, and gas abundances as the instrument's instantaneous field of view moves across the Earth (Dufour and Bréon, 2003).

Sensor noise mostly is a summation of spectrometer noise, detector noise, and sampling position uncertainty, depending on the type of instrument. In the present study, Gaussian noise and LN of Gaussian noise were introduced to sample spectra to observe the deviation from original spectra with variable CO_2 concentration without further processing (such as inverse modelling).

6.7 Conclusions

Coalfire is a wide spread environmental problem in most coal producing countries. To detect and monitor coalfires, remote sensing can play a significant role in planning for prevention of huge economic loss and environmental disaster. The green house gases emitted from coalfires need to be quantified more seriously as coalfire related green house gases have a significant adverse contribution to global warming. As seen in the present study, the relationship between total transmission and

concentration of CO_2 strongly agrees in specific wavelengths. Although most hyperspectral instruments operate in the visible and shortwave infrared range where the absorption bands of CO_2 are very narrow, still there is an option to scale down the parameters retrieved from models (laboratory based) and fit in the available remote sensing bands. However, a more dedicated and higher spectral resolution sensor with low sun angle could retrieve atmospheric CO_2 concentration more accurately in order to understand the global carbon budget more effectively.

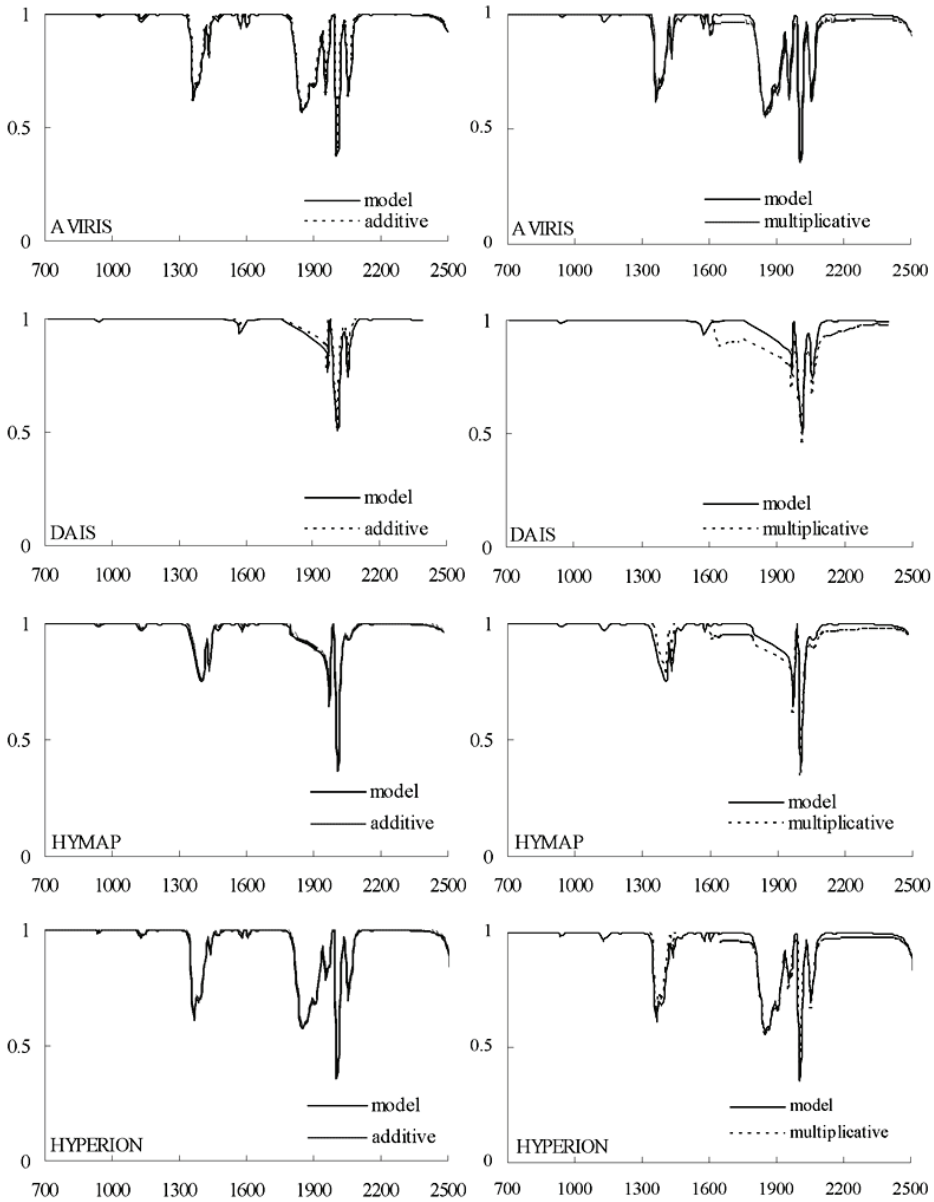

Fig. 6.7: Additive and multiplicative noise simulation using central wavelength and FWHM on AVIRIS, DAIS, HYMAP and HYPERION respectively in relation to CO_2 absorption lines (here x-axis and y-axis represent wavelength (nm) and transmittance respectively).

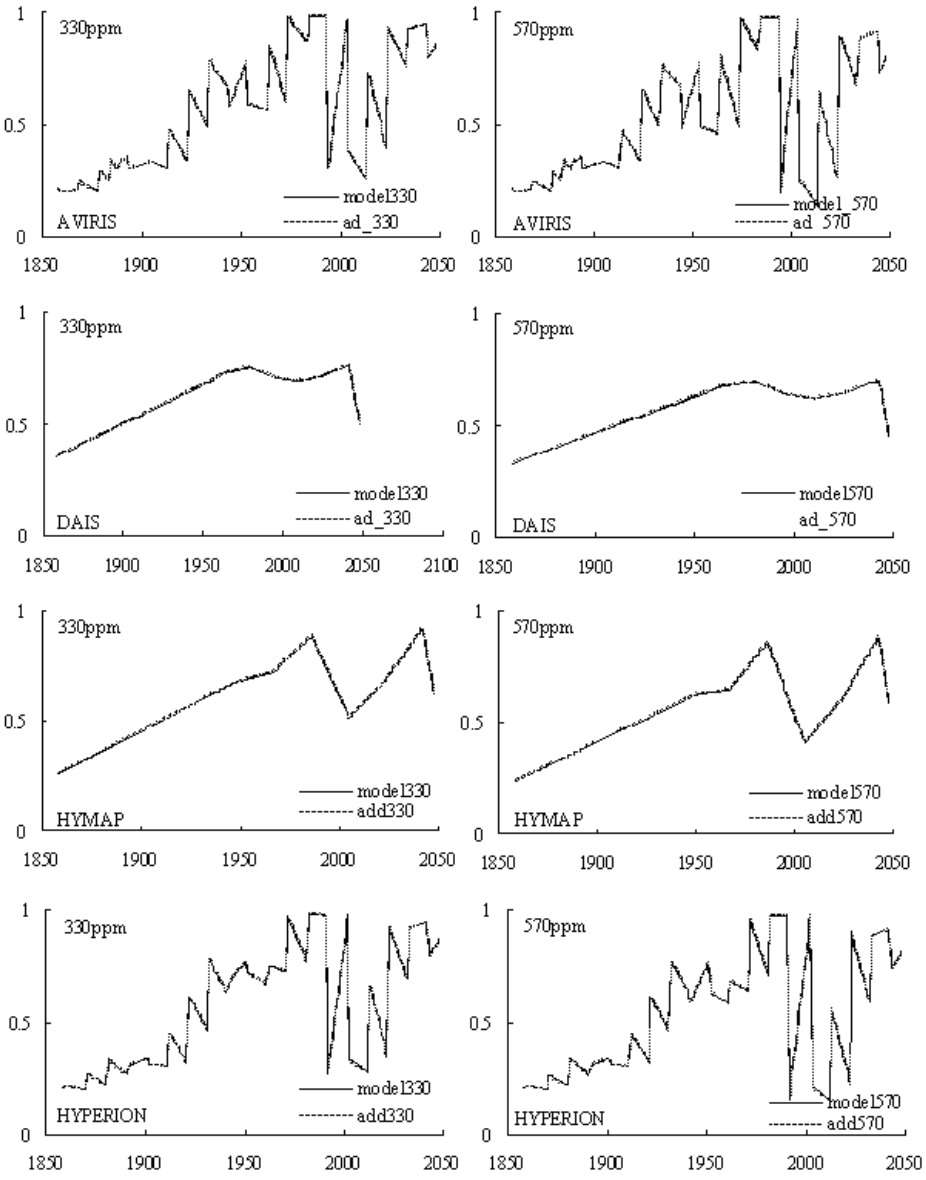

Fig. 6.8: Additive noise simulation in low (330ppm) and relatively extreme concentration (570ppm) on CO_2 absorption bands related to AVIRIS, DAIS, HYMAP and HYPERION sensors respectively in 1nm resolution (here x-axis and y-axis represent wavelength (nm) and transmittance respectively).

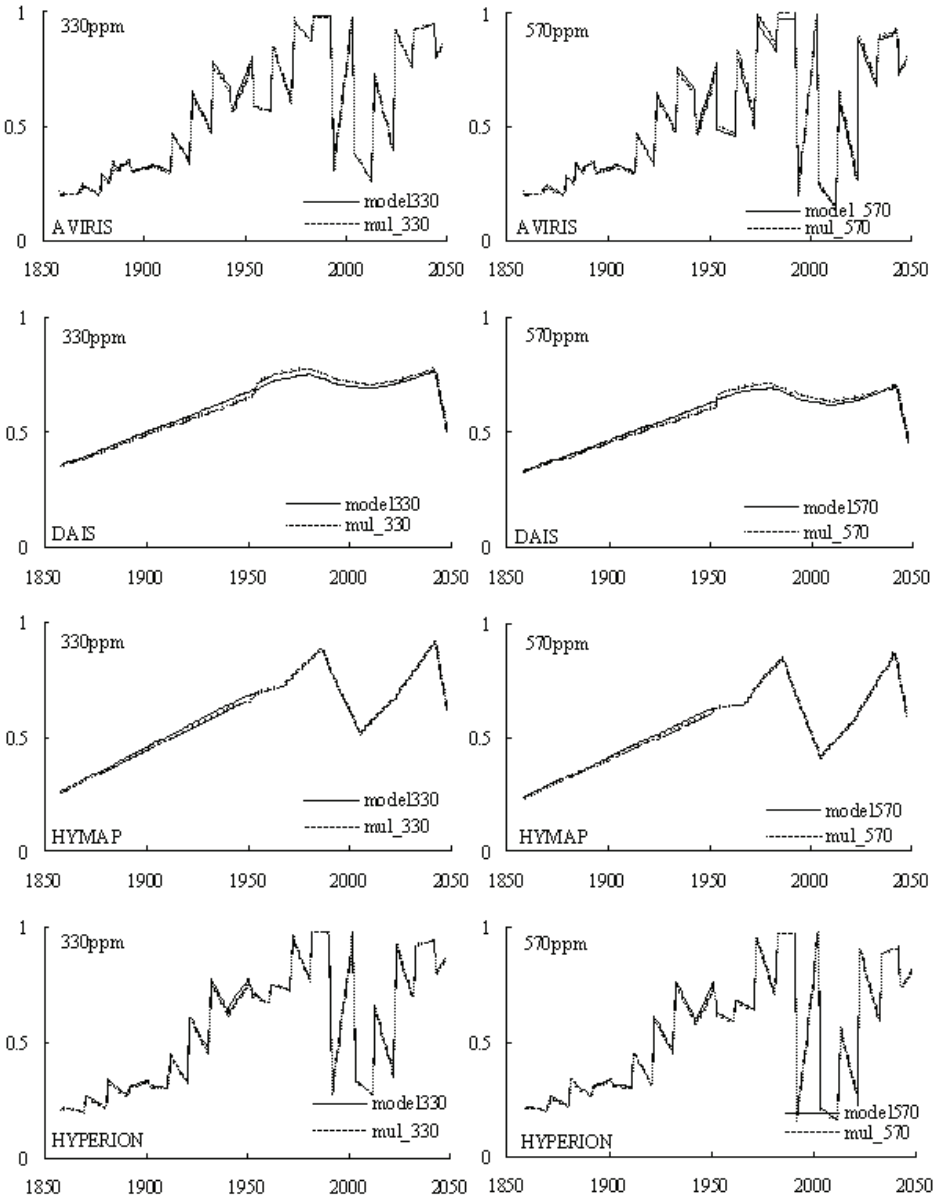

Fig. 6.9: Multiplicative noise simulation in low (330ppm) and relatively extreme concentration (570ppm) on CO_2 absorption bands related to AVIRIS, DAIS, HYMAP and HYPERION sensors respectively in 1nm resolution (here x-axis and y-axis represent wavelength (nm) and transmittance respectively).

Chapter 7

Detecting anomalous CO_2 flux using spaceborne spectroscopy*

7.1 Introduction

Over the time-scale, the Earth's atmospheric CO_2 concentration has varied and that is mostly determined by balance among the geochemical processes including burial of organic carbon in sediments, silicate rock weathering and volcanic activity. As discussed earlier, the best recorded atmospheric CO_2 variability is derived from the Vostok ice core that records last four glacial/interglacial cycles. The present CO_2 concentration of the Earth's atmosphere has exceeded more than was originally predicted from the ice core data. Other than rapid industrialization and urbanization since last century, geo-natural hazards such as volcanic activity, leakage from hydrocarbon reservoirs and spontaneous combustion of coal have all contributed to a considerable amount of CO_2 that has been released into the atmosphere.

Though remote sensing based coalfire study is well established, coalfire related CO_2 quantification from remote sensing data has not yet been endeavoured by scientific communities because of low spectral

*This chapter is based on the following article: Gangopadhyay, P. K., van der Meer, F. and van Dijk, P. - Detecting anomalous CO_2 flux using space borne spectroscopy. *International Journal of Applied Earth Observation and Geoinformation* (in press).

resolution of commercially available remote sensing data, and relatively sparse CO_2 plume than other geological hazards like volcanic activity.

Numerous instruments such as a Fourier transform spectrometer, lasers, hyperspectral sensors are being used, boarded on air/satellite based platforms for estimation of different atmospheric gases with a proper analysis of atmospheric spectra and reliable retrievals. One of the most popular methods is band ratioing for columnar water vapour retrieval. Columnar water vapour retrieval is much straightforward than CO_2, as CO_2 has much narrower absorption features than water vapour and is frequently influenced by other atmospheric gases such as water vapour.

However, the problem of narrow absorption bands (>5 nm) can hardly be solved, as most of the present remote sensing sensors typically have a band width of ~10 nm covering the whole visible and some part of the short-wave infrared region. The present study is based on a spaceborne hyperspectral sensor, namely Hyperion. The Hyperion pushbroom instrument (boarded on Earth Observing 1 satellite) has been designed in order to provide hyperspectral data of the Earth's surface. Hyperion acquires spectra of 7.7 km across track with a spatial resolution of 30 m. It has two spectrometers, one in VNIR range (bands 8-57, 427-925 nm) and other in SWIR region (bands 77-224, 912-2395 nm). For the present research, from FASCOD simulated transmission spectra of atmosphere, two bands of Hyperion (acquired on 09.09.2003) were selected (B185 and B186) that are close to 2.0 µm.

In the measured spectrum of a sensor (from the top of the atmosphere (TOA)) each atmospheric species leaves a specific absorption feature by which it can be identified and quantified (in the required resolution). By exploiting differential absorption features (up to today) several band ratioing methods are being used to estimate columnar abundance of different atmospheric species. Among them Narrow-Wide (N/W: Frouin *et al*., 1990), Continuum Interpolated Band Ratio (CIBR: Green *et al*., 1989, Bruegge *et al*., 1990; Kaufman and Gao, 1992) and Linear Interpolated Regression (LIRR: Schläpfer *et al*., 1996) are being used by research community. The present study examines the possibilities of CO_2 columnar retrieval by using CIBR method (Green et al., 1989) because of its straight forward approach.

Another goal of this study is to investigate the relation between radiance

at sensor and concentration of CO_2 plume emitted from certain event (in this case coalfire) to retrieve concentration of CO_2 (per pixel) from hyperspectral image. Based on FASCOD simulations a simplified atmospheric model was developed to retrieve the CO_2 plume related radiance and later this information was inversed to retrieve coalfire related CO_2 concentration up to a fixed altitude.

7.2 Study area

The study area, the Wuda coalmine area (or Wuda syncline), is located in Inner Mongolia's autonomous region in north China. The area is demarcated in the north and the west by the Gobi desert, in the east by the Yellow river, and in the south by the Helan Mountains. The extent of the Wuda coalmine area from north to south is 10 km and 3-5 km from east to west , with a total area of 35 square km. The Wuda mining region has been subdivided into three mining zones: Wuhushan, Suhaitu and Huangbaici by the mining authority.

The first coalfire was recorded here in 1961 in a small coalmine pit. Before 1989, the coalfires in Wuda were isolated and scattered in different places, which gradually combined between 1989 and 1995, and are known to be rapidly spreading since 1995. According to BRSC's (Beijing Remote Sensing Centre) estimation in 2002, the total area affected by coalfires is 3.07 million m^2 covering 8.8% of the total area of the Wuda syncline (Source: Wuda Mining Authority). The details of the study area are described in section 4.2.1.

7.3 Research approach

Theoretically, the sun is the main energy source in optical remote sensing apart from the negligible thermal radiation. The Earth's atmosphere modulates any signal twice before it reaches the sensor by means of absorption and scattering. As most of the remote sensing sensors are positioned in the middle or at the top of the atmosphere, the radiance at sensor is a combined effect of atmosphere and surface. The radiation of an incident beam is attenuated by both scattering and absorption in atmosphere. Aerosol particles, cloud drops and gases scatter and absorb energy as a function of wavelength.

As a chemically unreactive, well mixed and long lived gas, CO_2 has its main sources and sinks at the Earth's surface. Depending on surface conditions, CO_2 concentration can vary in the PBL, but at higher levels

its mixing ratio is nearly constant below the dissociation level of molecular oxygen (~90 km) (Mao and Kawa, 2004).

As a polyatomic molecule, CO_2's three atoms lie along a straight line with the two oxygen atoms equidistant from the carbon atom. The stretching and bending of the bonds in the internal modes produces the infrared absorptions seen in CO_2 spectra. There are several CO_2 absorption bands in the incoming solar radiation and outgoing atmospheric thermal emission (i.e. infrared and thermal infrared zone of spectrum). The near-infrared absorptions of interest in this study are combination bands centred around 2.0 μm.

To estimate CO_2 concentration based on absorption feature in certain wavelength from remote sensing sensors it is helpful to simulate same atmospheric conditions in controlled environment. Radiative transfer codes such as FASCOD (Clough *et al*., 1986) are able to simulate specific atmospheric conditions with variable atmospheric gas compositions and concentrations.

In the present study, FASCOD was used that calculates spectral transmittance, radiance, optical depth for a given path by using line-by-line calculation for very high spectral resolution. FASCOD uses HITRAN2K (Varanasi and Nemtchinov, 1994) spectral database to simulate atmospheric models. To simulate atmosphere (as it is expected in the study area), a boundary layer aerosol 'rural' and 'desert extinction' with a 'fall-winter' seasonal aerosol profile was used and for the stratospheric aerosol profile, a 'background stratospheric' was used. For cirrus clouds scattering calculation 'NOAA Cirrus Profile' was used with 'Cirrus Thickness' 1.0 km and 'Cirrus Base Altitude' 8.0 km in FASCOD.

In the present study, two methods were evaluated for atmospheric CO_2 retrieval. The first method, namely CIBR is a well used method for atmospheric column averaged water vapour retrieval. However, it is worthwhile mentioning that CO_2 has much narrower absorption bands than water vapour and frequently interfered by other atmospheric constituents. The second method attempts to establish an empirical relation between CO_2 plume related radiance and CO_2 concentration. First, it identifies the different components of radiance at sensor and then extracts the CO_2 plume related radiance from radiance at sensor.

Finally, it delivers CO_2 concentration (map) by inversing the CO_2 plume related radiance using a regression model.

7.4 Parameters calculation using FASCOD

In order to identify the most suitable CO_2 absorption bands in the VNIR/NIR range two types of atmosphere were simulated. The first simulated atmosphere consists of only CO_2 i.e. without water vapour, other atmospheric gases and aerosol. The other consists of all atmospheric constituents except CO_2. Later these two spectra were overlaid to identify the distinct CO_2 bands that are not influenced by other atmospheric constituents such as water vapour (Fig. 6.3). Later to estimate the significance of these absorption bands, PLSR was used with different concentrations of CO_2 (370-570 ppmv) in the same wavelength region. As observed from the result (Fig. 6.5), the most significant two absorption bands (2.001 and 2.01 μm) were chosen, since they were not considerably influenced by any other atmospheric constituents such as water vapour. These absorption bands are very close to central wavelength of Hyperion B185 and B186 (2.002 and 2.012 μm).

7.5 Estimating CO_2 concentration using the CIBR method

By exploiting the differential absorption features of atmospheric species, there are several band ratioing algorithms that have been developed. In the present study, CIBR was used to observe the possibilities of atmospheric column CO_2 retrieval in a coalfire affected area by this method. The CIBR method performs a ratioing between the radiance at channels within the absorption feature (measurement channels) and an interpolated radiance of channels in its vicinity (reference channels) to detect the relative strength of the absorption. The outcome is related to the total columnar concentration of certain atmospheric species (Green *et al*., 1989; Bruegge *et al*., 1990; Kaufman and Gao, 1992; Carrere and Conel, 1993).

In the present study Hyperion B185 and B186 (2002 and 2012.1 nm, measurement channels), B183 and B188 (1981.8 and 2032.3 nm, reference channels) were selected (Fig. 7.1) to estimate CO_2 concentration using the CIBR method.

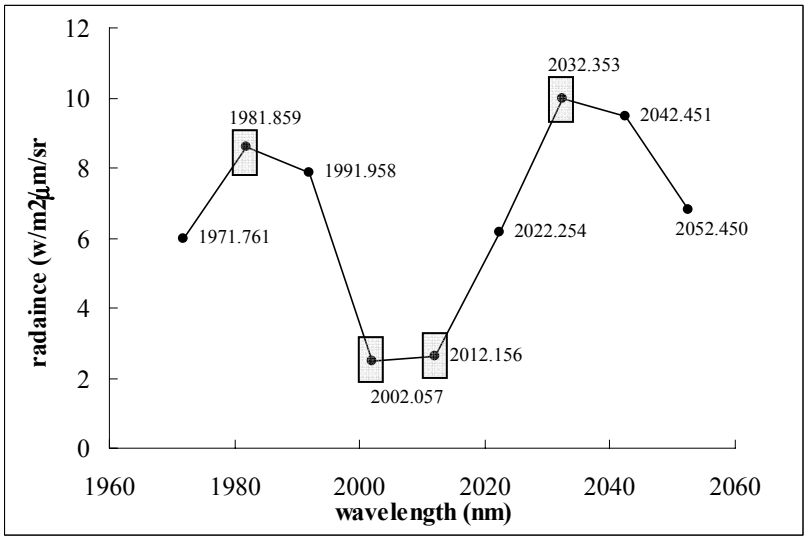

Fig.7.1: Location of measurement channel and reference channels in Hyperion sensor.

By inverting the following equation (eq. 7.1), columnar abundance of CO_2 can be retrieved.

$$CIBR = \exp\left(-\alpha[CO_2]^{\beta}\right) \tag{7.1}$$

where,
$[CO_2]$ is the CO_2 column abundance
α and β are parameters (related to the model variables)
CIBR is defined by the following equation (eq. 7.2):

$$CIBR = \frac{L_m}{w_{r1}L_{r1} + w_{r2}L_{r2}} \tag{7.2}$$

where,
L_m is the radiance of measurement channel
L_{r1} and L_{r2} the radiance of reference channels
and $w_{r1} = \dfrac{\lambda_{r2} - \lambda_m}{\lambda_{r2} - \lambda_{r1}}$
$w_{r2} = \dfrac{\lambda_m - \lambda_{r1}}{\lambda_{r2} - \lambda_{r1}}$ are weighing coefficients (λ = wavelength).

In order to obtain column abundance of CO_2, the α and β parameters were calculated. Note, that these parameters provide the calibration relationship between the CIBR and the column CO_2 content. In FASCOD radiances were calculated of four Hyperion bands (B183, B185, B186 and B188) using the atmospheric conditions as expected in the study area. The details of atmospheric profile (composition, sensor height, aerosol profile etc.) are discussed in the previous section. The spectra of different concentrations of CO_2 (300-10000 ppmv) were simulated in FASCOD and later α and β were calculated by linearly fitting an equation. The values of α and β were calculated with a fit correlation of 98%, and were retrieved for B185 and B186. By inverting the CIBR equation (eq. 7.1), the CO_2 columnar abundance was retrieved with the radiance measured on each pixel by the Hyperion sensor. The following Figures (Fig. 7.2) show the false colour composite and retrieved columnar abundance of CO_2 for B185 and B186.

Before applying the CIBR and inversion equations, the signal-to-noise ratio (SNR) of the scene was estimated. Because of low reflectance of coal and coaldust in most of the study area (except for the west part and middle) and high CO_2 concentration in the atmosphere, the Hyperion scene had an overall low radiance value. It was observed that SNR for

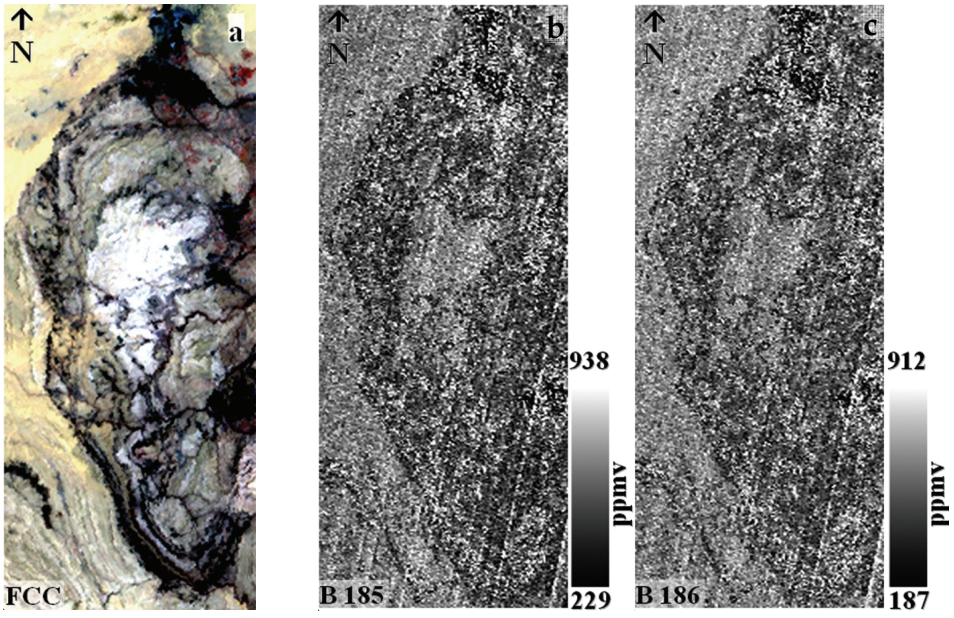

Fig. 7.2: False colour composite (a), CIBR derived CO_2 concentration (ppmv) of B185 (b) and B186 (c) in Wuda coal mining region.

both B185 and B186 were very low (~11). Although in normal cases, such a low SNR is not acceptable, but for the present study there was no other alternative due to absence of other (relatively) distinct CO_2 absorption bands in the operating range of the Hyperion sensor. As a well mixing gas, altitude has little effect on CO_2 concentration (till ~100 km). For experimental purpose an ASTER derived digital elevation model (DEM) was used to reduce the terrain effect. However, it has observed there was no significant change in the CIBR value.

It can be seen in the Fig. 7.2 that CO_2 concentration over the study area has a wide range. As the study area contains several active coalfires and coal powered industries/power-plant, it was expected that overall CO_2 concentration will be much higher than average global CO_2 concentration. In addition, few point measurements close to coalfires in the study area suggest that CO_2 concentration could be as high as 127,994 ppmv. Experienced from the field observation and chemical analysis of gas samples, it was assumed that higher temperature (coalfire, coal powered industry) = higher CO_2 emission. From visual comparison of two images and field knowledge, it was observed that in some pixels, higher CO_2 concentration (in both B185 and B186) was well correlated with thermal anomalies derived from ASTER thermal infrared data. But for the entire image there is hardly any correlation (Fig. 7.3a and 7.3b).

Another method was tested later to establish the relation between temperature increment and CO_2 concentration. The mean values of CO_2 concentration (ppmv) for a certain temperature range (increment of

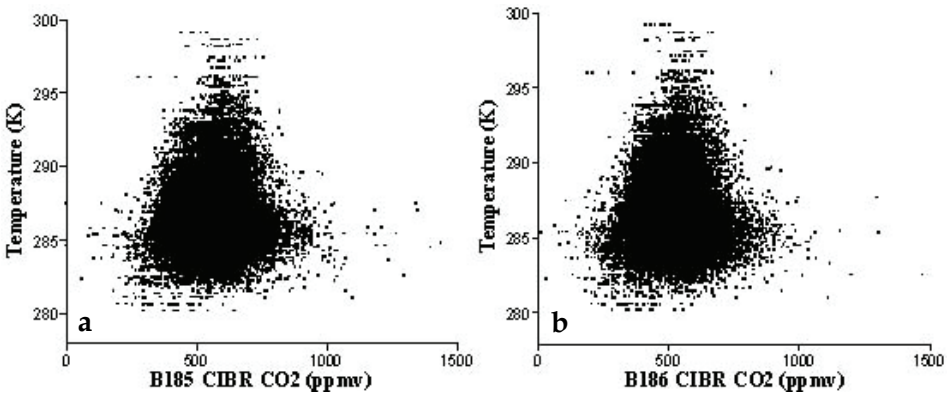

Fig. 7.3 Relation between surface temperature and CIBR derived CO_2.

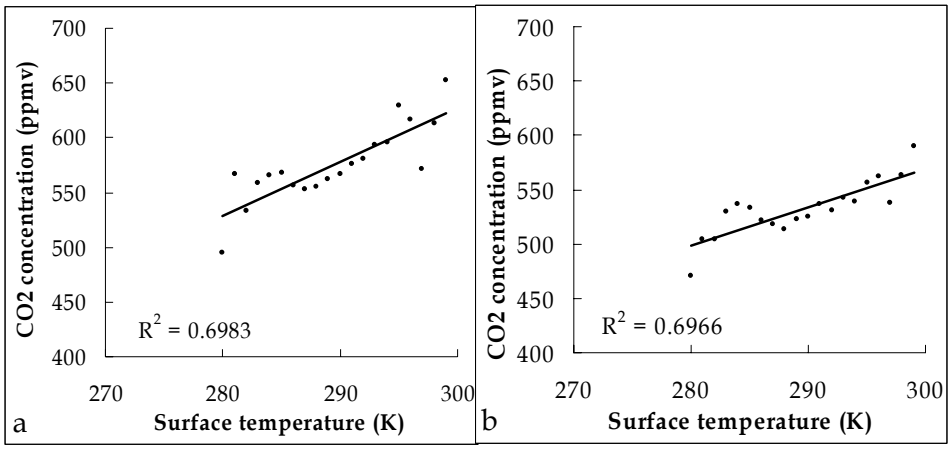

Fig. 7.4: The relation between CO_2 concentrations and temperature range of Hyperion B185 (a) and B186 (b).

every 1K) were calculated and then the relationship was tested (Fig. 7.4a and 7.4b). Furthermore, the correlation between the temperature range and mean CO_2 concentration was tested and found to be significant (Table 7.1 and 7.1).

Table 7.1: Correlation between surface temperature and CO_2 concentration (B185)

Pearson Correlation Sig. (2-tailed)	Temp- erature	Number of pixels	Range	Mean CO_2 (ppmv)
Temperature	1	-0.381	-.712**	.795**
		0.097	0.000	0.000
Number of pixels	-0.381	1	.709**	-0.054
	0.097		0.000	0.820
Range	-.712**	.709**	1	-0.342
	0.000	0.000		0.140
Mean CO_2 (ppmv)	.795**	-0.054	-0.342	1
	0.000	0.820	0.140	

**Correlation is significant at the 0.01 level (2-tailed).

Table 7.2: Correlation between surface temperature and CO_2 concentration (B186)

Pearson Correlation Sig. (2-tailed)	Temp- erature	Number of pixels	Range	Mean CO_2 (ppmv)
Temperature	1	-0.383	-.567**	.835**
		0.095	0.009	0.000
Number of pixels	-0.383	1	.605**	-0.160
	0.095		0.005	0.501
Range	-.567**	.605**	1	-0.262
	0.009	0.005		0.265
Mean CO_2 (ppmv)	.835**	-0.160	-0.262	1
	0.000	0.501	0.265	

**Correlation is significant at the 0.01 level (2-tailed).

However, for some pixels, very low or very high CO_2 concentration could be the result of sensor limitations and noise of that particular band and radiation from aerosols and Cirrus clouds. Additionally, few scan line failures can be seen in the east and south east of the both bands. Due to lack of proper field data and unsuitability of interpolation of few point measurements in the study area, a spatial relationship between B185 and B186 was tested (Fig. 7.5) that shows good correlation between the two bands.

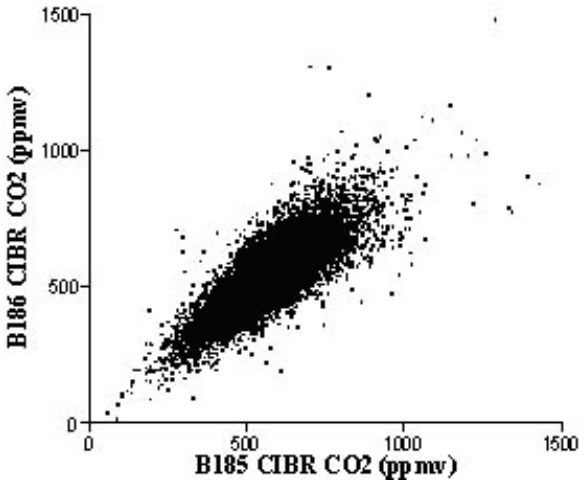

Fig. 7.5: Spatial relation between CIBR derived CO_2 (B185 and B186).

Further, a sensitivity analysis was undertaken in order to test the relationship between increment of radiance at sensor and CIBR derived CO_2 concentration over different surface types such as coalfire affected areas (south of study area), coal powered industry (south east of study area), sandstone (in the middle of study area), desert (north west of study area) and vegetation (north east of study area). It can be observed from Fig. 7.6a and 7.6b that after an increase of radiance at sensor value of B185 and CIBR, derived CO_2 follows a smooth pattern whereas B186 derived CO_2 shows an unpredictable pattern with change of radiance at sensor after increase of 75% of original value of B186.

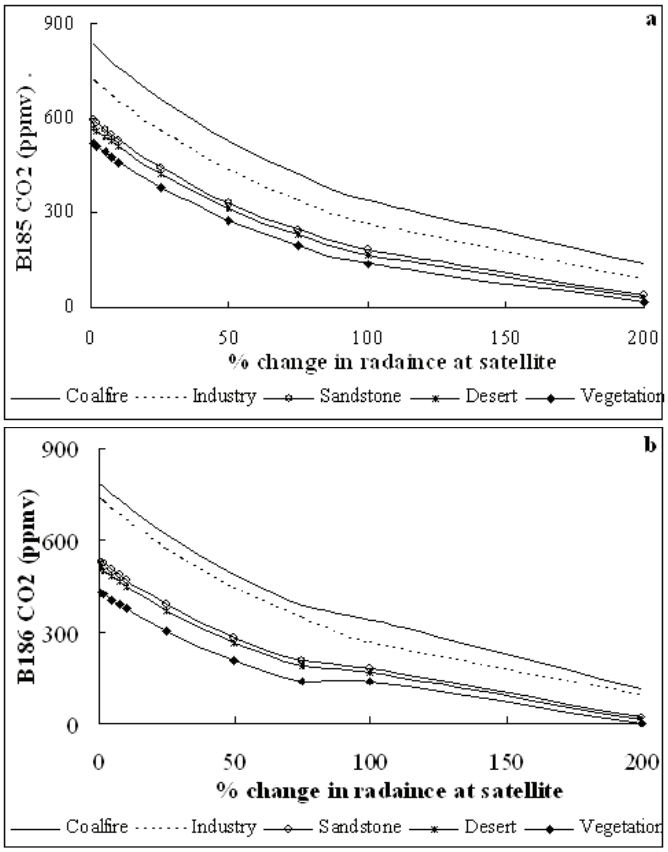

Fig. 7.6: Effect of change in radiance at satellite of B 185 (a) and B186 (b) over different surface types.

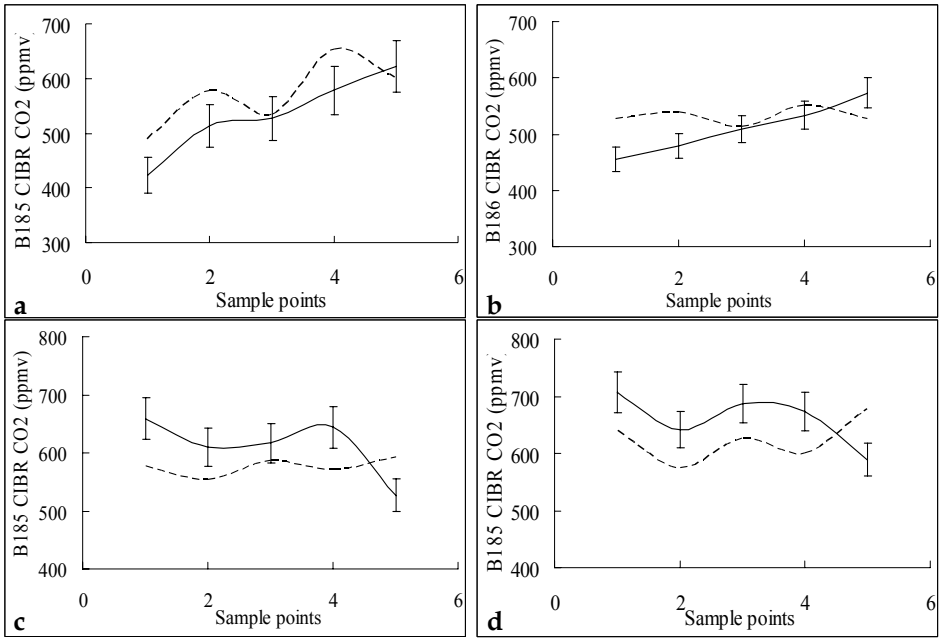

Fig. 7.7: Effect of surface reflectance on CO_2 retrieval. (a), (b) B185 and B186 values over *dark object* with known source (coalfire) of anomalous CO_2 flux with a retrieval deviation of 7.65% and 4.73% from surrounding pixels respectively. (c), (d) B185 and B186 values over *bright object* without any source of anomalous CO_2 flux with a retrieval deviation of 4.97% and 5.47% from surrounding pixels respectively. Here solid line and dashed line represent the value of central pixel and average of surrounding pixels respectively.

In order to randomly evaluate 'overestimation' and 'underestimation' due to high or low surface reflectance (ρ), some dark and bright pixels were selected and the value of central pixel was compared with the value of surrounding pixels (Fig 7.7). It was observed that in a case of low reflectance pixel (such as coal) certain pixel returns lower value (7.65% and 4.73% for B185 and B186) than average of it's immediate surrounding pixels. On the other hand high reflectance surface (such as desert sand) appears to have higher CO_2 abundance (4.97% and 5.47% for B185 and B186) than the average of neighbouring pixels.

7.6 Estimating CO_2 concentration using inversion method

The radiance at sensor is a result of absorption and scattering of surface reflected energy, energy radiated by atmosphere and TOA Solar irradiance. In FASCOD, the atmospheric layers are automatically defined by internally depending on the atmospheric model except interference from the user. For the purposes of the present research, the total atmospheric path was defined in two basic layers. The first layer was up to the height of CO_2 plume and the second layer formed the rest of the atmospheric path (up to space). A schematic diagram of proposed model is presented in Fig. 7.8. The plume height was defined as 25 m for the model as it was expected that the plume related CO_2 will be dispersed in the immediate atmosphere after a certain altitude.

In order to extract CO_2 plume radiance from radiance at satellite, different components were identified and a simplified atmospheric model was created. In the first step, surface reflectance was calculated using the following equation (eq. 7.3):

$$\rho = \frac{\pi \ L_{Sat} \ d^2}{L_{Sun} \ Cos\theta_s} \qquad (7.3)$$

where,
ρ = surface reflectance,
d = Earth-Sun distance,
θ_S = Solar zenith angle,
L_{Sat} = radiance at sensor,
L_{Sun} = Solar irradiance.
Later, surface leaving radiance was calculated (for a Lambartian surface) using equation 7.4.

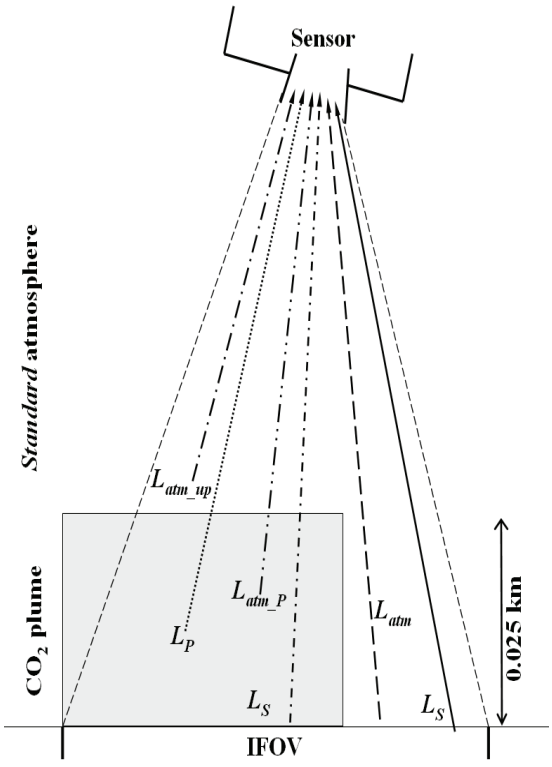

Fig. 7.8: Main components of the proposed model.

$$L_S = \frac{L_{Sun}\ \rho\ \tau_{atm}\ Cos\theta_s}{\pi} \tag{7.4}$$

where, L_S = surface leaving radiance and τ_{atm} = transmittance of atmosphere (for a Solar zenith angle 39.7 degree).

The radiance at sensor is a product of solar radiance reflected by surface (depending on surface reflectance), atmospheric radiance and solar radiance, where first two components are function of transmittance (eq. 7.5).

$$L_{Sat} = L_S + L_{atm} + L_{Sun} \tag{7.5}$$

The equation 7.5 can be extended and CO_2 plume radiance can be defined as:

$$L_P = \frac{L_{Sat} - \left(\begin{array}{l} L_S \tau_P \tau_{atm_P} \tau_{atm_{up}} + L_{atm_P} \tau_P \tau_{atm_P} \tau_{atm_{up}} \\ + L_{atm_{up}} \tau_{atm_{up}} + L_S \tau_{atm} + L_{atm} \tau_{atm} + L_{Sun} \Omega \end{array} \right)}{\tau_P \tau_{atm_P} \tau_{atm_{up}}} \tag{7.6}$$

where, L_{Sat} = radiance at sensor, L_P = radiance from CO_2 plume, L_S = surface leaving radiance L_{atm_P} = radiance from other gases excluding CO_2 (till plume height), $L_{atm_{up}}$ = radiance from rest of the atmosphere (from top of the CO_2 plume), L_{atm} = radiance from atmosphere (full path length), τ_P = transmittance of CO_2 plume, τ_{atm_P} = transmittance of other gases excluding CO_2 (till plume height), $\tau_{atm_{up}}$ = transmittance of rest of the atmosphere (from top of the CO_2 plume), τ_{atm} = transmittance of the atmosphere (full path length), L_{Sun} = Solar irradiance, Ω = solid angle (IFOV of sensor).

Finally, the relationship between CO_2 concentrations (ppmv) and CO_2 radiance was calculated from CO_2 plume radiance using a regression model.

In FASCOD, these components were calculated by using different models depending on the criteria. For all cases radiance and transmittance were calculated and resampled using Gaussian scanning/interpolating function with Half Width Half Max (HWHM) of

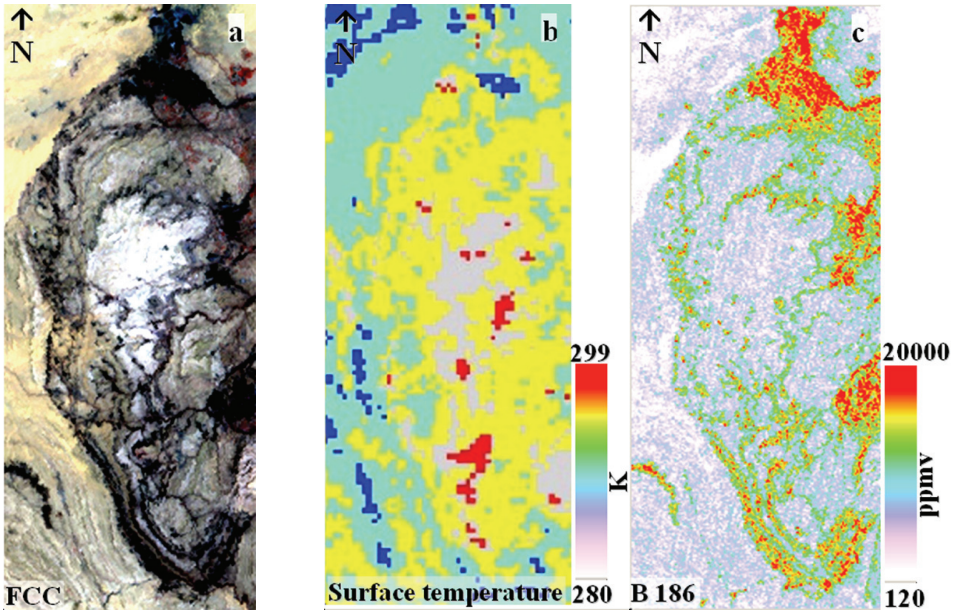

Fig. 7.9: False colour composite (a), ASTER derived surface temperature (b) and model derived CO_2 concentration (ppmv) of B185 (c) of Wuda coal mining region.

Hyperion B185 (central wavelength 2.002 µm). Later these parameters were used to obtain CO_2 plume related radiance from radiance at satellite. In relation to central wavelength and HWHM of Hyperion B185, several atmospheric models were simulated with different CO_2 concentrations (300 – 10000 ppmv) in order to establish a relationship between plume radiance and CO_2 by using a linear regression model.

The Fig. 7.9 shows false colour composite, ASTER derived surface temperature and model derived CO_2 concentration (ppmv) of B185. The red patches in the Fig. 7.9c represent highly anomalous CO_2 flux from active coalfires and industrial activities. The overall concentrations in some pixels are quite high as shown in Fig. 7.9c, as the model's plume height was defined as 25 m. It is worthwhile mentioning here that coalfire is a very local phenomena and CO_2 emitted from a coalfire can easily be dispersed in the immediate atmosphere. Strong wind flow from the nearby Gobi desert could influence the process. As a well mixing gas, CO_2 can easily dissolve with altitude in order to reach equilibrium. Another model (not shown here) with a plume height of 1 km shows a rapid 50% decrease in CO_2 concentration.

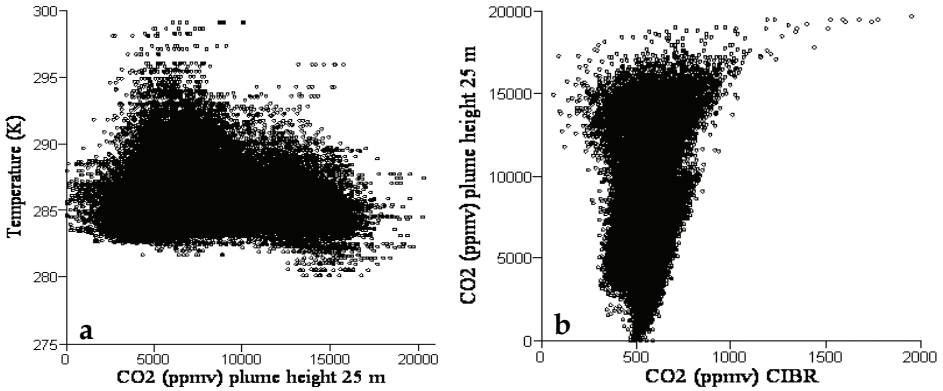

Fig. 7.10: Spatial relation between ASTER derived surface temperature and model derived CO_2 (a) and CIBR derived CO_2 concentration of B185 and model derived CO_2 (b).

Spatial relationships between surface temperature and model derived CO_2 concentration are shown in Fig. 7.10a and 7.10b. The relationship between surface temperature and CO_2 concentration shows a moderate agreement. In the north of the study area, a higher concentration of CO_2 is mostly due to coal processing plants. Also in the east, most anomalous CO_2 fluxes are related to industrial activities. The chimneys of these industries hardly appear as thermal anomalies but do emit a huge amount of CO_2 as most of these emissions form industries are untreated. The relationship between model and CIBR derived CO_2 does not show good correlation. The reason behind this disagreement could be the effect of the altitude because CIBR returns a column averaged CO_2 concentration whereas the present model deals with much smaller path length. The wind speed/direction could have a strong influence in the column averaged CO_2 retrieval.

7.7 Error contribution factors

The both methods deal with some uncertainties that can hardly be resolved. The total retrieval error is a resultant of sensor noise, surface properties, terrain effect, model error and interference for other atmospheric constituents.

Sensor noise: A better signal to noise ratio is always required to retrieve surface or atmospheric properties more effectively. According to Hyperion science team SNR in the SWIR range is 40, which is lower than required. In the study area, the SNR of B185 was found to be ~11, which

is much too low in order to retrieve any useful information. However, B185 was used in this study because of non-availability of other suitable CO_2 absorption bands.

Surface properties: As discussed in Section 7.5, most of the study area is covered by coal or coal dust. Low reflectance of the surface under consideration could include some retrieval error and leads to overestimation of CO_2 concentration. On the other hand, it was observed over a bright surface that CO2 is lower than its surrounding pixels.

Terrain effect: Low Solar zenith angle (39.7) related error or shadow effect in a rugged terrain like present study area could contribute a significant retrieval error. To reduce the terrain effect, an image normalization method was applied using the cosine of solar incidence angle. However, it was found that the method made no significant contribution to improve the CO_2 retrieval.

Model error: It should be noted that the proposed model is a simplified form of real world energy-surface-atmosphere interaction. In the real world, radiances from many more components could determine the final radiance at sensor. Particularly reflected energy from adjacent pixels depending on the incidence angle hardly could be solved. Also, the aerosol models used for this study were from LOWTRAN with a 'rural' extinction type that could be different from the study area. Because the area was near to the Gobi desert, a 'desert' extinction aerosol model was also tested, but was subsequently excluded due to poor performance. For stratospheric aerosol profile 'background stratospheric' was used. For cirrus clouds scattering calculation 'NOAA Cirrus Profile' was used with 'Cirrus Thickness' 1.0 km and 'Cirrus Base Altitude' 8.0km in FASCOD. However, it has been observed by previous researchers that the effect of the radiation scattered by thin clouds and aerosol on the estimation of the CO_2 column amount is not significant (Dufour and Bréon, 2003).

Interference of other atmospheric constituents: In the operating range of Hyperion sensor B185 is most suitable band for atmospheric CO_2 retrieval as its central wavelength is close to 2.001 μm. Nevertheless, this band is relatively transparent for other atmospheric species, as there are still some absorption features from water vapour and other gases. The water vapour columnar abundance was retrieved using CIBR method

(not shown) that shows a value range of 0.35 to 1.97 gm cm^{-2} for the same area. Because absorption features of water vapour and other atmospheric species in the same band, overestimation of CO_2 concentration can be overruled.

7.8 Conclusions

It is roughly estimated by previous researchers that coalfire has small but significant contributions to increase CO_2 concentrations in the atmosphere. Therefore, in order to avoid a major environmental catastrophe, the problem of coalfires and related CO_2 emissions needed to be addressed more seriously. In the present study, two methods were investigated in order to attempt to estimate CO_2 emission form coalfires. For atmospheric column CO_2 retrieval band ratioing method could be an effective method with necessary corrections such as removing the interference pattern of other atmospheric gases. Also a good terrain correction model can reduce the error related to sun illumination angle. The band ratioing method is much faster and effect where total atmospheric column CO_2 concentration is adequate for further analysis. To estimate CO_2 emission from coalfires, a local radiation transport model based on atmospheric simulations can be useful. As the inversion method calculates only to a certain level of atmosphere, this will be much more functional to estimate CO_2 from a particular event. The limitations of this model can be overcome by using very high spectral resolution (>1 nm), high SNR and a nadir view sensor. Also, an airborne sensor can reduce the uncertainties at higher altitude.

Chapter 8

Synthesis

8.1 Introduction

The purpose of this chapter is to summarize the prime achievements of chapters 2 to 7 discuss these results with respect to the research objectives. The core aim of the present research was to develop remote sensing based a new model to quantify CO_2 emissions from coalfires.

The objectives of the present research were:

- to use satellite derived emissivity to retrieve reliable surface temperature for a better understanding of coalfires.

- to evaluate sensitivity of present hyperspectral sensors in a changing CO_2 concentration in controlled environment.

- to evaluate capability of band ratioing method for column atmospheric CO_2 retrieval and develop an new remote sensing based model to quantify CO_2 emission from coalfires.

The following sections first discuss the achievement obtained for the objectives and then finally give recommendations to overcome constrains for further research.

8.2 The concept

For the last few decades, space borne remote sensing has proved to be an effective tool to indentify and monitor a process on earth's surface. In the present research, satellite borne multi spectral TIR data and hyperspectral SWIR data were used to identify and monitor coalfires; and quantify coalfire related CO_2 emissions.

Coalfire is a very local phenomenon and often overburden rocks and surface composition are the main deciding factors that appear a certain area (pixel) with a temperature of anomaly or background. In order to delineate coalfires from surrounding surface multispectral thermal was used. By exploiting the thermal properties of surface and using Planck's equation the coalfires were identified in a qualitative manner. Unlike previous remote sensing based coalfire studies that are based on fixed emissivity values, the present study endeavours satellite derived emissivity to identify coalfires.

A space borne sensor receives the surface reflected energy that is the summation of reflected radiance (of surface) and path radiance that are reflected, absorbed and radiated by the total atmospheric column. The absorption features of different atmospheric constituents leave their signatures in specific wavelengths. Data acquired by a suitable hyperspectral instrument records the information of surface properties and atmospheric constituents (as absorption features). The combination of a proper resolution remote sensing data, a suitable radiative transfer model and field knowledge can estimate CO_2 emission from coalfires. Nevertheless, it should be noted here the model can not resolve the uncertainties in the upper atmosphere. Furthermore, the available radiative transfer codes use inbuilt continental atmospheric model that could be different from test area. The present model does not consider these uncertainties because of lack of real-time data. The following figure (Fig. 8.1) gives an overview of the process (coalfire) and data acquisition.

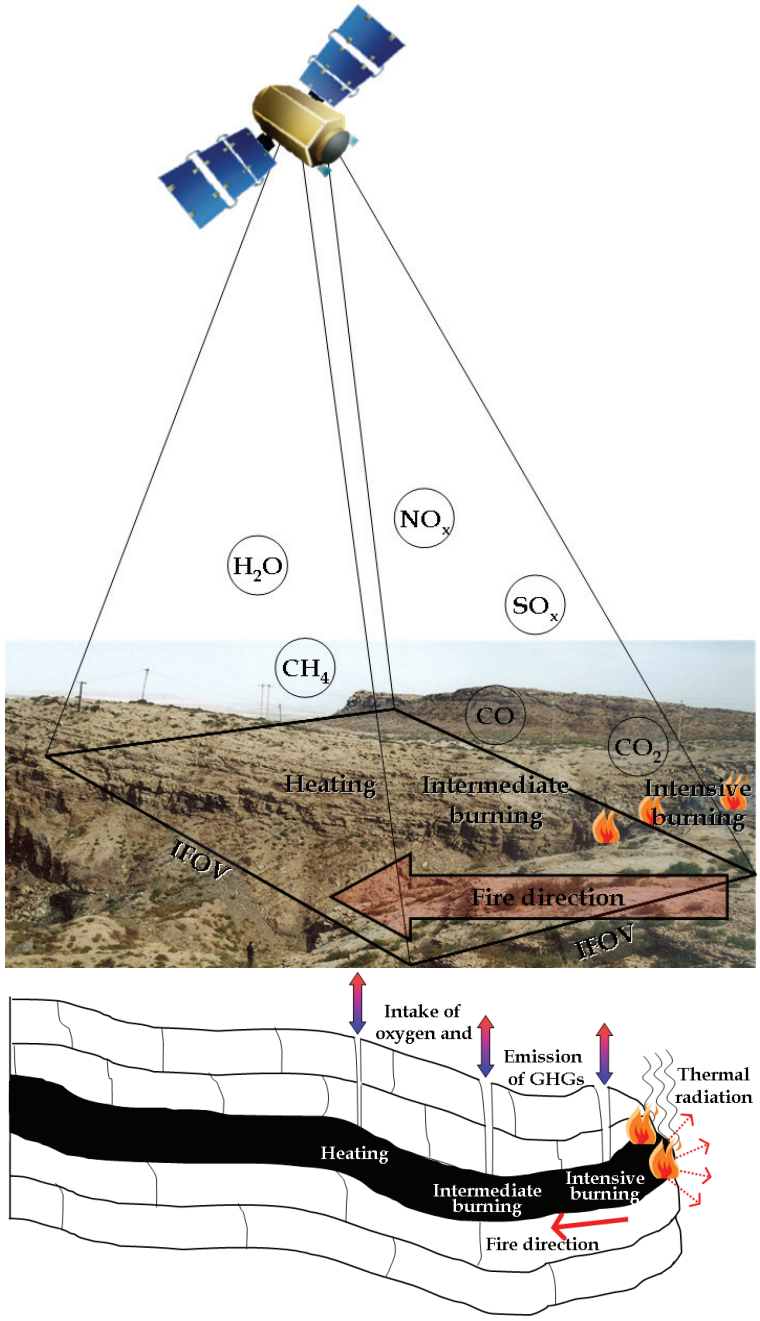

Fig. 8.1: The conceptual framework for detecting coalfirs and coalfire related CO_2 emissions using satellite borne remote sensing.

8.3 Satellite derived emissivity and coalfire detection

Emissivity is a factor as it describes how efficiently an object radiates energy compared to a blackbody. In the field of quantitative coalfire study, it is very important to estimate emissivity of the surface of interest for a better understanding of phenomena.

In chapter 4 two methods were tested (temperature-emissivity separation and vegetation index derived) to extract emissivity from satellite data. These emissivity values were later applied to extract surface temperature in the study area.

In order to extract emissivity by using temperature-emissivity separation method, two sub-methods were selected. The normalized emissivity method first calculates temperatures with a constant emissivity (0.96) for all five bands from ASTER data then choose the band with highest temperature and calculates back the emissivity for each band. For the reference channel method it is assumed that a pixel has a constant emissivity (0.95) value in the higher wavelength region (ASTER band 14, 10.9µm-11.6µm), because in this spectral region, the emissivity differences are less compared to those recorded by other ASTER channels. Then temperature calculated from band 14 was taken as the probable temperature of the surface and the emissivity values were calculated by using the relationship between surface temperature and brightness temperature.

In chapter 4, it has been discussed that from a single thermal band it not possible to extract emissivity and temperature directly. Therefore, a classified vegetation index map is useful to estimate surface emissivity. This method obtains the emissivity values from the NDVI considering three different cases, i.e. it classifies the image in three major classes: bare soil, mixture of bare soil and vegetation and mostly vegetated.

Surface property, in terms of heterogeneity of certain pixel is an important factor to calculate surface temperature precisely. In general coalfires are a very local phenomenon and in many cases they are not large enough to saturate a whole pixel in order to appear as an anomaly in comparison to the background. The aggregated temperature of a pixel depends on the location, spread, surface type and temperature of the fire/crack and its surrounding. An ASTER/TM pixel is big enough (90/120 m) to accommodate few cracks with active fire, local rocks and

(sometimes) sparse vegetation. These different types of landcover may have different temperature ranges to influence each other and finally appear as an anomaly or background with a certain pixel integrated temperature value. Also viewing angle, foot print, field of view (FOV) of sensor, distance from the object and operating range (wavelengths) between two types of sensors (handheld radiant thermometer and satellite) can introduce observation errors that are impossible to overcome.

8.4 Sensitivity analysis of hyperspectral remote sensing sensors in a changing CO_2 concentration

Coalfire related environmental problems have been discussed earlier and it has been conveyed that a proper mitigation plan needs to be enforced to avoid a major environmental disaster. The major adverse effect of coalfire is the emission of several GHGs. CO_2 is the main component of coalfire emitted gases along with CO, CH_4, SO_x and NO_x. It has been roughly estimated by researchers that CO_2 emission from Chinese coalfires could be as high as 3% of the world's total CO_2 emission from fossil fuels. In this context, estimating CO_2 emissions from coalfires is an important research problem in order to avoid major consequences such as significantly enhances the CO_2 concentration in the atmosphere that leads to global warming.

Chapter 6 describes a sensitivity analysis to study the possibilities of present hyperspectral sensors for atmospheric CO_2 retrieval in a changing noise and CO_2 concentration. For this purpose first the most susceptible CO_2 bands (in the VNIR and SWIR range) were identified that are not significantly influenced by other atmospheric constituents such as water vapour. The CO_2 absorption bands ~2.0 μm were selected for further study. It was observed these bands are interfered by several other atmospheric species that are narrow but frequent. Nevertheless, in the present spectral resolution (~10 nm) of hyperspectral sensors it was the best possibility for atmospheric CO_2 observation.

Chapter 6 also discusses the main factors (spatial/spectral resolution, scattering etc.) that can contribute a significant amount of error on CO_2 retrieval from remote sensing sensor. To retain higher SNR a sensor with larger footprint is more useful but in the other hand it increases the possibilities of heterogeneity of landcover and makes CO_2 retrieval more complicated. Although in a wider absorption window overall retrieval

error will be less, in a narrower window scattering by aerosol and the H_2O continuum can be assumed constant. Additionally in a certain sampling rate, a narrower spectrum will be acquired faster and thus less contaminated by the artefacts due to the spatial variation of surface reflectance, pressure, temperature profile, and gas abundances as the instrument's instantaneous field of view moves across the Earth. Quantitative study of CO_2 concentration estimation can be affected by aerosol and cirrus clouds. In the electromagnetic spectrum at about 2 μm most aerosols show a rapid decrease of optical thickness except for some specific cases such as dust/sand storm. In the present study area that could be a possible factor for error contribution in CO_2 quantification as it is close to the Gobi desert.

8.5 Quantifying CO_2 emissions from coalfires

The main problem of quantifying atmospheric CO_2 is non-availability of wide adsorption band to in the VNIR and near SWIR part of EMS – that are often covered by most hyperspectral remote sensing sensors. In the present study two methods were evaluated for atmospheric CO_2 retrieval in a coalfire affected area. It is worthwhile to mention here, the SNR of Hyperion band 185 was found to be very low (~11) in order to retrieve any highly useful information. Nevertheless, B185 was used in this study because of non-availability of other suitable CO_2 absorption bands.

Chapter 7 evaluates the possibilities of band rationing method to retrieve columnar CO_2 and proposes a model to retrieve CO_2 concentration emitted from coalfires to a desired altitude. The model is based on simulations in radiative transfer code and hyperspectral remote sensing data.

In the chapter 7, a radiative transfer based model has proposed the retrieval of CO_2 concentration up to a desired altitude. The basic idea of the model is to identify the different components that are responsible for the final radiance at satellite and then extract the CO_2 plume related radiance from remote sensing data. And finally make an inverse relation to retrieve CO_2 concentration from CO_2 plume related radiance by using a regression model.

8.6 Concluding remarks

Use of satellite derived emissivity for coalfire detection

It was observed between the two temperature-emissivity separation methods, normalized emissivity method is more reliable in estimating surface temperature from multispectral thermal remote sensing data like ASTER. The ASTER multispectral thermal sensor operates in 8 to 14 μm with a broad spectral coverage (~1 μm). Thus using narrow bands and more channels, satellite derived emissivity can be calculated much more precisely.

The results of vegetation index derived emissivity shows that it can estimate a more reliable surface temperature rather than use of a fixed emissivity for all types of landcover. However, it should be noted that vegetation type, water content of leaf and view angle can influence the expected result.

A comparison between ground based and satellite based observations of surface temperature is shown. From the comparison, it is clear that location, spread and temperature of a coalfire is the main deciding factor for final pixel integrated temperature.

Sensitivity analysis of present hyperspectal sensors in changing CO_2 concentration

During noise introduction, it was observed in the FASCOD simulated spectra (which are resampled based on central wavelength and FWHM) in respect to a specific sensor (AVIRIS, HYMAP, DAIS and HYPERION) that in a case of additive noise scenario all the sensors are not very much influenced. Nevertheless, in the case of multiplicative noise DAIS returned the worst scenario whereas HYPERION was more consistent.

Furthermore, same additive and multiplicative noise models were introduced to FASCOD simulated spectra (in respect to a specific sensor) with variable CO_2 concentrations (ppmv). It was observed that for additive noise on AVIRIS, HYMAP and HYPERION nearly has no effect but DIAS has little displacement with the change of CO_2 variation. For multiplicative noise AVIRIS, HYPERION and HYMAP closely agree with in next reference spectra and DAIS to a lesser extent.

Estimating CO_2 concentration from coalfires

Using a band ratioing method such as CIBR, atmospheric columnar water vapour retrieval already is a popular method. However, column atmospheric CO_2 retrieval is not as straightforward as water vapour. The CO_2 absorption bands in the VNIR and near SWIR are relative narrow and often interfered by other atmospheric constituents such as water vapour. In the present research it was observed that CIBR is capable of quantifying column atmospheric CO_2, though overestimation due to absorption features of other atmospheric gases can not be ruled out. Later the spatial relation between CIBR derived CO_2 concentration and surface temperature anomaly (due to coalfires) was tested and it was found they correlated well.

In order to assess the relationship between increment of radiance at sensor and CIBR derived CO_2 concentration over different surface types, a sensitivity analysis was undertaken over coalfire affected and non-affected areas. It was found that B185 follows a smooth pattern whereas B186 is unpredictable with the increment of radiance at satellite. To evaluate effect of surface properties on and CIBR derived CO_2 concentration randomly few *dark* and *bright* pixels were selected. The observation was: *dark* pixels can appear as relatively low concentration and *bright* pixels can appear as relatively high concentration than surrounding pixels.

It was observed that the model derived (with a plume height 25 m) CO_2 concentration is quite high because of low path length of the model. The spatial relationship between surface temperature and model derived CO_2 was moderately agreed. It was concluded that the model deals with few uncertainties that can hardly be solved in the present scenario. The present simplified model deals with most probable contributors that define radiance at satellite. Outside this model, there are many components and situations that could finalize the radiance. During simulation, few standard atmospheric properties were selected, which could be different from study area. In other words, atmospheric simulations as defined in FASCOD could be different from the local radiation transport model in terms of aerosol loading, high altitude cloud drops, wind speed/direction and standard gas composition.

8.7 Potential of future research

In the field of remote sensing based coalfire and relation emission study, the present study successfully added new contributions. However, the present research is just the beginning of remote sensing based coalfire related CO_2 studies that needs to be carried out for more accurate CO_2 retrieval.

To study coalfires quantitatively, satellite derived emissivity could be used for a better understanding of coalfires. Higher spatial resolution remote sensing data can achieve much more accurate emissivity from thermal remote sensing data and identify coalfires more effectively. Other than coalfire study, the satellite derived emissivity can be used for local lithological mapping based on the emissivity values.

As experienced from present research a high SNR data could deliver more useful information. In addition, reduction of terrain/shadow effect could return more accurate information from the area under investigation. Though the present models deals with most probable atmospheric/surface components, a further assessment of model could be useful. Inputs of radiosonde data in Fascod could represent much accurate local radiation transport model rather than continental model. In the preset situation, however, high spectral resolution data (>1 nm) are not commercially available that can reduce the overestimation due to absorption features of interfering atmospheric constituents in the CO_2 absorption bands. With a very high spectral resolution in specific wavelengths, a future sensor can attain more reliable atmospheric CO_2 retrieval. To improve the SNR ratio in high spectral resolution data a relatively larger spatial

In order to estimate the total CO_2 emissions from Chinese coalfires, it would be necessary to use both remote sensing as well as local field based methods (using a flux chamber).

The CO_2 flux could be estimated from a certain vent by using a flux chamber and the following equation

$$Q = \frac{dc}{dt}\frac{V_c}{A_c} = \frac{dc}{dt}h_c$$

where d_c/d_t is the concentration increase over time, h_C height of the chamber and V_C, A_C volume and base area of the chamber respectively. The unit of the gas flow Q is [Mass][Area]$^{-2}$[Time]$^{-1}$. The estimated CO_2

flux can be interpolated over the total coalfire affected area to have a rough estimation of the total CO_2 emission from a certain area. However, the many uncertainties related to local geological setting and meteorological conditions can not be overcome.

If these sparse ground-based local point observations are combined with remote sensing data in a model, we can estimate the CO_2 concentration of a certain area for a better quantification of total CO_2 emissions from coalfires. For example, hyperspectral remote sensing data of the area of interest with a specific spectral resolution can be used. With an improved radiative transfer based model and hyperspectral remote sensing data, CO_2 concentration of the area can be estimated. Ideally realtime measurement by using a flux chambers would locally quantify the CO_2 concentration at the remote sensing data acquisition time. The satellite derived CO_2 concentration can be compared with initial concentration value of flux chamber and be calibrated. However, the large variability and irregularities in local vents as well as local meteorological conditions will be very difficult to overcome.

Appendix

A.1 Instrument information

A general overview of Hyperion instrument, performance and bands of interest are shown here.

Table A.1: Characteristics of the Hyperion System.

Parameter	Value
Frame Rate (Hz)	223.4
Digitization	12
Number of Spectral Bands	220
Spectral Resolution (nm)	10
Wavelength Range (nm)	400 – 2500
Cross track FOV (deg)	0.63
IFOV (mrad)	0.043
Aperture (cm)	12
Average Power (W)	51
Mass (kg)	49
Volume (L x W x H, cm)	39 x 75 x 66

Table A.2: On-orbit Performance of the Hyperion Instrument.

	Characteristic	On-orbit
Optical	GSD (m)	30.38
	Swath (km)	7.6
	VNIR MTF @ 630nm	0.23-0.27
	SWIR MTF @ 1650nm	0.28
	Spatial Co-Reg: VNIR	.18 @ Pix #126
	Spatial Co-Reg: SWIR	.21 @ Pix #131
Radiometric	Abs. Radiometry (1Sigma)	3.40%
	VNIR SNR (550-700nm)	140-190
	SWIR SNR (~1225nm)	96
	SWIR SNR (~2125nm)	38
Spectral	No. of Spectral Channels	198 Processed
	VNIR (bands 8-57)	427-925 nm
	VNIR Bandwidth (nm)	10.19-10.21
	VNIR X-trk Spec. Error	2.2 nm
	SWIR (bands 77-224)	912 - 2395 nm
	SWIR Bandwidth (nm) 1	0.08-10.09
	SWIR X-trk Spec. Error	0.58

Table A.3: Characteristics of Hyperion bands of interest.

Hyperion Band	Average Wavelength (nm)	Full Width at Half the Maximum FWHM (nm)	Spatial Resolution (m)
B183	1981.8600	10.9230	30
B185	2002.0600	10.9083	30
B186	2012.1500	10.9069	30
B188	2032.3500	10.9013	30

A.2 IDL code used in Chapter 5*

```
FUNCTION COALFIRE_INIT,filename

 ; pre-define string variables
 data = strarr(17)

 ; open ascii file
 OPENR,lun,filename,/GET_LUN

 FOR i = 0,15 DO BEGIN
  dummy = ''
  READF,lun,dummy
  dummy = STRCOMPRESS( (STRSPLIT( dummy,";",/EXTRACT) )[0],/REMOVE_ALL)
  data[i] = dummy
 ENDFOR

 ; close ascii file
 CLOSE,lun

 ; return structure with all data
 RETURN, CREATE_STRUCT($
  'filename1',data[0], $
  'filename2',data[1], $
  'filename3',data[2], $
  'x',fix(data[3]), $
  'y',fix(data[4]), $
  'default_speed',float(data[5]),$
  'influence_cracks',float(data[6]),$
  'influence_geology1',float(data[7]),$
  'influence_geology2',float(data[8]),$
  'influence_geology3',float(data[9]),$
  'influence_geology4',float(data[10]),$
  'influence_geology5',float(data[11]),$
  'year',fix(data[12]), $
  'nyears',fix(data[13]),$
  'verbose',byte(data[14]), $
  'delay',float(data[15]) )

END

;+
; function coalfire_run
;-

FUNCTION COALFIRE_RUN,fuelmap_org,init,ns,nl
```

* This IDL code has written by Dr. Harald van der Werff, ESA Departmrnt, ITC

```
  ; some definitions for printing output
  tab = STRING(9b)
  cr  = STRING(10b)
  PRINT, 'Running the model...',cr

  ; make backup copy of the fuelmap
  fuelmap = fuelmap_org

  ; define a firemap with an initial fire
  firemap = BYTARR(ns,nl,init.nyears)
  firemap[init.x,init.y] = 2b

  ; display the fuelmap, firemap and the updating fuelmap
  ; scale to a default window size (300 px max)
  scaling = CEIL(300./MAX([ns,nl]))
  xsize = ns*scaling
  ysize = nl*scaling
  DEVICE,DECOMPOSED=0
  LOADCT,3
  WINDOW,0,TITLE='Original fuel',
XSIZE=xsize,YSIZE=ysize,XPOS=0,YPOS=0,RETAIN=2
  WINDOW,1,TITLE='Remaining
Fuel',XSIZE=xsize,YSIZE=ysize,XPOS=xsize+12,YPOS=0,RETAIN=2
  WINDOW,2,TITLE='Active Fires',
XSIZE=xsize,YSIZE=ysize,XPOS=xsize*2+24,YPOS=0,RETAIN=2
  WSET, 0 & TV,REBIN(fuelmap*10,xsize,ysize)

  ; loop through the years....
  FOR year = 0,init.nyears-2 DO BEGIN

    WSET, 2 & TV,REBIN(firemap[*,*,year]*128,xsize,ysize)
    WSET, 1 & TV,REBIN(fuelmap*10,xsize,ysize)
    WAIT, init.delay

    ; find all fires
    fires = WHERE(firemap[*,*,year] EQ 2b, nfires)
    IF init.verbose THEN BEGIN
      PRINT, cr,'running year    : ', STRCOMPRESS(STRING(year+init.year))
      PRINT,    'number of fires : ', STRCOMPRESS(STRING(nfires))
    ENDIF

    ; loop through all fires
    IF nfires GE 1 THEN BEGIN
      fires = ARRAY_INDICES(fuelmap,fires)
      FOR f = 0, nfires-1 DO BEGIN

        ; get coordinates of a fire
        xf = fires[0,f]
             yf = fires[1,f]
```

```
            IF init.verbose THEN BEGIN
              PRINT, cr,tab,'fire'
              PRINT, tab,tab,'index  : ', $
                STRCOMPRESS(STRING(f))
              PRINT, tab,tab,'pixels : ', $
                STRCOMPRESS(STRING(xf)),',',STRCOMPRESS(STRING(yf))
              PRINT, tab,tab,'fuel   : ', $
                STRCOMPRESS(STRING(fuelmap[xf,yf]))
      ENDIF
            ; define area of influence
            ff = round(fuelmap[xf,yf]/init.default_speed)
            ; mark existing fire as burned out
      fuelmap[xf,yf] = 0.
            firemap[xf,yf,year+1:*] = 1b

      ; make sure that we do not probe outside the image array
            IF xf-ff GE 0 && xf+ff LT ns && yf-ff GE 0 && yf+ff LT nl THEN BEGIN

              ; get fire neighbours that have fuel
              IF init.verbose THEN BEGIN
                PRINT, tab,'neighbour'
                PRINT, tab,tab, 'map    : ', cr, $
                  [ replicate(tab,3,ff*2+1),STRCOMPRESS(STRING(fuelmap[xf-ff:xf+ff,yf-
ff:yf+ff])) ]
              ENDIF
              neighbours = WHERE(fuelmap[xf-ff:xf+ff,yf-ff:yf+ff] GT 0, nneighbours)
        IF nneighbours GE 1 THEN BEGIN
          neighbours = ARRAY_INDICES(BYTARR(2*ff+1,2*ff+1),neighbours)
          neighbours[0,*] += xf-ff
          neighbours[1,*] += yf-ff

              ; spread the fire to the neighbours
          FOR n = 0, nneighbours-1 DO BEGIN
                xn = neighbours[0,n]
                yn = neighbours[1,n]
            IF init.verbose THEN BEGIN
                    PRINT, tab,tab,'pixel  : ', $
                      STRCOMPRESS(STRING(xn)),',',STRCOMPRESS(STRING(yn))
                    PRINT, tab,tab,'fuel   : ', $
                      STRCOMPRESS(STRING(fuelmap[xn,yn]))
            ENDIF
                firemap[xn,yn,year+1] = 2b
          ENDFOR
        ENDIF
            ENDIF
      ENDFOR
    ; speed up the processing when no more fires are detected
    ENDIF ELSE init.delay = 0
  ENDFOR
```

```
  ; display final images
  WSET, 1 & TV,REBIN(fuelmap*10,xsize,ysize)
  WSET, 2 & TV,REBIN(firemap[*,*,year]*128,xsize,ysize)

  PRINT, cr,'Done!',cr

  RETURN, firemap

END

;+
; function coalfire_fuel
;-

FUNCTION COALFIRE_FUEL,layer_seams,layer_cracks,layer_geology,init,ns,nl

  ; define a fuelmap with a default speed of fire
  ;fuelmap = REPLICATE(FLOAT(init.default_speed),ns,nl)

  ; set influence of coal seams and their dip (binary)
  ;index = WHERE(layer_seams EQ 0)
  ;fuelmap[index] = 0.

  ; define a fuelmap with a default speed of fire (floating point)
  fuelmap = layer_seams * init.default_speed

  ; set influence of geology
  IF init.filename3 THEN BEGIN
    index = WHERE(layer_geology EQ 1)
    fuelmap[index] *= init.influence_geology1
    index = WHERE(layer_geology EQ 2)
    fuelmap[index] *= init.influence_geology2
    index = WHERE(layer_geology EQ 3)
    fuelmap[index] *= init.influence_geology3
    index = WHERE(layer_geology EQ 4)
    fuelmap[index] *= init.influence_geology4
    index = WHERE(layer_geology EQ 5)
    fuelmap[index] *= init.influence_geology5
  ENDIF

  ; set influence of cracks
  IF init.filename2 NE "" THEN BEGIN
    index = WHERE(layer_cracks EQ 1)
    fuelmap[index] *= init.influence_cracks
  ENDIF

  RETURN, fuelmap

END
```

```
;+
; pro coalfire
;
; main program
;-

PRO COALFIRE

 filename = DIALOG_PICKFILE(/READ,DEFAULT_EXTENSION='ini',$
  /MUST_EXIST,TITLE='Load initialisation file',GET_PATH=path)
 IF filename EQ "" THEN RETURN
 init = COALFIRE_INIT(filename)

 ; some definitions for printing output
 tab = STRING(9b)
 cr  = STRING(10b)
 PRINT, cr, 'loaded init file: ',cr,tab,filename
 PRINT, cr, 'loaded layers: '

 ; load layer with coalseams
 PRINT, tab, init.filename1
 layer_seams = READ_TIFF(path+PATH_SEP()+init.filename1,GEOTIFF=geotiff)

 ; load layer with fractures
 IF init.filename2 NE "" THEN BEGIN
  PRINT, tab, init.filename2
  layer_cracks = READ_TIFF(path+PATH_SEP()+init.filename2)
 ENDIF

 ; load layer with geology
 IF init.filename3 NE "" THEN BEGIN
  PRINT, tab, init.filename3
  layer_geology = READ_TIFF(path+PATH_SEP()+init.filename3)
 ENDIF

 PRINT, cr

 ; determine size of the images
 ns = N_ELEMENTS(layer_seams[*,0])
 nl = N_ELEMENTS(layer_seams[0,*])

 ; prepare the fuel
 fuelmap = COALFIRE_FUEL(layer_seams,layer_cracks,layer_geology,init,ns,nl)

 ; run the model
 firemap = COALFIRE_RUN(fuelmap,init,ns,nl)

 ; option to save output images to disk
 ok = DIALOG_MESSAGE('Save output to disk?',/QUESTION,/CENTER)
```

```
  IF ok EQ 'Yes' THEN BEGIN
    firemap = FLOAT(firemap)
    firemap = [ [[firemap]],[[fuelmap]] ]
    filename = DIALOG_PICKFILE(/WRITE,PATH=path)
    IF filename NE "" THEN BEGIN
      firemap = TRANSPOSE(firemap, [2, 0, 1])
      WRITE_TIFF,filename,firemap,GEOTIFF=geotiff,/FLOAT
    ENDIF
    PRINT, cr,'Saved! Bye bye...'
  ENDIF ELSE PRINT, STRING(10b),'Exiting...'

  ; close windows
  WDELETE,0,1,2

END
```

Bibliography

Abbott, W.E., 1918, Mount Wingen and the Wingen Coal Measures, Angus and Robertson, Sydney, N.S.W. Australia, 26 p.

Andres, R.J., Fielding, D.J., Marland, G., Boden, T.A., Kumar, N. and Kearney, A.T., 1999, Carbon dioxide emissions from fossil-fuel use, 1751-1950, Tellus, 51B: 759-765.

Anonymous, 1972, The Burning Mountain, Wingen, Scone Shire Council Archive.

Arisoy, A. and Akgun, F., 1994, Modelling of spontaneous combustion of coal with moisture content included, Fuel, 73(2): 281-286.

Associated Press Newswires (APN), 2005, Coal mine fire in northern Norway could burn for weeks: 2 August 2005, The Associated Press.

Austin American-Statesman (AAS), 1989, Coal mine fire in Serbia kills 92 workers: 19 November 1989, Austin American-Statesman.

Banerjee, S.C., 1985, Spontaneous combustion of coal and mine fires: A.A. Balekema, Rotterdam, 18 p.

Becker, F., 1980, In Remote Sensing Applications in Agriculture and Hydrology (G. Fraysse, Ed.), Balkema.

Bhattacharya, A., Reddy, C.S. and Mukherjee, T., 1991, Multi-tier remote sensing data analysis for coalfire mapping in Jharia coalfield of Bihar, India, in Proceedings, Asian Conference on Remote

Sensing, Singapore, 12th, National University of Singapore, p. 22-1-22-6.

Blanford, W.M., 1861, 'On the geological structures and relation of the Raniganj coalfield, Bengal', Memoirs of the Geographical Survey of India, Vol. 8, Part I.

Bruegge, C. J., Conel, J. E., Margolis, J. S., et al. 1990. In-situ atmospheric water-vapor retrieval in support of AVIRIS validation. Imaging Spectroscopy of the Terrestrial Environment: SPIE 1298, 150 – 163.

Buchwitz, M. SCIAMACHY CO2 retrievals. Oral presentation, EVERGREEN final workshop, 19-20 January 2006, KNMI, De Bilt, The Netherlands.

Buehler, S.A., Eriksson, P., Kuhn, T., von Engeln, A., and Verdes, C., 2005, ARTS, the Atmospheric Radiative Transfer Simulator, Journal of Quantitative Spectroscopy and Radiative Transfer, 91(1): 65–93.

Bunny, M.R., 1967, The Burning Mountain, Wingen: N.S.W. Geol. Survey Report, GS1967/063.

Bustin, R.M. and Mathews, W.H., 1982, In situ gasification of coal, a natural example: history, petrology, and mechanics of combustion, Canadian Journal of Earth Sciences, 19: 514-23.

Bustin, R.M. and Mathews, W.H., 1985, In situ gasification of coal, a natural example: additional data on the Aldridge Creek coalfire, southeastern British Columbia, Canadian Journal of Earth Sciences, 22: 1858-64.

Carrere, V. and J.E. Conel 1993. Recovery of Atmospheric Water vapour Total Column Abundance from Imaging Spectrometer data around 940nm – Sensitivity Analysis and Application to AVIRIS data,. Remote Sensing of Environment 44, 179 - 204.

Carrere, V. and J.E. Conel 1993. Recovery of Atmospheric Water vapour Total Column Abundance from Imaging Spectrometer data around 940nm – Sensitivity Analysis and Application to AVIRIS data. Remote Sensing for Environment 44, 179 - 204.

Cassells, J.S.C., 1998, Thermal modelling of underground coalfires in northern China, [PhD Thesis]: Enschede, ITC, 183 p.

Central Mine Planning and Design India Limited (CMPDIL), 1992, Annual Report, Central Mine Planning & Design Institute Limited, Asansol.

Chahine, M.T., 1970, Inverse problems in radiative transfer: determination of atmospheric parameters, Journal of Atmospheric Science, 27: 960–967.

Chen, L., 1997, Subsidence assessment in the Ruqigou coalfield, Ningxia, China, using a geomorphological approach. Master thesis at the International Institute for Aerial Survey and Earth Sciences (130pp). ITC, Enschede, Netherlands.

Ciais, P., Tans, P.P., Trolier, M., White, J.W.C. and Francey, R.J., 1995, A large northern-hemisphere terrestrial CO_2 sink indicated by the 13C/12C ratio of atmospheric CO_2, Science, 269: 1098–1102.

Clough, S.A., Kneizys, F., Shettle, E.P., Anderson, G., 1986, Atmospheric radiance and transmittance: Fascod. Proceedings of Sixth Conference on Atmospheric Radiation, Williamsburg, VA 1986; p. 141-144.

Conway, T.J., Tans P.P., Waterman, L.S. and Thoning, K.W., Evidence for interannual variability of the carbon cycle from the National Oceanic and Atmospheric Administration Climate Monitoring and Diagnostics Laboratory Global Air Sampling Network, Journal of Geophysical Research, 99: 22831–22855.

Cracknell, A.P. and Mansor, S.B., 1992. Detection off sub-surface coalfires using Landsat Thematic Mapper data. International Archive of Photogrammetry and Remote Sensing, 29(b7): 750-753.

Dai, S., Ren, D., Tang, Y., Shao, L. and Li, S., 2002, Distribution, isotopic variation and origin of sulfur in coals in the Wuda coalfield, Inner Mongolia, China, International Journal of Coal Geology, 51: 237–250.

Dash, P., Gfttsche, F. -M., Olesen, F. -S., and Fischer, H., 2005, Separating surface emissivity and temperature using two-channel spectral indices and emissivity composites and comparison with a vegetation fraction method, Remote Sensing of Environment, 96: 1–17.

Dufour, E. and Bréon, F-M, 2003, Spaceborne Estimate of Atmospheric CO_2 Column by Use of the Differential Absorption Method: Error Analysis, Applied Optics, 42: 3595-3609.

Dymond, J.R., and Shepherd, J.D., 1999, Correction of the topographic effect in remote sensing. IEEE Transactions of Geoscience and Remote Sensing, 37: 2618–2620.

Eastern Coalfield Limited (ECL), 2004, Annual Report, Sanktoria: ECL Eastern Coalfields Limited.

Ellyett, C.D. and Fleming, A.W., 1974, Thermal infrared imagery of the Burning Mountain coalfire. Remote Sensing of Environment, 3: 79-86.

Energy Information Administration (EIA 1), 2006, Greenhouse Gases, Climate Change, and Energy, (http://www.eia.doe.gov/oiaf/1605/ggccebro/chapter1.html).

Energy Information Administration (EIA 2), 2006: International Energy Outlook (http://www.eia.doe.gov/oiaf/ieo/coal.html).

Energy Sector Management Assistance Programme (ESMAP), 2004, Toward a Sustainable Coal Sector in China (http://wbln0018.worldbank.org/esmap/).

Enting, I.G., Trudinger, C.M. and Francey, R.J., 1995, A synthesis inversion of the concentration and $\delta^{13}C$ of atmospheric CO_2. Tellus-B, 47: 35–52.

Etheridge, D.M., Steele, L.P., Langenfelds, R.L., Francey, R.J., Barnola, J.M., and Morgan, V.I., 1996, Natural and anthropogenic changes in atmospheric CO_2 over the last 1000 years from air in Antarctic ice and firn, Journal of Geophysical Research, 101: 4115-4128.

Fisher, W.J. and Knuth, W.M., 1968, Detection and delineation of subsurface coalfires by aerial infrared scanning: Geological Society of America Bulletin, 115: 67–68.

Fleming, A.W., 1972, Investigations into Permian Geology and The Burning Mountain Coalfire [B.Sc. Thesis]: Newcastle, University of Newcastle.

Gaffey, S.J., McFadden, L,A,, Nash, D. and Pieters, C.M., 1993, Ultraviolet, visible, and near-infrared reflectance spectroscopy: laboratory spectra of geologic materials, In Pieter CM, Engler PA, editors. Remote Geochemical Analysis: Elemental and Mineralogical Composition, Cambridge: Cambridge University Press, p. 43-71.

Gangopadhyay, P.K., 2000, Surface Temperature Mapping and Detection of Surface & Subsurface Coal-mine Fires of the Raniganj Coalbelt (West Bengal) Using Remote Sensing and GIS [Dissertation Paper]: Dehradun, IIRS, p. 56.

Gangopadhyay, P.K., 2003, Coalfire detection and monitoring in Northern China: A multi-spectral and multi-sensor TIR approach [M.Sc. Thesis]: Enschede, ITC, p. 72.

Gangopadhyay, P.K., Lahiri-Dutt, K., Saha, K., 2006, Application of Remote Sensing to Identify Coalfires in the Raniganj Coalbelt,

India. International Journal of Applied Earth Observation and Geoinformation, 8: 188–195.

Gangopadhyay, P.K., Maathuis, B. and van Dijk P., 2005a, ASTER derived emissivity and coalfire related surface temperature anomaly: A case study in Wuda, North China, International Journal of Remote Sensing, 26(24): 5555-5751.

Gangopadhyay, P.K., van der Meer, F.D. and van Dijk, P.M., 2005b, Atmospheric modelling using high resolution radiative transfer codes and identification of CO2 absorption bands to estimate coalfire related emissions, in Zagajewski, B. and Sobczak, M. eds., Imaging Spectroscopy: New Quality in Environmental Studies, Warsaw University, p. 373-381.

Gao, B.C. and Goetz, A.F.H., 1990, Column Atmospheric Water Vapor and Vegetation Liquid Water Retrievals From Airborne Imaging Spectrometer Data. Journal of Geophysical Research, 95: 3549-3564.

Gee, E.R., 1932, Memoirs of the Geological Survey of India, The geology and coal resources of the Raniganj Coalfield, Part – I. (Gee, I.B.).

Geissinger, J., 1990, Mapping Underground mine fires: The case of Centralia, Pennsylvania, The Pennsylvania Geographer, 28(2): 22-26.

Geological Survey of India (GSI), 2004, Coal Resource Scenario of India (http://www.gsi.gov.in/indiacol.pdf).

Ghosh, A., 1990, Environmental Impact of Coal Mining in Eastern India, in Joshi S.C. and Bhattacharya G. (Eds.). Mining and Environment in India, H. R. Publishers, Nainital.

Ghosh. A., 1988, Environmental Impact of Coal Mining in Eastern India in Joshi S.C. and Bhattacharya G. (Eds.). Mining and Environment in India, Nainital: H R Publishers.

Gillespie, A.R., 1985, Lithologic mapping of silicate rocks using TIMS, The TIMS data users' Workshop, June 18-19, 1985, JPL Publication, 86-38, pp. 29-44.

Gillespie, A.R., Rokugawa, S., Hook, S., Matsunaga, T. and Kahle, A.B., 1998, A temperature and emissivity separation algorithm for Advanced Spaceborne Thermal Emission and Reflection Radiometer (ASTER) images, IEEE Transactions of Geosciences and Remote Sensing, 36: 1113–1126.

Glover, L., 1998, Underground Mine Fires Sparks Residents' Fear: Tribune Review, Greensburg, PA, A-1, A-10.

Goddard Space Flight Center, 2006, Global, Regional, and National Carbon Dioxide (CO2) Emission Estimates (1751-2000) from CDIAC, (http://gcmd.nasa.gov/records/GCMD_CDIAC_CO2_EMISS_MODERN.html).

Goldammer, J.G. and Seibert, B., 1989, Natural rain forest fires in Eastern Borneo during the Pleistocene and Holocene, Naturwissenschaften, 76: 518-520.

Government of India (GOI), 1979, Report of the Committee on Safety in Coal Mines, Department of Coal, GOI, New Delhi.

Green, R.O., Carre`re, V., and Conel, J.E. 1989. Measurement of atmospheric water vapor using the Airborne Visible/Infrared Imaging Spectrometer. Workshop Imaging Processing: Sparks 1989, Nevada, USA, p. 6.

Greene, G.W., Moxham, R.M. and Harvey, A.H., 1969, Aerial infrared surveys and borehole temperature measurements of coal mine fires in Pennsylvania, Proceedings of the Sixth International ERIM Symposium on Remote Sensing of Environment, 13-16 October, 1969 (University of Michigan), p. 517-525.

Gurney, K.R., et al., 2002, Towards robust regional estimates of CO2 sources and sinks using atmospheric transport models, Nature, 415: 626–630.

Hogerheijde, M.R. and van der Tak, F.F.S., 2000., Astrology and Astrophysics, 362: 697-710.

Hook, S.J., Gabell, A.R., Green, A.A. and Kealy, P.S., 1992, A Comparison of Techniques for Extracting Emissivity Information from Thermal Infrared Data for Geologic Studies, Remote Sensing of Environment, 42: 123-135.

Huang, Y., Huang, H. and Chen, W., 1991, Remote sensing approaches for underground coalfire detection, in Proceedings, Beijing International Conference on Reducing Geological Hazards, Beijing, p. 634-641.

Hunag, J., Bruuining, J. and Wolf, K.-HA.A., 2001, Modelling of gas flow and temperature fields in underground coal fires, Fire Safety Journal, 36: 477-489.

Hunter, W.W., 1868, Annals of Rural Bengal, Smith, Elder and Co., London (Reprinted by Government of West Bengal, Calcutta, 1973).

Interfax News Bulletin, 2002, Coal Mine Fire in Ukraine Kills 33 - GOVT.: 8 July 2002, Interfax International Ltd.

Interfax News Bulletin, 2004, 11 Injured in Coal Mine Fire in Kuzbass: 9 June 2004, Interfax Information Services, B.V.

Kaufman, Y. J., and Gao, B.C., 1992, Remote sensing of water vapor in the near IR from EOS/MODIS. IEEE Transactions of Geosciences and Remote Sensing, 30(5): 871–884.

Kaufman, Y. J., and Gao, B.C., 1992. Remote sensing of water vapor in the near IR from EOS/MODIS. IEEE Transactions of Geosciences and Remote Sensing, 30(5): 871–884.

Kealy, P.S. and Gabell, A.R., 1990, Estimation of Emissivity and Temperature using Alpha Coefficients, 2nd TIMS Workshop, (JPL Publication), p. 90-55.

Kealy, P.S. and Hook, S.J., 1993, Separating Temperature and Emissivity in Thermal Infrared Multispectral Scanner Data: Implication for Recovering Land Surface Temperatures, Geosciences in Remote Sensing, 31(6): 1155-1164.

Keeling, C.D. and Whorf, T.P., 1999, Atmospheric CO2 records from sites in the SIO air sampling network, University of California, California (http://cdiac.esd.ornl.gov/trends/CO2/sio-mlo.htm).

Kneizys, F.X., Abreu, L.W, Anderson, G.P., Chetwynd, J.H., Shettle, E.P., Berk, A. Bernstein, L.S., Robertson, D.C., Acharaya, P., Rothmann, L.S., Selby, J.E.A., Gallery, W.O. and Clough, S.A., 1996, The MODTRAN 2/3 Report and LOWTRAN 7 Model. Technical Report, MA 01731-3010. Phillips Laboratory, Hanscom AFB.

Knuth, W.M., 1968, Using an airborne infrared imaging system to locate subsurface coalfires, in Culm banks. Proceedings of Pennsylvania Academy of Science, Pennsylvania, p. 42.

Kok, A., 1981, Spontaneous heating of Coal, KEMA Report, WSK/2780-55 (in Dutch).

Krishnaswamy, S., Agarwal, P.K. and Gunn, R.D., 1996, Low temperature oxidation of coal 3. Modelling spontaneous combustion in coal stockpiles, Fuel, 75(3): 353-362.

Lahiri-Dutt, K., 1999, State, market and the crisis in coalbelt, Economical and Political Weekly, 34(41): 2952-2956.

Lahiri-Dutt, K., 2001, 'Location, extent and means of control of surface and subsurface mines fires in the Raniganj coalbelt of West Bengal with the help of satellite data', Research project sponsored by the University Grants Commission, Government of India, Technical Report, Department of Geography, The University of Burdwan, Burdwan.

LaRocca, A.J. and Turner, R.E., 1975, Atmospheric Transmittance and Radiance: Methods of Calculation, State-of-the-Art Report, 0014-73-A-0321 -OO02 and O014-74-C-0285, Environmental Research Institute of Michigan, Ann Arbor, MI, 1975.

Li-ding, C., 1999, Environmental problems in a coal mining area affected by coal fires -A case study in Ruqigou Coalfield, Ningxia, China, Environmental Sciences, 11(1): 23-32.

Lillesand, T.M. and Kiefer, R.W, 2000, Remote Sensing and Image Interpretation, John Wiley and Sons Inc., New York, 724 p.

Liner, R.T., 1969, Moment and Discrete Ordinate Methods in Radiative Transfer Problems, Journal of Quantitative Spectroscopy and Radiative Transfer, 9: 721-732.

Liu, G., 1990, Permo-carboniferous paleography and coal accumulation and their tectonic control in North China and South China continental plates, International Journal of Coal Geology, 16: 73-117.

Mao, J. and Kawa, S.R., 2004, Sensitivity studies for space-based measurement of atmospheric total column carbon dioxide using reflected sunlight, Applied Optics, 43: 914–927.

Markham, B.L. and Barker, J.L., 1986, Landsat MSS and TM post calibration dynamic ranges, Exoatmospheric reflectance and at-satellite temperatures. EOSAT Landsat Technical Notes 1. Earth Observation Satellite Co. (Lanham, Maryland, EOSAT), USA, pp. 3-8.

Martini, B.A., 2002, New insights into the structural, hydrothermal, and biological systems of Long Valley Caldera using hyperspectral imaging, [PhD Thesis], UCSC Earth Sciences Department, University of California Santa Cruz, Santa Cruz.

Matsunaga, T., 1994, A Temperature-Emissivity Separation Method Using an Empirical Relationship between the Mean, the Maximum and the Minimum of the Thermal Infrared Emissivity Spectrum, Journal of Remote Sensing Society of Japan, 14(2): 230-241.

McMillin, L.M. and Fleming, H.E., 1976, Atmospheric transmittance of an absorbing gas : a computationally fast and accurate transmittance model for absorbing gases with constant mixing ratios in inhomogeneous atmosphere, Applied Optics, 15: 358–363.

Memmi, J., 2000, Cooking Centralia: a recipe for disaster, Geotimes, 45(9): 26-27.

Metzier, M.C. and Malila, W.A., 1985. Characterization and comparison of Landsat 4 and Landsat 5 Thematic Mapper data, Photogrammetric Engineering and Remote Sensing, 15: 1315-1330.

Miesch. C., Briottet, X., Kerr, Y. and Cabot, F., 2000, Radiative transfer solution for rugged and heterogeneous scene observations, Applied Optics, 39: 6830-6846.

Miller, C.E., Brown, L.R., Toth, R.A., Benner, D.C. and, Devi, V.M., 2005, Spectroscopic challenges for high accuracy retrievals of atmospheric CO_2 and the Orbiting Carbon Observatory (OCO) experiment, Comptes Rendus Physique, 6: 876–887.

Mitchell, T.L., 1839, Three Expeditions into the Interior of Eastern Australia with Descriptions of the Recently Explored Region of Australia Felix and the Present Colony of N.S.W., Eastern Australia: London, T. and W. Boone, V. 1.

Mukherjee, T.K., Bandopadhyay, T.K. and Pande, S.K., 1991, Detection and delineation of depth of subsurface coalmine fires based on an airborne multispectral scanner survey in a part of the Jharia Coalfield, India: Photogrammetric Engineering and Remote Sensing, 57: 1203-1207.

National Council for Safety in Mines (NCSM), 1981, Mine Disasters in India, Volume I & II, Directorate General of Mines Safety, Dhanbad.

National Oceanic and Atmospheric Administration (NOAA), 1999, Climate Monitoring and Diagnostic Laboratory (http://www.noaa.gov/ccgg/).

Paterson, J.C.K., 1910, Bengal District Gazetteer: Burdwan, Bengal Secretariat Book Depot, Calcutta.

Prakash, A. and Gupta, R.P., 1999, Surface fires in Jharia coalfield, India – their distribution and estimation of area and temperature from TM data, International Journal of Remote Sensing, 20(10): 1935-1946.

Prakash, A., Gupta, R.P. and Saraf A.K., 1997. A Landsat TM based comparative study of surface and subsurface fires in the Jharia coalfield, India, International Journal of Remote Sensing 18(11): 2463-2469.

Rădan, S.C. and Rădan, M., 1998, Rock magnetism and paleomagnetism of porcelanites/clinkers from the western Dacic Basin (Romania), Geol Carpat, 49: 209–211.

Ramaswamy V. et al., 2001, Climate Change 2001: The Scientific Basis,

IPCC. In: Houghton JT et al., eds. Cambridge, Cambridge University Press, p. 351-416.

Rattigan, J. H., 1967a, Phenomena about Burning Mountain, Wingen, New South Wales, Australian Journal of Science, 30: 183-184.

Rattigan, J. H., 1967b, Occurrence and genesis of halloysite, Upper Hunter Valley, N.S.W., Australia, American Mineralogist, 52: 1795-1805.

Rayner, P.J. and O'Brien, D.M., 2001, The utility of remotely sensed CO2 concentration data in surface source inversions, Geophysical Research Letter, 28: 175–178.

Rayner, P.J., Enting, I.G., Francey, J. and Langenfelds, R., 1999, Reconstructing the recent carbon cycle from atmospheric CO2, $\delta^{13}C$ and O2/N2 observations, Tellus-B, 51: 213–232.

Reddy, C.S.S., Srivastav, S.K., and Bhattacharya, A., 1993, Application of Thematic Mapper short wavelength infrared data for the detection and monitoring of high temperature related geoenvironmental features, International Journal of Remote Sensing, 14(17): 3125-3132.

Reuters News, 1998, Five die in coal mine fire in Kyrgyzstan: 16 July 1998, Reuters Limited.

Reuters News, 2004, Six dead in Argentina coal mine fire, 8 missing: 17 June 2004, Reuters Limited.

Reuters News, 2005, Nine missing after Russian coal mine fire: 26 January 2005, Reuters Limited.

Ricchiazzi, P., Yang, S., Gautier, C. and Sowle, D., 1998, SBDART: A research and teaching software tool for plane-parallel radiative transfer in the Earth's atmosphere, Bulletin of American Meteorological Socity, 79(10): 2101-2114.

Richter, R., 2005, Atmospheric/Topographic Correction for Satellite Imagery (ATCOR 2/3 User Guide, Version 6.1, January 2005), DLR, Remote Sensing Center, Wessling. DLR-IB 565-01/05. Germany, pp. 57.

Rodgers, C.D., 1976, Retrieval of atmospheric temperature and composition from remote measurements of thermal radiation. Review of Geophysical and Space Physics, 14: 609–624.

Rosema, A., Guan, H. and Veld, A., 2001, Simulation of spontaneous combustion, to study the causes of coal fires in the Rujigou Basin, Fuel, 80: 7-16.

Rosema, A., Guan, H., and Veld, H., 2001, Simulation of spontaneous combustion, to study the causes of coalfires in the Rujigou Basin, Fuel, 80: 7-16.

Rosema, A., Guan, H., Veld, H., Vekerdy, Z. Ten Katen, A.M. and Prakash, A., 1999, Manual of Coalfire Detection and Monitoring: Utrecht, Netherlands Institute of Applied Geosciences, NITG Publications, p. 245.

Rosema, A., van Genderen, J.L. and Schalke, H.J.W.G., 1995, Environmental monitoring of coalfires in North China. ISBN 9054111054, BCRS project 4.2/TO-04, BCRS report 93-29, 6 p.

Rothermund, D. and Wadhwa, D.C., 1978, Zamindars, Mines and Peasants, Manohar Publications, New Delhi.

Rothery, D.A. Francis, P.W. and Wood, C.A., 1998, Volcano monitoring using short wavelength infrared data from satellite, Journal of Geophysical Research, 93: 7993-8008.

Rothman, L.S. et al., 2003, The HITRAN molecular spectroscopic database: edition of 2000 including updates through 2001, Journal of Quantitative Spectroscopy and Radiative Transfer, 82: 5–44.

RoyChaudhuri, R., 1996, Gender and labour in India: The Kamins of Eastern coalmines, 1900-1940, Minerva, Calcutta.

Saha, K., 2004, Mine fire problem: A study in environmental impact of mining in the Raniganj Coalbelt, West Bengal, [PhD Thesis], Burdwan University, Burdwan.

Saraf, A.K., Prakash, A., Sengupta, S. and Gupta, R.P., 1995, Landsat TM data for estimating ground temperature and depth of subsurface coalfire in the Jharia coalfield, India, International Journal of Remote Sensing 16(12): 2114-2124.

Sarkar, S.K. and Sarkar, S., 1995, State of environment and development in Indian coalfields: coalfields in West Bengal, Oxford and IBH Publishing Company Pvt. Ltd., New Delhi.

Saunders, R.W., Matricardi, M. and Brunel, P., 1999, An Improved Fast Radiative Transfer Model for Assimilation of Satellite Radiance Observations. Quarterly Journal Royal Meteorological Society, 125: 1407-1425.

Schläpfer D., Borel C.C., Keller J., and Itten K.I., 1996, Atmospheric Pre-Corrected Differential Absorption Techniques to Retrieve Columnar Water Vapor: Application to AVIRIS 91/95 Data. Summaries of the Sixth Annual JPL Airborne Earth Science Workshop, Vol. 1, JPL, Pasadena (CA), pp 209-217.

Schläpfer, D., Borel, C.C., Keller, J. and Itten, K.I., 1998, Atmospheric Pre-Corrected Differential Absorption Techniques to Retrieve Columnar Water Vapor, Remote Sensing of Environment, 65(3): 353-366.

Schmal, D., 1987, A model for the spontaneous heating of stored coal [Ph.D. Thesis]: Delft, The Netherlands, Technology University of Delft, p. 167.

Schurin, B.D. and Ellis, R.E., 1968, Integrated intensity measurements of carbon dioxide in the 2.0μm, 1.6μm, and 1.43μm regions, Applied Optics, 7(3): 467-470.

Sinha, P.R., 1986, Mine Fires in Indian Coalfields, Energy, 11(12): 1147-1154.

Slavecki, R.J., 1964, Detection and location of subsurface coalfires, in Proceedings, Symposium on Remote Sensing of Environment, 3rd, Ann Arbor: Michigan, University of Michigan, p. 537-547.

Smith, W.L., 1970, Iterative solution of the radiative transfer equation for temperature and absorbing gas profile of an atmosphere, Applied Optics, 9: 1993–1999.

Sobrino, J.A., and Raissouni, N., 2000, Towards remote sensing methods for land cover dynamic monitoring, application to Morocco, International Journal of Remote Sensing, 21(2): 353– 366.

Sobrino, J.A., Jimenez-Munoz, J.C. and Paolini, L., 2004, Land surface temperature retrieval from LANDSAT TM 5, Remote Sensing of Environment, 90: 434–440.

Stracher, G.B. and Taylor, P. T., 2004, Coalfires burning out of control around the world: thermodynamic recipe for environmental catastrophe, International Journal of Coal Geology, 59: 7-17.

Tans, P.P., Fung, I.Y. and Takahashi, T., 1990, Observational constraints on the global atmospheric CO_2 budget, Science, 247: 1431–1438.

Tetuko, S.S. J., Tateishi, R. and Takeuchi, N., 2003, A physical method to analyse scattered waves from burnt coal seam and its application to estimate thickness of fire scars in central Borneo using L-Band SAR data, International Journal of Remote Sensing, 24(15): 3119-3136.

Théry I., Gril J., Vernet J.L., Meignen L. and Maury J., 1996, Coal used for Fuel at Two Prehistoric Sites in Southern France: Les Canalettes (Mousterian) and Les Usclades (Mesolithic), Journal of Archaeological Science, 23(4): 509-512.

Valor, E. and Caselles V., 1996, Mapping land surface emissivity from NDVI: Application to European, African and south American areas, Remote Sensing of Environment, 57: 167-184.

van de Griend, A.A. and Owe, M., 1993, On the relationship between thermal emissivity and the normalized difference vegetation index for natural surfaces, International Journal of Remote Sensing, 14(6): 1119-1131.

van der Meer, F.D., van Dijk, P.M., Gangopadhyay, P.K. and Hecker, C.A., 2004, Remote-sensing GIS based investigations of coalfires in northern China : global monitoring to support the estimation of CO2 emissions from spontaneous combustion of coal, in Proceedings, Asian Space Conference, 1st, Chiang Mai: Thailand, Geo-Informatics and Space Technology Development Agency, p. 6.

van Genderen, J.L., Cassells, C.J.S. and Zhang X.M., 1996, The synergistic use of remotely sensed data for the detection of underground coalfires, International Archives of Phtogrammetry and Remote Sensing, XXXI(7): 722-727.

Varanasi, P. and Nemtchinov, V., 1994, Thermal infrared absorption coefficients of CFC-12 at atmospheric conditions, Journal of Quantitative Spectroscopy and Radiative Transfer, 51: 679-687.

Vermonte, E.F., Tanré, D., Deuze, J.L., Herman, M. and Morcrette, J,J., 1997, Second simulation of the satellite signal in the solar spectrum, 6S: An overview. IEEE Transactions of Geosciences and Remote Sensing, 35(3): 675-686.

Voigt, S., A. Tetzlaff, J. Zhang, C. Künzer, B. Zhukov, G. Strunz, D. Oertel, A. Roth, P. van Dijk and H. Mehl, 2004, Integrating satellite remote sensing techniques for detection and analysis of uncontrolled coal seam fires in North China, International Journal of Coal Geology, 59: 121-136.

Walker, S., 1999, Uncontrolled fires in coal and coal wastes, International Energy Agency, London, 73 p.

Wan, Y.Q. and Zhang X.M., 1996, Using a DEM to reduce the effect of solar heating on Landsat TM thermal IR images and detection of coalfires, Asia-Pacific Remote Sensing and GIS Journal, 8: 65-72.

Wang, C., 2002, Detection of coalfires in Xinjiang (China) using remote sensing techniques [MSc Thesis]: Enschede, ITC, 93 p.

Whitehouse, A.E. and Mulyana, A.A.S., 2004, Coalfires in Indonesia, International Journal of Coal Geology, 59: 91–97.

World Coal Institute, 2007, Safety at Coal Mine (http://www.worldcoal.org/).

Worldbank, 2004, Mitigating the Environmental Impact of Coal in China (http://web.worldbank.org/).

Xie, Y., 2001, Einfluss der weidewirtschaft auf die vegetation und die ökologischen bedingungen der trockensteppe in Ningxia, China. Frankfurt, Germany.

Yang, H., 1995, Detection of Areas of Spontaneous Combustion of Coal Using Airborne and TM Data in Xinxiang, China [MSc Thesis]: Enschede, ITC, 73 p.

Zhang X.M., van Gengeren, J.L. and Kroonenberg, S.B., 1997, A method to evaluate the capability of Landsat-5 TM band 6 data for sub-pixel coalfire detection, International Journal for Remote Sensing, 18(15): 3279-3288.

Zhang, J.Z., 1996, SWIR spectra of rocks in areas affected by coalfires, Xinjinag autonomous region P.R. of China [MSc Thesis]: Enschede, 74 p.

Zhang, X., Kroonenberg, S.B. and de Boer, C.B., 2004, Dating of coalfires in Xinjiang, north-west China, Terra Nova, 16(2): 68-74.

Zhao, X. and Jiang, X., 2004, Coal mining: Most deadly job in China, Xinhua News Agency (http://www.chinadaily.com.cn).

Summary

Subsurface and surface coal fires are a serious problem in many coal-producing countries. Combustion can occur within the coal seams (underground or surface), in piles of stored coal, or in spoil dumps at the surface. While consuming a non renewable energy source, coal fires promote several environmental problems. Emission of several greenhouse gasses (GHGs), especially large amounts of CO_2 is the most significant among them. The fires in coal seams can be initiated spontaneously under certain conditions, where coal, air and heat (from sun) are found together. Lightning and forest/bush fire can also initiate coal fires. In some cases, human negligence, a mine accident, or a human-induced heat source could be the reason for a coal fire.

Coal fires are common in many coal-producing countries, such as China, India, Indonesia, the United States, Australia, South Africa, and Russia. The potential for coal to spontaneously combust depends on its aptitude of oxidization at ambient temperature under certain conditions. This occurs through the *absorption* of oxygen at the surface of the coal, and is an exothermic reaction. Therefore, the temperature of the coal may start to increase. If the temperature reaches what often is called the 'threshold' temperature somewhere between 353 and 393 K, a steady reaction results in the emanation of gaseous products, such as CO_2. Once the threshold temperature is reached and the second stage of the reaction begins, heat is usually generated at such great rate that the temperature of the coal will continue to increase until combustion is reached.

Apart from ineffectively consuming a nonrenewable energy resource coal fires promote several environmental problems e.g. subsidence, land degradation and GHGs emissions. To tackle these severe economic and environmental problems remote sensing can play an important role. The present research focuses on coal fire detection, simulation and monitoring for better management of coal fires, and CO_2 emission estimation.

Among the all GHGs that are emitted from coal fires, CO_2 is the most significant because of its high quantity and adverse effect on environment. The core aim of the present research was to develop a hyperspectral remote sensing and radiative transfer based model that is able to estimate CO_2 concentration (ppmv) from coal fires.

Since 1960s remote sensing is being used as a tool to detect and monitoring coal fires. With time, remote sensing has proven to be an efficient and reliable tool for this purpose. In the present study multi-temporal, multi-sensor and multi-spectral thermal remote sensing data are being used to detect and monitor coal fires. Emissivity (emitting capability of an object compared to a blackbody) plays an important role to determine the surface temperature of a body. In the former coal fire related studies, an average emissivity value (0.96) was used to represent all landcover. Unlike the earlier studies, the present study explores the possibilities of satellite derived emissivity to detect and monitor coal fires. Two methods of emissivity extraction from satellite data were tested, namely NDVI (Normalized Difference Vegetation Index) derived and TES (Temperature Emissivity Separation) in two study areas situated in India and China. It was observed that the satellite derived emissivity offers a better kinetic surface temperature, which leads to a better understanding of the extent and spreading of the coal fires.

In order to reduce coal fire related GHG emissions it is crucial to understand and manage coal fires effectively. Proper understanding of the nature of migration of a coal fire (dynamics) is necessary for a better management of coal fires to reduce the emissions of GHGs in local environment. To understand the dynamics of coal fires multi-temporal thermal infrared data with adequate knowledge of study area can be used for monitoring purposes. Multitemporal spaceborne remote sensing data can be used to study this migration and expresses the results as vectors, indicating direction and speed of migration. The

present study proposes a 2D model that recognizes an initiation point of coal fire from thermal remote sensing data and consider local geological settings (dip angle and location of coal seam, rock porosity, crack location and density) to predict the speed and future location of coal fires. It was observed that the model can predict the future location of coal fires with predefined time period. However, few uncertainties (e.g. abrupt meteorological change) can not be taken account in this model.

To explore the sensitivity of present hyperspectral sensors with different atmospheric CO_2 concentrations, additive and multiplicative noise were introduced in FASCOD simulated original spectra and evaluated. A comparison among the present available hyperspectral sensors was made to find out the most suitable remote sensing sensor for CO_2 quantification.

To achieve the core research objective, firstly, a band ratioing method was used for column atmospheric retrieval of CO_2. Secondly atmospheric models were simulated in FASCOD to understand the local radiation transport and then the model was implemented with the inputs from hyperspectral remote sensing data. Both methods (band ratioing and radiative transfer based) were tested in a coal fire affected area in northern China. It was observed that retrieval of columnar abundance of CO_2 with the band ratioing method is faster as less simulation is required in FASCOD. Alternatively, the inversion model could retrieve CO_2 concentration from a (certain) source because it excludes the uncertainties in the higher altitude.

Remote sensing plays an important role in detecting and monitoring coal fires and can therefore help prevent economic loss and environmental disaster. With the necessary inputs from radiative transfer codes, a combined model based on thermal and hyperspectral remote sensing data would be useful to tackle the coal fires much effectively. The outputs from thermal remote sensing data would be able to detect and monitoring coal fires for a good fire fighting plan. Alternatively outputs from hyperspectral remote sensing data would be able to quantify the CO_2 concentration increase due to emission from coal fires. Finally the combined model would be useful for a total management of coal fire efficiently.

Samenvatting

Steenkoolbranden in de ondergrond en aan de oppervlakte vormen een groot probleem in veel steenkool producerende landen. Ontbranding kan voorkomen in de steenkool dagzomen (ondergronds of aan de oppervlakte), in steenkool opslag, of in storthopen aan de oppervlakte. Dit resulteert niet alleen in het verbruik van een kostbare grondstof; steenkoolbranden zijn ook de oorzaak van een aantal milieu problemen. De uitstoot van enkele broeikasgassen (GHG's), met in het bijzonder grote hoeveelheden CO_2, vormt het meest belangrijke hiervan. De branden in steenkool dagzomen kunnen onder bepaalde omstandigheden spontaan ontstaan, wanneer steenkool, lucht en warmte samen voorkomen. Bliksem en bosbranden kunnen ook steenkoolbranden veroorzaken. In andere gevallen kan menselijke onachtzaamheid, een mijnbouw ongeluk, of één of andere warmtebron door menselijk toedoen de aanleiding vormen voor een steenkoolbrand.

Steenkoolbranden zijn een normaal verschijnsel in vele steenkool producerende landen, zoals China, India, Indonesië, de Verenigde Staten, Australië, Zuid Afrika en Rusland. Spontane ontbranding van steenkool hangt af van de neiging tot oxidatie bij de omgevingstemperatuur onder bepaalde omstandigheden. Dit vindt plaats door *absorptie* van zuurstof aan het oppervlakte van de steenkool, en is een exothermische reactie. Hierdoor kan de temperatuur van de

steenkool stijgen. Als de temperatuur een waarde bereikt tussen de 353 en 393 K, wat vaak als 'drempelwaarde' wordt aangeduid, resulteert een permanente reactie in de uitstoot van gasvormige producten, zoals CO_2. Zodra de drempelwaarde is bereikt en het tweede stadium van de reactie begint, wordt de warmte gewoonlijk in een zodanig hoog tempo ontwikkeld dat de temperatuur van de steenkool blijft stijgen totdat ontbranding het gevolg is.

Naast het nutteloos verbruiken van een niet-hernieuwbare energiebron veroorzaken steenkoolbranden verschillende milieuproblemen, zoals bodemdaling, land degradatie en de uitstoot van broeikasgassen. Aardobservatie kan een belangrijke rol spelen in de aanpak van deze ernstige economische en milieuproblematiek. Het huidige onderzoek richt zich op het detecteren, simuleren en monitoren van steenkool branden, met als doel een betere beheersing en het maken van een schatting van de CO_2 uitstoot.

Onder alle broeikasgassen die worden uitgestoten door steenkool is CO_2 het meest belangrijk vanwege de grote hoeveelheid. Het centrale doel van dit onderzoek is om een model te ontwikkelen, gebaseerd op hyperspectrale aardobservatie en stralingsinteractie, dat in staat is om de CO_2 concentratie (ppmv) van steenkoolbranden te schatten.

Aardobservatie wordt sinds de zestiger jaren gebruikt als hulpmiddel om steenkoolbranden op te sporen en in de gaten te houden. Door de tijd heen heeft aardobservatie bewezen een betrouwbaar en efficient middel te zijn voor deze toepassing. In de huidige studie worden multi-temporele, multi-sensor en multi-spectrale thermische aardobservatie gegevens gebruikt om steenkoolbranden te detecteren en te volgen. De emissiviteit (uitstraling capaciteit van een object ten opzichte van een zwart lichaam) speelt een belangrijke rol in de bepaling van de oppervlakte temperatuur van een object. In eerdere studies naar steenkoolbranden werd een gemiddelde waarde voor emissiviteit (0.96) gebruikt voor elk type terrein oppervlakte. In tegenstelling daarmee probeert de huidige studie de mogelijkheid te onderzoeken om steenkoolbranden te ontdekken en te volgen met behulp van emissiviteit die is afgeleid uit satelliet gegevens. Twee methodes om emissiviteit uit satellietgegevens te bepalen zijn onderzocht, namelijk NDVI (Normalized Difference Vegetation Index) afgeleide en TES (Temperature Emissivity Separation), in twee studiegebieden in India en

China. Het resultaat is dat de door middel van satellietgegevens verkregen emissiviteit een betere kinetische oppervlakte temperatuur oplevert, wat tot een beter begrip van de omvang en uitbreiding van de steenkoolbranden leidt.

Om de CO_2 uitstoot door steenkoolbranden te reduceren is het essentieel om steenkoolbranden goed te doorgronden en te kunnen beheersen. Een goed begrip van de aard van migratie van steenkoolbranden (dynamiek) is noodzakelijk voor een betere beheersing ervan om tot een terugdringing van uitstoot van broeikasgassen in de omgeving te komen. Om de dynamiek van steenkoolbranden te begrijpen kunnen multi-temporele thermisch infrarood gegevens samen met voldoende kennis van het studie gebied gebruikt worden voor observatie doeleinden. Multi-temporele aardobservatie satelliet gegevens kunnen gebruikt worden om de migratie waar te nemen en het resultaat uit te drukken in vectoren die de richting en snelheid van migratie aangeven. In deze studie wordt een 2-D model voorgesteld dat uit thermische aardobservatie data een beginpunt van een steenkoolbrand identificeert en de lokale geologische omstandigheden in beschouwing neemt (laagstand en locatie van de steenkool dagzoom, porositeit van het gesteente, plaats en dichtheid van scheuren in het gesteente) om de snelheid en toekomstige plaats te voorspellen. De uitkomst is dat het model binnen een bepaalde tijdsduur de toekomstige locatie van steenkoolbranden kan voorspellen. Enkele onzekerheden (zoals abrupte meteorologische variabiliteit) kunnen echter niet in dit model meegenomen worden.

Om de gevoeligheid van hedendaagse hyperspectrale sensoren te onderzoeken met betrekking tot verschil in concentratie van atmosferisch CO_2, werd additieve en multiplicatieve ruis toegevoegd in gesimuleerde originele FASCOD spectra en beoordeeld. Een vergelijking van de huidige beschikbare hyperspectrale sensoren is gemaakt om de meest geschikte sensor voor CO_2 kwantificatie te bepalen.

Om het centrale onderzoeksdoel te realiseren is, in de eerste plaats, een band ratio methode gebruikt voor bepaling van CO_2 in de atmosferische kolom. Ten tweede zijn atmosferische modellen gesimuleerd in FASCOD om de lokale stralingsinteractie te begrijpen, en vervolgens is het model ten uitvoer gebracht met de invoer van hyperspectrale aardobservatie gegevens. Beide methoden (gebaseerd op band ratio en stralingsinteractie) zijn getest in een door steenkoolbranden geteisterd

gebied in het noorden van China. Het resultaat laat zien dat de bepaling van de CO_2 hoeveelheid per kolom sneller gaat met de band ratio methode omdat daarvoor minder simulatie benodigd is in FASCOD. Daarentegen zou het inversie model de CO_2 concentratie van een (bepaalde) bron kunnen bepalen omdat het de onzekerheden op grotere hoogte uitsluit.

Aardobservatie speelt een belangrijke rol in het opsporen en observeren van steenkoolbranden, en kan zodoende behulpzaam zijn om economisch verlies en milieu schade te voorkomen. Met de noodzakelijke invoer van stralingsinteractie codes, zou een gecombineerd model gebaseerd op thermale en hyperspectrale aardobservatie gegevens bruikbaar kunnen zijn om steenkoolbranden efficiënter aan te pakken. De resultaten afkomstig van thermale aardobservatie gegevens zouden in staat moeten zijn om steenkoolbranden waar te nemen en te observeren ten behoeve van een goed brandbestrijdingsplan. Aan de andere kant zouden de uitkomsten van hyperspectrale gegevens de CO_2 concentratie verhoging ten gevolge van uitstoot door steenkool branden kunnen kwantificeren. Tenslotte zou een gecombineerd model nuttig kunnen zijn voor een integraal en efficiënt beheer van steenkoolbranden.

Acknowledgements

This thesis could not have been completed without the great support and the encouragement of a number of people.

I am indebted to the financial support from the Netherlands Fellowship Program (NFP) that enabled me to undertake this research work.

It was a great pleasure and enlightening to work with Freek, my first supervisor and *guru* in hyperspectral remote sensing. Despite his very busy schedule, his door was always open for me for discussions. Without his active support and critical comments, this research could have landed in some 'interesting' problems.

I know Paul, my second supervisor closely since my MSc. Without his valuable and timely comments it was nearly impossible for me to narrow down my ideas to reach the goal. His constant encouragement and support throughout my ITC life can not be expressed in few words. I am also thankful to him for translating the summary in Dutch.

My heartfelt thanks and gratitude go to Kuntala and David for their intellectual and valuable comments.

The critical comments from several anonymous reviewers were extremely helpful to improve the articles.

I gratefully acknowledge the academic and technical support from Martin Hale, John van Genderen, Ben, John, Anupma, David, Glenn, Zoltan, Ambro, Pravesh, Ulan, Harald, Frank, Klaas, Geoffry, Jwelle, Boudwijn, Chris, Mila, Srirama and Xin - thank you for your suggestions.

The supports extended by Loes, Christie, Ard, Marie, Theresa, Bettine, Adrie, Frans, Marjolein, Saskia, Johan, Yevtte, Ruben during my long stay in ITC, are fondly recalled. I would also like to express my thankfulness all staff members of ESA departments, Student Affairs and all technical departments for their kind support.

Ajay, Alok, Bharat, Patrick, Hein, Sanders - my officemates – thank you friends for your patience, friendly attitude and tolerate my smoking. I would also thank you all IIRS students and the Indian community, Farhadbhai & Boudi, and many more, who made Holland my second home. It was a great pleasure to have friends in and outside PhD community. Marleen, Gaby, Marion, Kim, Marco, Istiak, Kamal, Moses, Carolina, Enrique, Trias, Graciela, Veronica, Peter, Shravan, Chinmay, Shreedhar, Saibal, Tapas, Pankaj, Shekhar, Lal, Lalan, Asit, Anoop, Richard, Talat, Tuan, Hoa, Snigdha, Anisha, Deepty, Arindam, Mousumi, Swati and Tam – thank you for your friendship and help. Qi - thank you for your support during the final compilation of my thesis.

Back home, I would like to express my sincere thankfulness to my elder brothers and Pranab who were always there to extend their help to my family during my long absence.

Finally, I would like to thank my mother Mrs. Rina Ganguly, my father Mr. Krishna Kumar Ganguly and my wife Dr. Kanika Saha for their inspiration, moral support and love which enabled me to complete this work.

During my PhD I have received the best gift of my life, Rhitav, my son. His innocent and happy face encouraged me keep walking even in the worst condition.

Prasun K Gangopadhyay
Enschede, June, 2008

Biography

Prasun K Gangopadhyay was born on the 20th March of 1970 in Burdwan, West Bengal, India. In 2003 he obtained a M.Sc. degree in Geo-information Science and Earth Observation from ITC, the Netherlands. His main research interest is focused on thermal and hyperspectral based remote sensing applications in environmental geosciences. Since 1995 he is working on coal mining and related environmental problems in different countries. He has gained experience in coal mining related environmental problems (such as surface and subsurface coalfire detection, monitoring and estimation of related emissions and impact of coal mining on environment) using remote sensing as a prime tool in India, China and Australia. Since 2003 he is working on his PhD research *Coalfire related CO_2 emissions and remote sensing* (ITC and Utrecht University, the Netherlands). He has published scientific articles in journals, books and other media. His future research interest is working on coalfire mapping in global context and emission estimation using remote sensing. Other than coalfire he is keenly interested in other high temperature events such as volcanoes and the quantitative estimation of different gases from these sources with remote sensing.

Publications

Journals (peer reviewed)

Gangopadhyay, P.K., van der Meer, F. and van Dijk**,** P.M., 2008, Comparison of two methods of satellite derived emissivity for surface temperature extraction in a coalfire affected area. *Remote Sensing of Environment* (in process).

Gangopadhyay, P.K., van der Meer, F., van Dijk, P. and Saha, K., 2008 Use of satellite derived emissivity to detect coalfire related surface temperature anomalies in Jharia coalfield, India. *International Journal of Remote Sensing* (submitted).

Gangopadhyay, P.K., van der Meer, F., van Dijk, P. and van der Werff, H., 2008, Monitoring coalfire using remote sensing and 2D geological modelling. *Coal Geology* (submitted).

Gangopadhyay, P.K., van der Meer, F., van Dijk, P. and Saha, K., 2008, Coalmining, coalfire and environment in India and China. *International Journal of Environmental Studies* (in review).

Gangopadhyay, P. K., van der Meer, F. and van Dijk, P., 2008, Detecting anomalous CO_2 flux using space borne spectroscopy. *International Journal of Applied Earth Observation and Geoinformation* (in press).

Gangopadhyay, P.K., van der Meer, F. and van Dijk, P., 2008, Atmospheric modelling using FASCOD to identify CO_2 absorption bands and their suitability analysis in variable concentrations for remote

sensing applications. *Journal of Quantitative Spectroscopy and Radiative Transfer*, 109: 670–683.

Lahiri-Dutt, K. and **Gangopadhyay, P.K.,** 2007, Subsurface coalfires in the Raniganj coalbelt: investigating their causes and assessing human impacts. *Resources, Energy, and Development*, 4(1): 71-87.

Gangopadhyay, P.K., Lahiri-Dutt, K. and Saha, K., 2006, Application of remote sensing to identify coalfires in the Raniganj Coalbelt, India. *International Journal of Applied Earth Observation and Geoinformation*, 8: 188-195.

Gangopadhyay, P.K., Maathuis, B. and van Dijk P., 2005, ASTER Derived Emissivity and Coalfire Related Surface Temperature Anomaly: A Case study in Wuda, North China. *International Journal or Remote Sensing*, 26(24): 5555-5751.

Saha, K., **Gangopadyhay, P.K.** and Bhattacharya, K., 2005, Studies on the Environmental Impact due to Coal Mining Activities in the Raniganj Coalbelt in West Bengal, Impacts of Coal Mining Activities on Environment: A Case Study in Raniganj Coalbelt, West Bengal. *Indian Journal of Regional Science*, 37: 85-95.

Article in edited books

Gangopadhyay, P.K., 2007, Application of remote sensing in coal - fire studies and coal - fire – related emissions. In: Geology of coal fires : case studies from around the world. ed. G.B. Strachter. Boulder : Geological Society of America (GSA). (Geological Society of America Reviews in Engineering Geology: 18), ISBN 978-0-8137-4118-5 pp. 239-248.

Gangopadhyay, P.K., van der Meer, F.D., and van Dijk, P.M., 2007, Monitoring coalfires using dynamic remote sensing, in ERSEC Ecological Book Series–4 on Coalfire Research, Beijing, UNESCO (in press).

Web articles, conference proceedings and dissertation papers

Gangopadhyay, P.K., 2007, Coalfire and Remote Sensing (http://www.eoearth.org/article/Coalfire_and_remote_sensing).

Gangopadhyay, P.K., Saha, K., van der Meer, F., van Dijk, P., 2006, Satellite Derived Emissivity and Coalfire Related Surface Temperature Anomalies in Raniganj Coalbelt, India. *The International Archives of the Photogrammetry, Remote Sensing and Spatial Information Sciences*, 34(XXX).

Gangopadyhay, P. K., van der Meer, F. and van Dijk, P., 2005, Atmospheric modelling using high resolution radiative transfer codes and identification of CO2 absorption bands to estimate coalfire related emissions. *In*: Zagajewski, B., Sobczak, M. and Prochnicki, W. eds. *Proceedings 4th Workshop on Imaging Spectroscopy*, Warsaw University, Warsaw, p. 92.

van der Meer, F.D., van Dijk, P.M., **Gangopadhyay, P.K.** and Hecker, C.A., 2004, Remote-sensing GIS based investigations of coalfires in northern China : Global monitoring to support the estimation of CO2 emissions from spontaneous combustion of coal. *In*: Vibulresth and Soo, D.N., eds. *Proceeding of the 1st Asian Space Conference*: Chiang Mai, Thailand, p. 6.

Gangopadhyay, P.K., 2003, Coalfire Detection and Monitoring in Wuda, North China: A Multi-spectral and Multi-sensor TIR Approach, *MSc Thesis*, ITC, Enschede.

Gangopadhyay, P.K., 2000, Surface Temperature Mapping and Detection of Surface & Subsurface Coal-mine Fires of the Raniganj Coalbelt (West Bengal) Using Remote Sensing and GIS, *Dissertation paper*, Indian Institute of Remote Sensing, DehraDun.

The full list of ITC PhD theses are available at:
http://www.itc.nl/research/phd/phd_graduates.aspx